TIME-RESOLVED, CONTRAST-ENHANCED MR ANGIOGRAPHY OF THE PERIPHERAL VESSELS WITH RADIAL SAMPLING AND HYPR RECONSTRUCTION

BY

LAUREN A. KEITH

A dissertation submitted in partial fulfillment of

the requirements for the degree of

Doctor of Philosophy

(Medical Physics)

at the

University of Wisconsin – Madison

2012

Date of final oral examination: August 28, 2012

This dissertation is approved by the following members of the Final Oral Committee:

Charles A. Mistretta, Professor, Medical Physics
Frank R. Korosec, Professor, Radiology
Oliver Wieben, Assistant Professor, Medical Physics
Scott B. Reeder, Associate Professor, Radiology
Walter F. Block, Associate Professor, Biomedical Engineering

TIME-RESOLVED, CONTRAST-ENHANCED MR ANGIOGRAPHY OF THE PERIPHERAL VESSELS WITH RADIAL SAMPLING AND HYPR RECONSTRUCTION

LAUREN A. KEITH

Under the supervision of Charles Mistretta, PhD
and Frank Korosec, PhD
At the University of Wisconsin - Madison

Abstract

Atherosclerotic vascular disease (AVD) – characterized by narrowing and stiffening of the arteries due to plaque – is one of the most common causes of morbidity and mortality in the United States and throughout the world. Currently, medical imaging plays an important role in both the diagnosis of the disease and in the planning of treatment. In particular, magnetic resonance angiography (MRA) has been widely used as a tool for non-invasive and safe vascular imaging despite spatial and temporal resolutions that are generally poorer than other imaging modalities deemed less safe or more invasive like computed tomography angiography (CTA) or x-ray digital subtraction angiography (DSA). For MRA to truly supersede these imaging modalities as the optimal technique

from both a safety and image quality perspective, new and advanced data acquisition and reconstruction techniques are necessary.

The purpose of this work is to develop a robust protocol for MRA – particular focus being placed on of the peripheral vessels – with imaging parameters that exceed those currently attainable with MRA in the clinical setting. This is achieved by utilizing radial k-space sampling in conjunction with an advanced, constrained reconstruction technique (HYPR). In the first phase of this work, experiments were designed to characterize the accuracy and fidelity of the reconstruction technique. In the second phase, protocols were developed based on two distinct radial k-space acquisition techniques: stack-of-stars (SOS) and vastly undersampled isotropic projection reconstruction (VIPR). The specific benefits and deficits of each protocol were evaluated. In the final phase, data were acquired from patients with peripheral artery disease (PAD) using the current clinical reference standard for MRA and a robust imaging protocol based on radial sampling and HYPR reconstruction. Statistical analysis was performed to compare the agreement in diagnoses made from each protocol.

Acknowledgements

I first contacted Dr. Charles Mistretta during the spring semester of my sophomore year at the University of Wisconsin. I had recently declared my undergraduate major – physics – and I was trying to sort out what my next step would be after earning my degree. The work he shared with me was inspiring – an avenue to use physics to affect real, tangible change in the medical field; I shamelessly asked if there was a position open in his lab. Dr. Mistretta's willingness to support, mentor and take a chance on young scientists is the reason I was introduced to the field of medical physics.

I would also like to acknowledge Dr. Frank Korosec. His directness and honesty were refreshing and his willingness to give me the freedom to design and drive my projects provided priceless experience. He somehow managed to give what I consider to be the perfect balance of guidance and independence.

My other committee members: Dr. Scott Reeder, Dr. Oliver Wieben and Dr. Wally Block have provided invaluable advice and support. I thank them deeply. I would like to acknowledge the HYPR group: Dr. Jim Holmes, Dr. Kang Wang, Dr. Jean Brittain and Mahdi Rahimi. Our discussions were always fruitful and fun. Dr. Steve Kecskemeti not only provided answers to countless questions, but did so (seemingly) happily. Jan Yakey, Kelli Hellenbrand, Sara John and Jenelle Fuller did their jobs exceptionally well and with attitudes that made them a pleasure to work with. Alejandro Munoz del Rio assisted with – and tried to teach me – statistics (often under less than optimal time constraints).

I'd like to thank all the students of the MRI research group for lively discussions and distractions. It has truly been a pleasure and a privilege to learn and work among such great scientists and people.

Finally, I'd like to acknowledge my family: Mike, Roy, Penny and Lucas and Margaret, Caryl and Paul. They have been a tremendous source of encouragement and happiness, two things that are both essential (and at times difficult) to preserve while pursuing one's doctorate. I thank them all.

This work is dedicated:

to my parents – *for their persistent emphasis on thoughtfulness and reason;*

to my brother – *for being a limitless source of motivation and inspiration;*

to my future-husband – *for his unyielding support and selflessness.*

Table of Contents

Chapter 1: Introduction

1.1 Motivation

There is a significant need for safe, efficient and accurate vascular imaging methods to aid in both disease diagnosis and interventional treatment planning. Magnetic resonance angiography (MRA) has been widely used as a tool for non-invasive vascular imaging. However, to approach the superior spatial and temporal resolutions of more invasive imaging techniques, new, highly advanced methods are required. The purpose of this research is to create a robust protocol for time resolved, contrast-enhanced imaging of the vascular system of the body. Particular attention has been paid to the vessels in the lower extremities and protocols were tailored to this application; however, both the protocols created and the knowledge gained during the fulfillment of this research are useful and applicable to many other MR angiography applications.

1.2 General Hypothesis

The general hypothesis of this dissertation is in multiple parts. First, the highly constrained backprojection (HYPR) reconstruction method can be used to provide highly undersampled time frames that demonstrate a high signal-to-noise ratio (SNR) and low undersampling artifacts that sustain limited penalty in either spatial or temporal fidelity. Second, a robust imaging protocol can be developed using a combination of radial k-space sampling and HYPR reconstruction to produce time-resolved, contrast-enhanced exams of the peripheral vasculature with higher spatial and temporal resolutions than methods currently used in the clinic today. Third, the improvements in imaging parameters using such a protocol are attainable without a decrease in diagnostic accuracy.

1.3 Chapter Summary

Chapter 2 provides a review of previously published work and the background information necessary to appreciate the need and novelty of the work that follows. This includes: the clinical background of peripheral artery disease (PAD); current diagnostic tools for PAD; the role that MRA currently plays in the diagnosis; radial k-space sampling; and highly constrained backprojection reconstruction.

Chapter 3 is an account of a study designed to test the temporal fidelity of HYPR processing in relation to the temporal fidelity of MRA reconstruction techniques currently available on the commercial market. This study utilized a numerical phantom that was designed to simulate extreme temporal characteristics rather than likely *in vivo* contrast dynamics.

In Chapter 4, a study is described that was designed to test the temporal and spatial fidelity of HYPR reconstruction using real, acquired data from a physical, computer-controlled phantom that mimics the contrast dynamics confronted in MRA of the peripheral arteries. The consequences of and potential artifacts caused by using the image processing technique with sub-optimal parameters is also investigated and discussed.

Chapter 5 contains a description of a project in which a hybrid three-dimensional radial k-space acquisition was developed with coil-by-coil data-driven parallel imaging and HYPR processing and used to acquire MRA exams from healthy volunteers.

Chapter 6 is an account of the development of a robust imaging protocol for a truly three dimensionally radial k-space acquisition and HYPR reconstruction. This protocol was used to acquire time-resolved, contrast-enhanced MR angiography datasets from healthy volunteers. Furthermore, this chapter discusses the application of the technique to imaging of patients with PAD using a fractional dose of gadobenate dimeglumine contrast agent.

Chapter 7 is a description of a study designed to test the clinical benefit of the radial k-space acquisition and HYPR reconstruction protocol in a cohort of patients with PAD. Magnetic resonance angiography exams using a commercially available Cartesian view-sharing technique were also conducted on these patients. Additionally, these patients

underwent x-ray digital subtraction angiography exams by surgeons in the University of Wisconsin Vascular Surgery Department. The ability to see and diagnosis stenoses in vessel segments from images produced by each MRA technique was tested and the agreements on the presence of significant disease and the assigned stenosis grades were calculated.

Chapter 8 is a summary that addresses the scope and impact of this work. Thoughts on future work are also expressed.

Chapter 2: Background

2.1 Clinical Background

Atherosclerotic vascular disease (AVD) is one of the most common causes of morbidity and mortality in the United States and throughout the world. AVD is characterized by hardening, stiffening and narrowing of the arteries due to the buildup of fatty deposits called plaque. Peripheral artery disease (PAD) is one of the many specific manifestations of AVD and most commonly affects the arteries of the lower extremities. As of 2006, 12 million people in the United States were living with a diagnosis of the disease(1). PAD primarily affects the elderly and consequently patients on Medicare, see Figure 2.1(2). Alarmingly, the annual total Medicare cost of PAD treatment is reported to be as high as $3.87 billion. While only 6.4% of patients with PAD require and receive in-patient care, 88% of the total Medicare PAD cost is associated with PAD-related hospitalizations due to surgical interventions or amputations(3). If this grossly under-

diagnosed and under-treated disease could be identified and intervened upon earlier, before severe disease has manifested to a point that renders less invasive treatments insufficient, PAD would become a significantly smaller financial burden on the Medicare system. Furthermore, as the average age of the general population increases and the obesity and diabetes epidemic continue, the disease is expected to become even more prevalent.

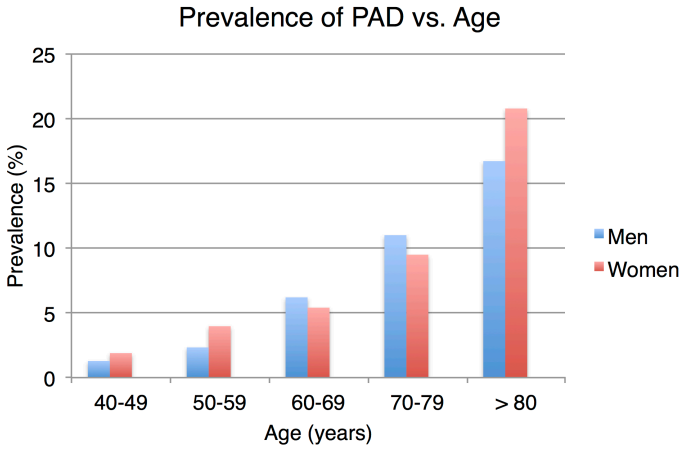

Figure 2.1: Prevalence (%) of PAD vs. age (years) for men and women in the United States. Data are from Allison, et al.

One common symptom of PAD is intermittent claudication, which includes pain, numbness and aching in the legs. This may occur during exertion or rest. Other symptoms include: decreased pulse is the legs or feet, pale or bluish skin color in the legs or feet, low limb temperature, tissue loss and ulceration. However, the disease can also be asymptomatic; of patients with PAD, only 10% to 30% experience classic intermittent claudication(4). The diagnosis of even asymptomatic disease is meaningful, however, since AVD in one vascular territory is associated with an increased risk of the disease in other territories; patients with PAD have a 4-fold increased risk of myocardial

infarction and a 2 to 3-fold greater risk of stroke than patients without PAD(4). Unfortunately, PAD remains both under-diagnosed and under-treated.

Treatment for PAD can include lifestyle changes like improvement of diet and increased exercise. However, if the disease has reached the stage where pain is present with exertion, exercise may be difficult. Modification of risk factors like hyptertension, smoking and diabetes can also be effective. Systemic treatment - anti-platelet drugs, for example - have been shown to reduce adverse cardiovascular outcomes like myocardial infarction or stroke. Endovascular treatments are often utilized in patients with a relatively small number of stenosis that are short in length. Surgical revascularization is also an option in cases that involve long stenotic lesions, numerous short stenotic lesions or critical limb ischemia(5,6).

Besides a thorough medical history and complete physical examination focusing on the cardiovascular system, an ankle-brachial index (ABI) test is a common, non-invasive diagnostic tool for PAD(7). The ABI is the ratio of blood pressure measured in the leg to the blood pressure measured in the arm. For the ABI diagnostic test, these parameters are most often measured by Doppler ultrasound(8). In healthy patients, this ratio should be slightly greater than or equal to 1.0. However, due to artery blockages that are characteristic of PAD, an ABI less than 1.0 can be a predictor of disease(9).

In some cases, to confirm a PAD diagnosis, to visualize the severity of the disease, or to determine the location of blockages for surgical revascularization planning, anatomical

imaging of the vessels may be necessary. Imaging modalities must have high spatial resolution in order to confidently visualize and diagnose stenotic vessel segments. Also, adequate artery vein separation must be demonstrated. The anatomy in the lower legs is such that the veins run directly posterior to the main arteries. The enhancement of both arties and veins in a coronally oriented image can lead to overestimation of the arterial lumen and misdiagnosis of stenosis severity. Sufficient artery-vein separation is usually achieved by a high temporal resolution of the imaging modality so that an angiogram can be acquired such that contrast material or image signal is present in the arteries only.

X-ray digital subtraction angiography (DSA) has been the reference standard for imaging of the peripheral arteries due to both high spatial and temporal resolutions(10). However, an intra-arterial injection of iodinated contrast agent is required, which can necessitate post-procedure observation and/or hospitalization. At many institutions, DSA is no longer being used as a diagnostic tool, but rather a tool to aid in interventions such as endovascular treatment or revascularization. Computed tomography angiography (CTA), which requires iodinated contrast agent via an intravenous injection, has been used as an imaging modality for the assessment of PAD(11). Specifically, multi-row CTA provides high volumetric spatial resolution and total longitudinal coverage of the legs. However, the accuracy of CTA is significantly hampered in the presence of severely calcified arteries(12-14). Also, in both DSA and CTA the patient is subject to potentially harmful amounts of ionizing radiation.

2.2 Magnetic Resonance Angiography

Magnetic resonance angiography (MRA) has been an increasingly important tool for vascular imaging of the peripheral arteries. Techniques that rely upon Gadolinium-based contrast agents (GBCA) to shorten the spin-lattice relaxation time of blood (i.e. contrast-enhanced methods) are currently the most robust.

Due to concerns over the correlation between administration of GBCA and the development of nephrogenic systemic fibrosis (NSF)(15-18), a significant amount of effort has been applied to designing robust, non-contrast-enhanced methods for peripheral angiography(19-25). The slow, variable and sometimes retrograde blood flow in the lower extremities – especially with disease present – can significantly complicate non-contrast methods that rely on flow to obtain endogenous contrast. To date, few of these methods have proven to be as robust as the contrast-enhanced methods that continue to be the gold standard for peripheral MRA.

It should be noted that the incidence of NSF has been shown to be contrast agent dose dependent. In a large, retrospective study of the occurrence of NSF within two major medical centers over ten years, 0.17% of patients who received a high dose of gadolinium-based contrast agent (0.2 – 0.4 mmol/kg) developed NSF. There were no cases in patients who received the standard dose (0.1 mmol/kg)(15). The feasibility of performing time-resolved contrast-enhanced peripheral MRA exams with less than a standard dose of contrast agent (< 0.1 mmol/kg) is discussed in Chapter 6.

Several of the time-resolved, contrast-enhanced methods that are currently available commercially rely upon a view-sharing data acquisition and reconstruction scheme to increase the frame update rate of the time series(26-28). Three-dimensional time-resolved imaging of contrast kinetics (TRICKS)(26) is the commercially-available contrast-enhanced MRA technique currently utilized by University of Wisconsin Hospital and Clinics for peripheral angiography, and is discussed in more detail below.

2.2.1 Time-Resolved Imaging of Contrast Kinetics

Three-dimensional TRICKS, like many other time-resolved, contrast-enhanced angiography techniques(27,29), uses a view-sharing acquisition and reconstruction algorithm. During acquisition, certain segments of k-space data in each time interval are systematically left un-acquired to improve the frame rate. During reconstruction, the missing k-space data are either borrowed or interpolated from neighboring time frames.

Figure 2.2 (from Korosec, et al.) shows the TRICKS k-space acquisition pattern and the reconstruction routine. The A region of k-space represents the low spatial frequencies and is updated during every other time interval. Therefore, a high percentage of the contrast information is updated at a relatively high rate. K-space sections B, C and D represent increasing spatial frequencies and are sampled at lower rates. The success of the TRICKS technique relies on the assumption that high spatial frequency information in a contrast-enhanced angiography exam is 1) generally of less importance than low spatial frequency data and 2) less likely to change significantly at a high temporal rate.

Therefore, to save acquisition time, high spatial frequency information is not sampled with the same update rate as low spatial frequencies.

The fundamental idea behind view-sharing techniques like TRICKS – that high spatial frequencies are less influential in a contrast-enhanced angiography image – is typically valid. However, a view-sharing technique like TRICKS dramatically increases the total amount of un-weighted temporal information included in a single time frame. The total amount of time represented by the un-weighted data used to reconstruct a single time frame is much longer than the frame update rate. This can lead to artifacts and errors in the temporal accuracy of the exam.

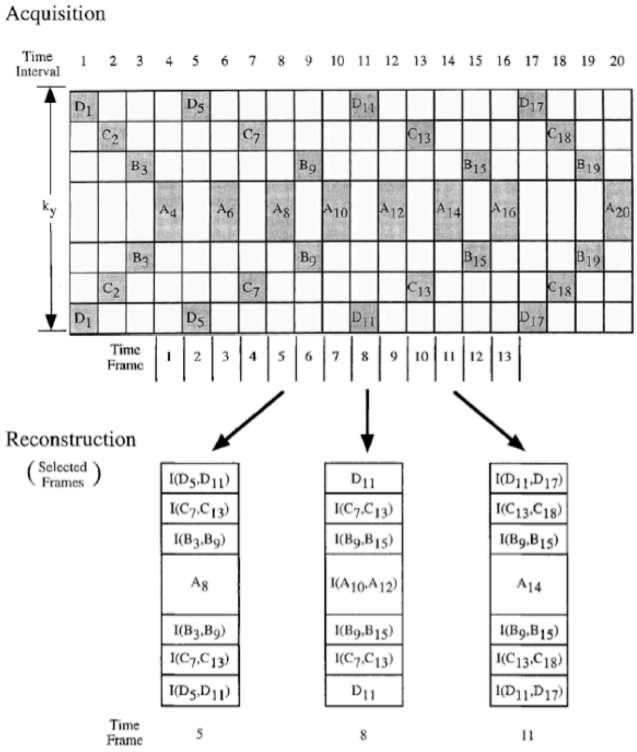

Figure 2.2: Schematic diagram of the acquisition and reconstruction algorithm for Time-Resolved Imaging of Contrast Kinetics (TRICKS). Figure is from Korosec, et al.

2.3 Radial k-Space Sampling

2.3.1 Introduction

Radial k-space acquisition and projection reconstruction was one of the first data acquisition techniques used in MR imaging(30). However, due to initial hardware and computation challenges, acquisition methods evolved to Cartesian-based techniques where parallel lines of k-space are acquired to fill a Cartesian grid. Radial sampling has many well-understood benefits compared to Cartesian sampling. Due to the acquisition of the center of k-space during every repetition time and the subsequent low spatial frequency signal averaging, radial sampling is less susceptible to motion artifacts(31). The penalties resulting from not meeting the Nyquist criterion are more benign than the coherent aliasing artifacts that arise from undersampling in Cartesian space(32). Also, since there is no phase encoding in plane, spatial resolution in radial sampling is most dependent upon readout length, which is not a significant contributor to imaging time. This characteristic allows for the ability to image rapidly while maintaining relatively high spatial resolution and acceptable levels of artifact. These benefits, along with MR hardware improvements and computational advances(33-36), are responsible for renewed interest in the radial sampling technique among researchers within the last decade. Specific details and benefits of two radial acquisition techniques used in this work are described below.

3.3.2 Hybrid 3D Radial Acquisition

The hybrid 3D radial acquisition – also called stack-of-stars (SOS) – is a k-space sampling method in which data are sampled along radial trajectories in the k_x-k_y plane and phase encoding is employed in the k_z direction. Figure 2.3 shows this pattern.

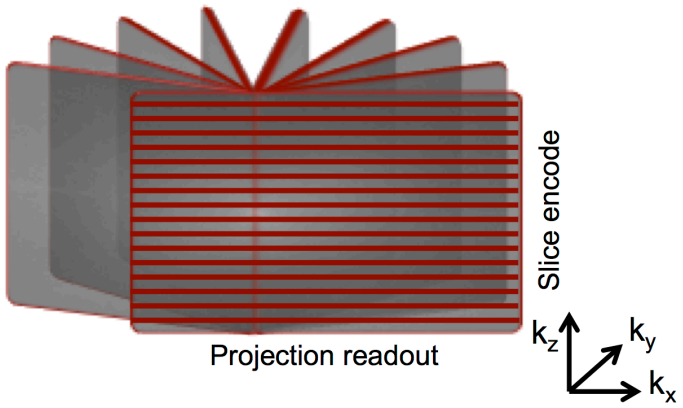

Figure 2.3: Diagram of the stack-of-stars (SOS) k-space acquisition trajectory. Radial sampling is employed in the k_x-k_y plane, while Cartesian phase encoding is employed in the slice direction.

A fully-sampled SOS dataset necessitates the acquisition of $\frac{\pi}{2}$ times more data than a corresponding Cartesian acquisition, due to the divergent nature of the radial projections at high spatial frequencies. However, as noted above, radial aliasing artifacts due to the acquisition of too few projections are relatively benign compared to the deterministic and coherent aliasing that occurs in Cartesian undersampling. When radial undersampling is employed, high intensity streak artifacts radiate from areas of signal. While these streak artifacts may interfere with other structures in the image, they will not obstruct the object from which they originate; around every point object in the image, there is an artifact free FOV (rFOV), the extent of which is determined by the amount of undersampling:

Equation 2.1

$$rFOV = FOV \cdot \left(\frac{N_p}{N_r}\right) \cdot \left(\frac{2}{\pi}\right).$$

Along with the high acceleration factors possible with radial undersampling, the SOS trajectory is also compatible with Cartesian parallel imaging in the phase-encoding direction. Parallel imaging strategies for non-Cartesian trajectories are currently a focus of many investigators(37,38). While many algorithms exist, few have proven as robust as Cartesian, data-driven techniques and will not be considered in this work.

2.3.3 True 3D Radial Acquisition

Vastly undersampled isotropic projection reconstruction (VIPR) is a true 3D radial k-space trajectory; radial sampling occurs over the whole k_x-k_y-k_z volume as shown in Figure 2.4(39). Endpoints of each projection are distributed over the surface of a sphere. The equation for the artifact free FOV (rFOV) for a VIPR acquisition is:

Equation 2.2

$$rFOV = FOV \cdot \left(\frac{N_p}{N_r^2}\right) \cdot \left(\frac{2}{\pi}\right).$$

Again, VIPR acquisition requires $\frac{\pi}{2}$ times more data than a similarly sized Cartesian volume to be considered fully-sampled (i.e. when $\frac{rFOV}{FOV} = 1$). However, the penalties for not meeting the Nyquist criterion are even more benign than the undersampling artifacts in an SOS image. Streak artifacts are present in an undersampled VIPR image; however, the artifacts are spread into three dimensions, making them less structured and more noise-like. This property can facilitate higher undersampling factors and, consequently, increased temporal resolution. Because of the consistent radial sample

spacing (Δk_ϕ and Δk_θ) throughout k-space, VIPR trajectories are considered to be more naturally suited for imaging of isotropic volumes.

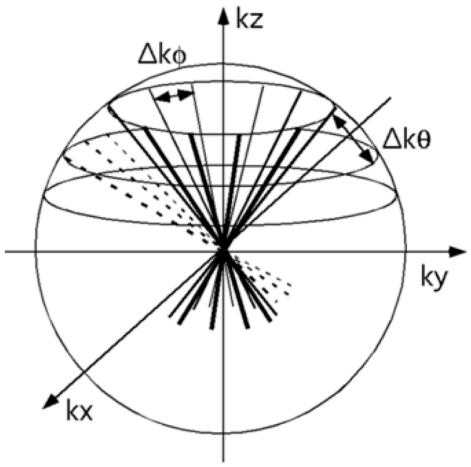

Figure 2.4: Diagram of the vastly undersampled isotropic projection reconstruction (VIPR) k-space acquisition trajectory. Figure is from Barger, et al.

2.4 Highly Constrained Backprojection Reconstruction Techniques

2.4.1 Introduction

Highly constrained backprojection (HYPR)(40) is an image reconstruction algorithm that exploits image sparsity and spatio-temporal correlation to obtain high quality time-resolved images from significantly undersampled data. Time-resolved contrast-enhanced MR angiography is a well-matched application for the HYPR algorithm because the subtraction of a pre-contrast mask results in a dataset that meets the sparsity recommendations. Many authors have applied HYPR reconstruction to MRA(41-43) and have demonstrated that HYPR processed images exhibit a decrease in undersampling artifact and high signal-to-noise (SNR) ratios compared to corresponding, non-HYPR-processed time frames.

The HYPR reconstruction process involves the creation and manipulation of two fundamental images: the composite image and the weighting image. Since the initial introduction of the technique, modified HYPR algorithms have been proposed, which differ from the original algorithm in the manner in which the weighting image is created. In this section, the original HYPR algorithm and two such modifications are examined and considered. It should be noted that while the HYPR technique is adaptable to interleaved variable density Cartesian acquisitions(44), this work focuses on the original, intended application of the algorithm – interleaved, radially undersampled data.

2.4.2 Original HYPR Reconstruction

A schematic diagram of the original HYPR reconstruction algorithm is shown in Figure 2.5. A composite image is formed by one-dimensional Fourier transform and filtered backprojection (FBP) of either all or a significant subset of the acquired k-space projections. The result is a well-sampled anatomical image with high SNR due to the long data acquisition time, high spatial resolution and few undersampling artifacts. The composite image has little or no temporal information, but contains detailed structural information pertaining to the anatomy.

The weighting image is unique for each desired HYPR time frame and in the original HYPR algorithm is calculated by normalizing each image space projection – obtained by a one-dimensional Fourier transform of the k-space projection – in a given time frame interleave by the corresponding projection angle that is re-sampled from the time

averaged composite image. The desired number of normalized projections is then backprojected with no filtering. Note that the unfiltered backprojection (UFBP) process will result in a significant loss of spatial resolution. Also, the weighting image is highly undersampled at high spatial frequencies, and therefore suffers from streaking artifacts. However, the temporal resolution of the weighting image is very fine and the SNR is high.

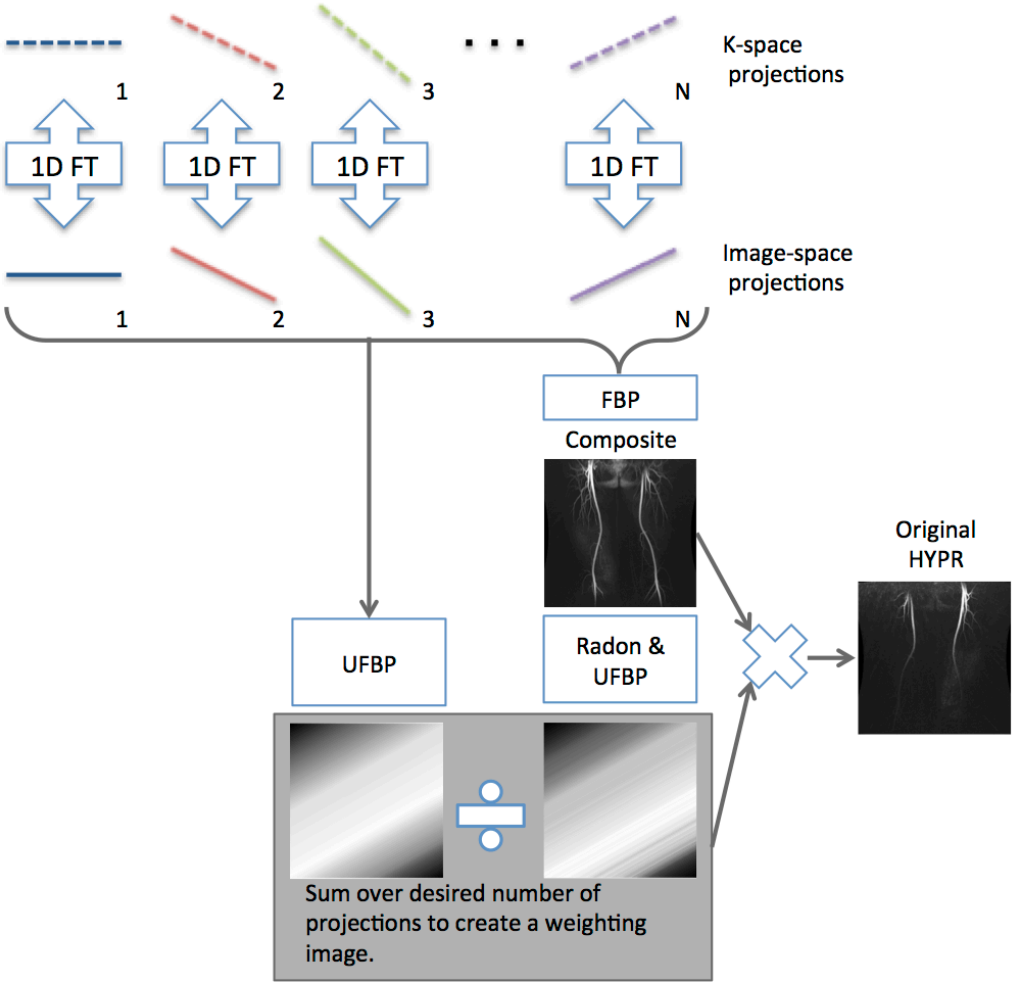

Figure 2.5: Schematic diagram of the Original HYPR algorithm.

Multiplication of the composite image and the weighting image is the final step of the HYPR algorithm. Signal arising from either undersampling artifacts or the unfiltered

backprojection of data that enhances areas of the weighting image beyond the borders of the vascular system will be suppressed by the near zero signal values in the corresponding pixels of the composite image. Dynamic information describing the true temporal kinetics of the image series will be bright in the weighting image and will be enhanced when multiplied with the composite image. The original HYPR process can be written mathematically as:

Equation 2.3

$$I_H(t) = I_C \cdot I_W(t) = I_C \cdot \frac{1}{N_{pr}} \sum_{i=1}^{N_{pr}} B\left(\frac{P_t^i}{P_C^i}\right)$$

where I_C is the well-sampled composite image; $I_W(t)$ is the unique weighting image for time frame t; P_t, denotes the set of image space profiles for time frame t; P_C is the corresponding set of projections sub-sampled from the composite image, N_{pr} is the number of projections per time frame, and $B()$ denotes the unfiltered backprojection process. Note that in the original HYPR technique, projections are normalized prior to backprojection.

2.4.3 Image-Based HYPR Reconstruction

Huang, et al.(41) published a modified version of the HYPR algorithm referred to in this work as Image-Based HYPR. The modified algorithm can be expressed as:

Equation 2.4

$$I_H(t) = I_C \cdot I_W(t) = I_C \cdot \left(\frac{\sum_{i=1}^{N_{pr}} B(P_t^i)}{\sum_{i=1}^{N_{pr}} B(P_C^i)}\right).$$

A schematic diagram of Image-Based HYPR is shown in Figure 2.6. In this case, the entire interleave of k-space projections for a given time frame is one-dimensionally Fourier transformed and backprojected with no filter prior to the normalization step. The image created by the time frame projections is normalized by a similar image formed by the summation of corresponding unfiltered, backprojected projections re-sampled from the composite image. Note the difference between the original HYPR algorithm and Image-Based HYPR is the order in which normalization and backprojection steps are performed to create the weighting image.

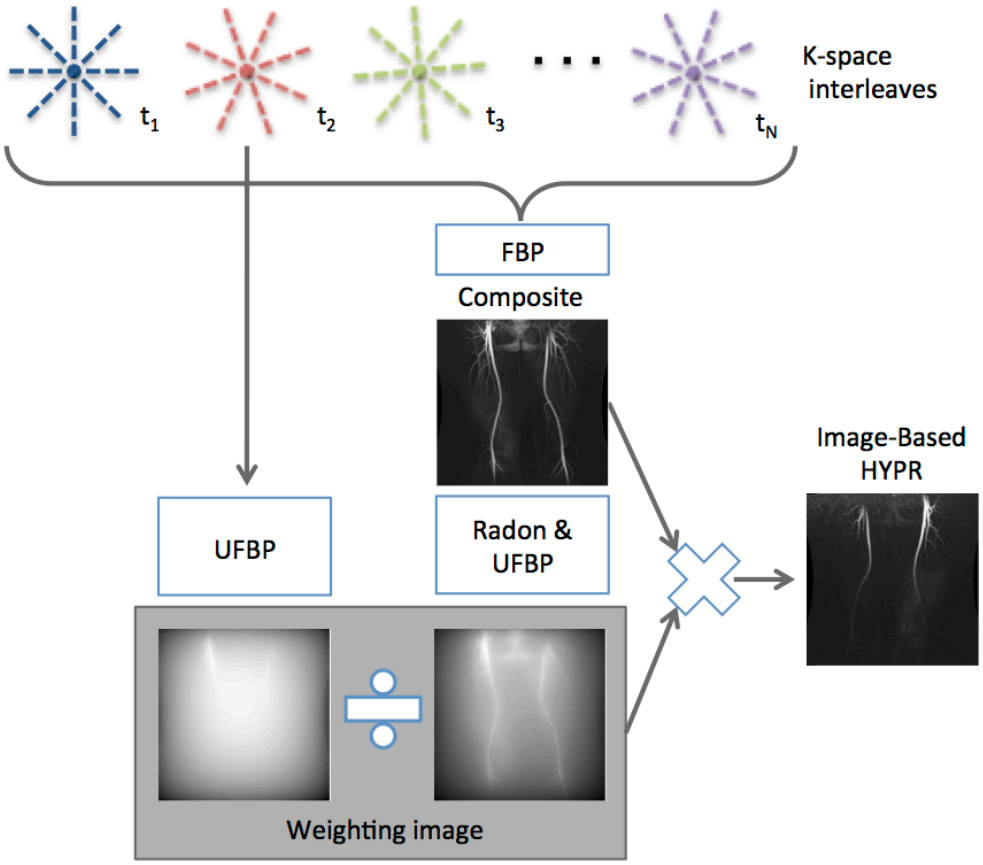

Figure 2.6: Schematic diagram of the Image-based HYPR algorithm.

The motivation behind Image-Based HYPR stems from the concept that, as the number of projections in a time frame interleave increases towards the total number of

projections in the dataset, the HYPR image should become equal to the composite image; the weighting image should be of unit value. In Equation 2.4, as the image formed by $B(P_t)$ approaches $B(P_C)$, it is clear that I_W will approach 1. This is not necessarily the case in the original HYPR algorithm. Assume N_{pr} is equal to the total number of projections and there is only one time frame. In the original HYPR algorithm, for a given projection, k, the value $\left(\frac{P_1^k}{P_C^k}\right) \neq 1$ is backprojected. $P_1{}^k$ will contain the data collected only during the acquisition of the kth projection. $P_C{}^k$, however, is a projection from the re-sampled composite image and will contain temporal information that has been time-averaged from the entire scan. In this theoretical limit, the normalization step in the original HYPR algorithm will not result in a weighting image of unit value, but in the Image-Based HYPR it will.

2.4.4 HYPR Local Reconstruction

Mathematically, the HYPR LR reconstruction algorithm can be written as:

Equation 2.5

$$I_H(t) = I_C \cdot I_W(t) = I_C \cdot \frac{\Phi(k_t)}{\Phi(k_{C,t})}.$$

HYPR LR is similar to Image-Based HYPR in that the normalization step of weighting image formation is performed on images, rather than projections (see Figure 2.7 for a schematic diagram). The difference between HYPR LR and Image-Based HYPR lies in how the normalization images are created. In the HYPR LR equation, Φ represents a reconstruction technique for k-space data from the time frame t (k_t) and the re-sampled composite ($k_{C,t}$). The reconstruction technique (Φ) may vary for different data acquisition

trajectories, but should be chosen based on its ability to reduce aliasing artifacts and improve SNR relative to the corresponding non-HYPR processed image. In many cases, that corresponds to a low spatial resolution reconstruction of the data.

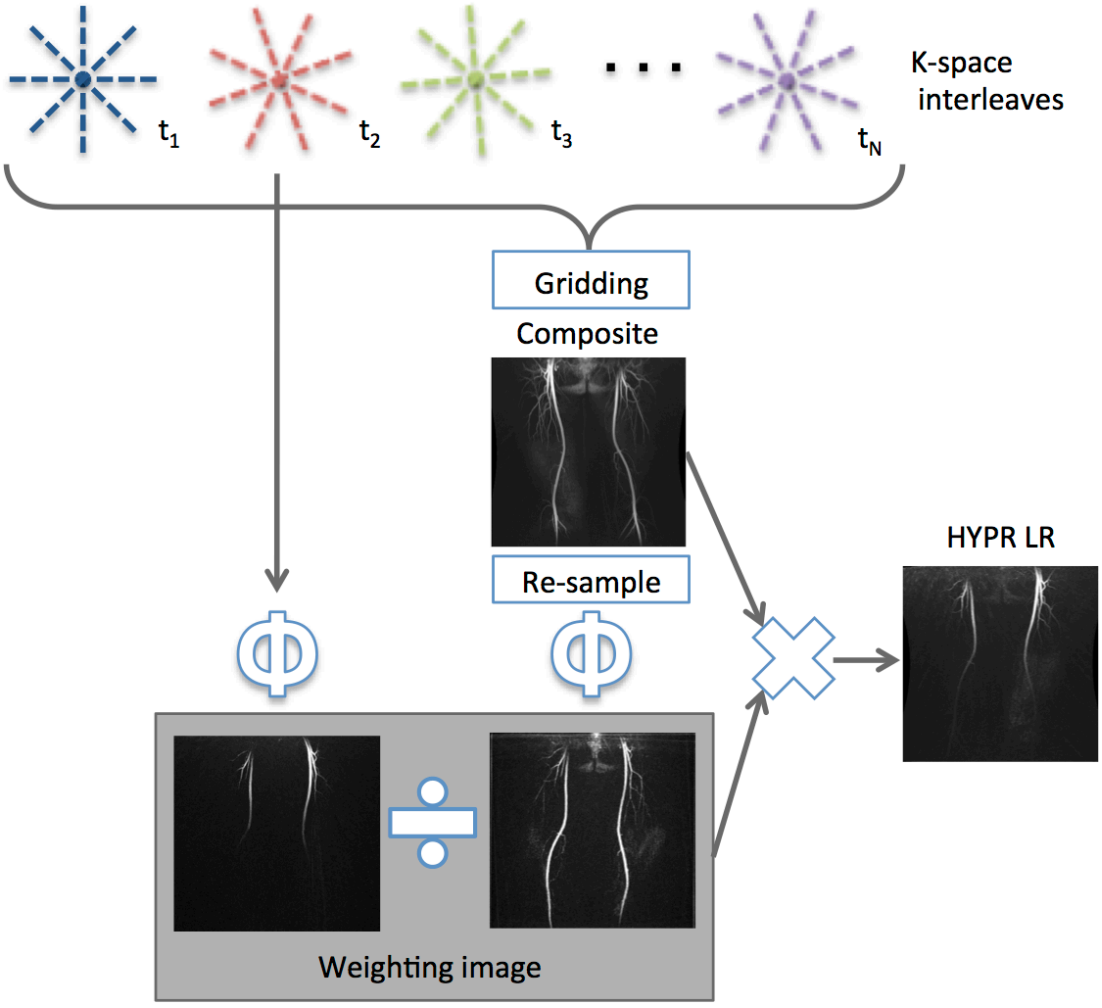

Figure 2.7: Schematic diagram of the HYPR LR algorithm.

2.4.5 HYPR Reconstruction: Other Considerations

An early criticism of the original HYPR technique is the possibility of inadvertent enhancement of structures that should not be enhanced in instances where the dataset

is not sufficiently sparse or the spatio-temporal correlation is weak. This error is commonly referred to as signal cross-talk. The unfiltered backprojection performed in the creation of the weighting image can result in bright signal in areas of the anatomy that have yet to truly receive contrast material. If these areas are outside of the border of the vascular system, multiplication by the corresponding low signal in the composite image will significantly suppress the erroneous signal. However, if the backprojected signal in the weighting image overlaps vascular anatomy in the composite image, premature enhancement of the vessels in the reconstructed time frame can result.

The use of a sliding window composite image can mitigate this error(42). A sliding window composite is created with only a subset of the data collected throughout the exam – not the entirety of it. Usually, the data from the time frame being reconstructed are temporally in the center of the sliding window; an equal amount of data are used from before the time frame of interest as after. By time averaging less data, the image sparsity is greater in a sliding window composite than in a full composite. Also, the vessels that are bright are more temporally relevant to the time frame being reconstructed. Therefore, there are more pixels of low signal intensity in the composite image that will dampen erroneously bright signal in the weighting image. When creating a sliding window composite, the amount of data included from low and high spatial frequencies need not be the same; more high spatial frequency information can be averaged than low spatial frequency data(45). A tradeoff exists, however, between a temporally smaller composite image and an increasingly undersampled one. Increased

undersampling will result in more and higher intensity streaking artifacts in the composite image, which can nullify the benefit of the sliding window composite.

Local HYPR reconstruction (HYPR LR)(46) mitigates the cross-talk issue by creating the weighting image in an alternative fashion, effectively localizing the weighting image blur. In the HYPR LR reconstruction, the weighting image projections are filtered prior to backprojection. The filter is chosen to reduce the weighting image undersampling artifacts and increase image SNR. In most cases, this corresponds to a low-pass filter that reduces the weighting image spatial resolution. Filtering the weighting image projections minimizes the potential for signal cross-talk when using a fully sampled composite image.

Chapter 3: Simulation of Relative Temporal Response of Time-Resolved MRA Sequences

3.1 Introduction

As elaborated upon in the two previous chapters, there is a significant need for safe, efficient and accurate peripheral vascular imaging methods to aid in both disease diagnosis and interventional treatment planning. Magnetic resonance angiography (MRA) has been widely used as a tool for non-invasive vascular imaging. However, due to the long duration needed to acquire sufficient high spatial frequency data, many conventional MRA methods suffer from poor temporal resolution. Several techniques – termed view-sharing techniques – have been commercially implemented that decrease the scan time necessary for a given time interval by reducing the amount of k-space data

acquired during that time interval. To reconstruct a full, high spatial resolution time frame, data are shared between multiple time intervals.

This work investigates the temporal resolution of three time-resolved MRA methods: Keyhole(47), Time-Resolved Imaging of Contrast Kinetics (TRICKS)(26), both of which are Cartesian view-sharing techniques, and Highly-Constrained Back Projection Local Reconstruction (HYPR LR)(40,46). Temporal resolution in this study is examined by simulating the temporal impulse response of a given image reconstruction process. The temporal impulse response function (IRF) describes how a system responds to an impulse signal present for only a short time constrained to a small area of impulse (AOI); it is analogous to the point-spread function in the spatial domain. The temporal frequency response (TFR) is the temporal Fourier transform of the IRF and describes the system's response to the impulse signal in the temporal frequency domain; it is analogous to the modulation transfer function in the spatial domain. Although a given MRA reconstruction method may have excellent temporal resolution, as described by the IRF and TFR, it may nonetheless suffer from poor spatial resolution. Often times, an increase of resolution in one domain results in a decrease in the other. Therefore, when investigating the temporal resolution of different methods, spatial representation of the AOI is also considered.

3.2 Background

The Keyhole method takes advantage of the characteristics of different regions within k-space and the contributions of those regions to the contrast and edge sharpness of an

image; low spatial frequency data found in the center of k-space contributes to the image contrast, while the high spatial frequency data near the edges of k-space contribute to image sharpness. Acquiring low spatial frequency phase encoded data and zero filling missing high spatial frequency data results in a decreased acquisition time, however, the image is blurred in the phase encoding direction. Keyhole attempts to remedy this by supplementing the low spatial frequency data acquired rapidly during a time interval with high spatial frequency data from a fully sampled reference frame. Although this can produce acceptable images, the degree of acceptability depends on the consistency of the information in the reference frame with the information contained in the time interval being reconstructed. For example, if the reference frame contains high frequency phase encoded data that are not consistent with the data in the rapidly acquired time intervals, the Keyhole method will incorrectly spread the reference frame data to all other frames, resulting in reduced temporal and spatial fidelity.

TRICKS also takes advantage of the contributions of different k-space regions. However, instead of imposing a single high spatial frequency k-space region onto the entire image series, TRICKS systematically acquires high spatial frequency data throughout the acquisition albeit at a slower rate than low spatial frequency acquisition. The advantage of such an approach is that k-space data missing from a given time interval can be estimated by linear interpolation of neighboring k-space data points. In that way, each reconstructed time frame has unique high and low spatial frequency data.

Unlike Keyhole and TRICKS, which are both Cartesian, view-shared techniques, HYPR LR is most commonly applied to a set of undersampled, interleaved radial projections. For the HYPR LR reconstruction, all or a significant subset of the acquired data are combined to reconstruct a composite image via filtered backprojection or gridding and an inverse Fourier transform. The composite image has high SNR and contains little, if any, undersampling artifacts. A series of weighting images are formed using data from each time frame; the final HYPR LR image is a multiplication of the weighting image by the composite image. The HYPR LR process can be represented mathematically as:

Equation 3.6

$$I_H(t) = I_C \cdot I_W(t) = I_C \cdot \frac{\mathrm{F} \otimes I_t}{\mathrm{F} \otimes I_{C,t}}$$

where I_C is the well-sampled composite image; F is a convolution kernel chosen to minimize undersampling artifacts; I_t is a gridded, density compensated and Fourier transformed reconstruction of the time frame image; and $I_{C,t}$ is a re-sampled composite image.

3.3 Methods

The impulse response functions of each method were simulated using a set of identical 512 x 512 pixel x-ray DSA images of the intracranial vasculature. The DSA frame provides a relatively artifact free image and serves to simulate a contrast-enhanced magnetic resonance angiography study of the head. A small 4 x 4 pixel area of impulse (AOI) was prescribed in a non-sparse region; it was surrounded by vessels on all four sides, see Figure 3.1. The value within the AOI for a single time frame of the input series

was set to approximately 1.5 times the maximum signal intensity. The intensity within the AOI was set to zero for all other time frames. Impulse response functions were calculated by measuring the mean signal within the AOI for each frame in the reconstructed time series.

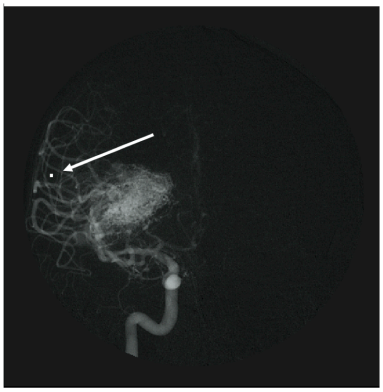

Figure 3.1: A 512 x 512 pixel x-ray DSA image of the head used as input for the simulation. This frame also shows the area of impulse (AOI) (arrow).

As noted above, TFR curves are the Fourier transform of the IRFs. In this investigation, the TFR of each method was normalized to one at zero frequency, since each reconstruction technique would perfectly reconstruct static, non-temporally changing objects. Since the temporal frequency response may depend on AOI size, various size AOIs were examined for certain cases described below.

For the Keyhole simulation, the inner 15% of phase encoded lines were sampled in each frame (labeled *L* in Figure 3.2a). This is consistent with the parameters reported in the literature(27,47) and results in an acceleration factor of 6.6 relative to a fully-sampled Cartesian acquisition. To simulate the temporal frequency response of Keyhole reconstructions, two possible scenarios were addressed. First is the scenario around

which the technique was developed: the impulse signal occurs during the rapid acquisition of low spatial frequency time frame data (referred to as *Case L* for *Low* spatial frequency). In Case L, high spatial frequency reference data will generally be consistent with the time series and the impulse signal will be represented with high temporal fidelity, but low spatial resolution. Second is a scenario that demonstrates the potential for temporally inaccurate reconstructions if high spatial frequency reference data are inconsistent with time frame data: the impulse signal occurs during the acquisition of high spatial frequency reference frame data (referred to as *Case H* for *High* spatial frequency). In Case H, high spatial frequency data from the impulse signal will be imposed on all time frames in the series.

To simulate TRICKS, k-space was divided into three equal regions: A, B and C (see Figure 3.2b). The low spatial frequency region was sampled twice as often as the middle and high spatial frequency regions. The k-space region sampling pattern followed: A, B, A, C, A, B, etc. Linear interpolation was used to estimate missing data for a given time frame in the series. This resulted in an acceleration factor of 3 relative to a fully-sampled Cartesian acquisition. For a TRICKS method with three k-space regions, three unique simulations are necessary, depending on whether the signal impulse occurs during the acquisition of low, middle, or high spatial frequency data.

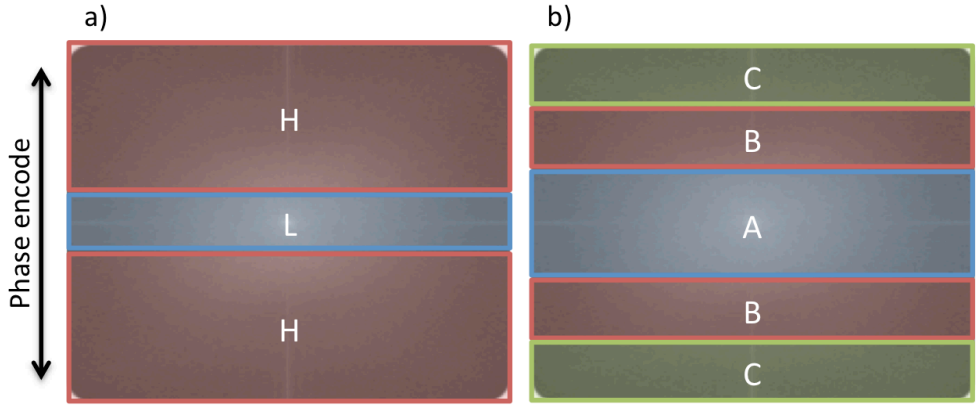

Figure 3.2: a) In the Keyhole simulation the inner 15% of k-space – labeled *L* – is sampled at a high rate, while high spatial frequencies – labeled *H* – are acquired only during a single reference frame. b) In the TRICKS simulation, k-space is divided into three equal regions: *A*, *B* and *C*.

To simulate HYPR LR, 2D k-space data were sampled along radial lines for each time frame. Interleaves consisted of 41 angles, corresponding to an undersampling factor of 10 relative to the Nyquist criteria or 13 compared to a fully-sampled Cartesian acquisition. To form the weighting image, all filtering was done in k-space by a radially-symmetric Gaussian filter that reduced the spatial resolution of the weighting image by a factor of 5. A composite image reconstructed with of all the k-space lines was used.

Since the impulse response function has units of [time frames] on the abscissa, a scaling factor of (seconds / time frame) is needed to convert to the customary unit of seconds prior to applying the Fourier transform. In Fourier space, the scaling for the temporal frequency response function is then the reciprocal of the scaling parameter used for the impulse response function. In this investigation, Keyhole, TRICKS and HYPR LR have update rates of 76, 170 and 41 TRs. Therefore, to account for the different sampling

rates used to measure the IRF, the frequency response functions of Keyhole and TRICKS were compressed by a factor of 1.85 and 4.14 relative to that of HYPR LR.

3.4 Results

Figure 3.3 shows the impulse response functions for both Case L and Case H Keyhole scenarios. In Case L, when the impulse occurred during the acquisition of low spatial frequency data, the impulse response function is nearly ideal. No signal is spread to other time frames, however only 54% of the original signal intensity is reconstructed in the impulse frame. The impulse response function for Case H is very poor; 100% of the signal is reconstructed in the impulse frame, however 45% of the signal intensity is spread to all time frames in the series.

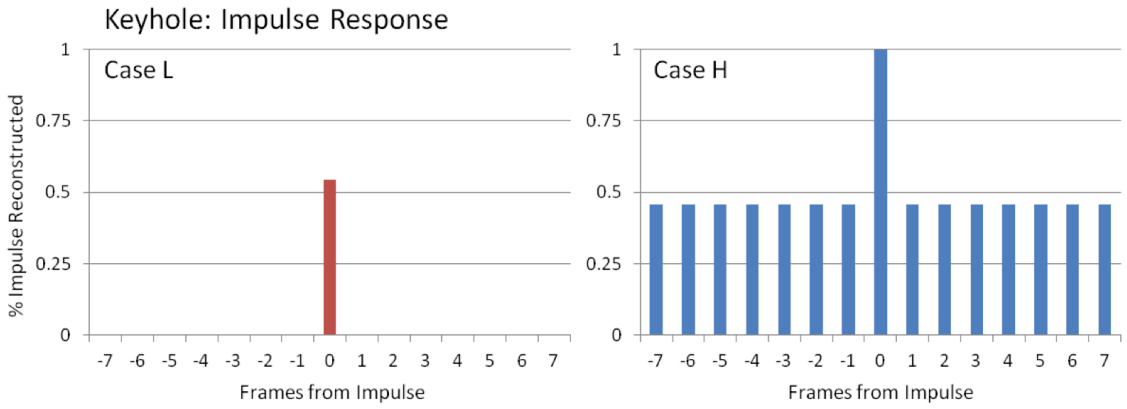

Figure 3.3: Impulse Response Functions (IRF) for Keyhole under scenarios in which the 4 x 4 pixel impulse occurred during the rapid acquisition of low spatial frequency time intervals (Case L) and during the acquisition of the high spatial frequency reference frame (Case H).

The frequency response curves for both scenarios are plotted in Figure 3.4; the results vary drastically depending on whether the signal impulse occurs during the acquisition of reference or time frame data. Figure 3.5 shows cropped and enlarged images of the resulting time frames immediately preceding and including the impulse signal (T_{i-1} and T_i, respectively) for both cases when a 4 x 4 pixel AOI is used in the simulation. Figure 3.6 plots the impulse response functions for both Case L and Case H when the side length of the square AOI is varied. Notice that the depth axes for each three-dimensional plot are opposite. In both cases, Keyhole exhibits the best impulse response when the AOI is large, in other words, when the AOI consists of more low spatial frequency components that are rapidly acquired and updated.

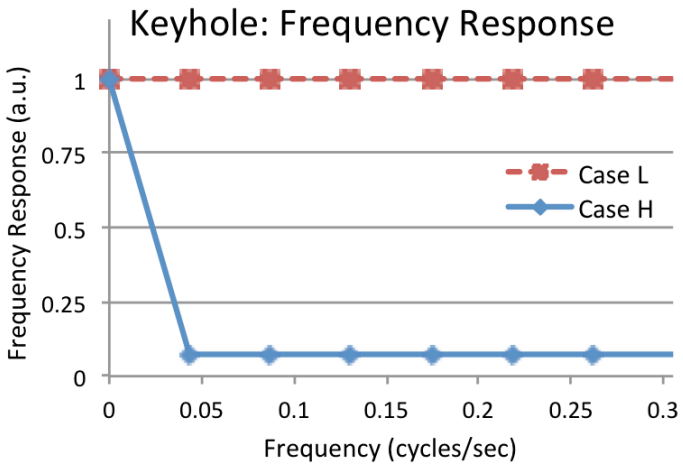

Figure 3.4: Temporal Frequency Response curves for Case L and Case H of the Keyhole simulation. The constant response for Case L indicates that in that scenario, Keyhole exhibits no spreading of the impulse signal in the temporal dimension.

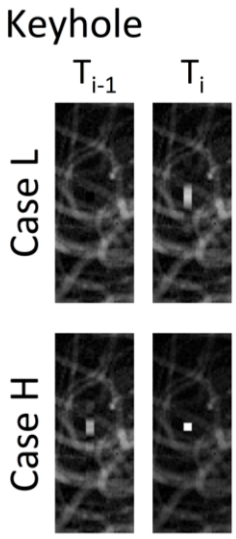

Figure 3.5: Cropped and enlarged images of the time frame preceding the 4 x 4 pixel impulse (T_{i-1}) and containing the impulse (T_i). Note that while Case L exhibits perfect temporal response in Figures 3.3 and 3.4, there is a significant loss of spatial resolution in the phase encode direction (top to bottom in image) in T_i. Conversely, while in Case H the AOI is represented well spatially in T_i, a high-pass filtered representation of the AOI is present in all other time frames.

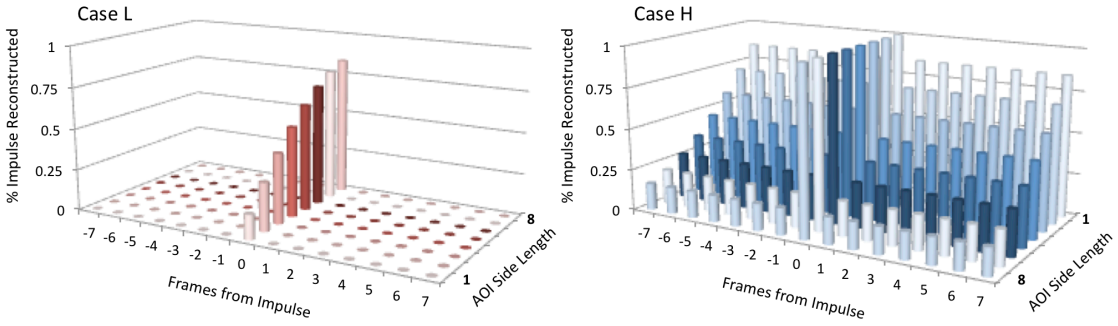

Figure 3.6: Impulse Response Functions for Case L and Case H of the Keyhole simulation with square AOI side lengths of 1 through 8 pixels. Note that the depth axes for each plot are reversed. In both scenarios, impulse response is significantly improved with larger AOI sizes.

Figure 3.7 shows the TRICKS impulse response functions for Cases A, B and C. In Case A, 88% of the impulse signal is reconstructed in the correct time frame, while 44% of the

impulse signal is erroneously spread to either side of the impulse time frame. Impulse response is poor in Cases B and C; note the difference in y-axis scale for the Case B plot. Only 2.8% and 13.6% of the impulse signal is reconstructed in the correct time frame in Case B and Case C, respectively. Low intensity signal is erroneously spread to three frames before and after the impulse frame in both cases. The frequency response curves for all cases are plotted in Figure 3.8 and cropped and enlarged images of TRICKS time frames immediately preceding (T_{i-1}) and including (T_i) the signal impulse are shown in Figure 3.9 for each case when a 4 x 4 pixel AOI is used. Note that the shape of each impulse response function is indicative of the sampling scheme for each region in k-space and the linear interpolation performed to approximate the missing k-space data. Therefore, the shape of the impulse response curve will not change for different size AOIs. However, the impulse reconstructed signal intensity will vary. Figure 3.10 plots the AOI signal intensity in the impulse frame for Cases A, B and C when square AOIs of various side lengths are used in the simulation.

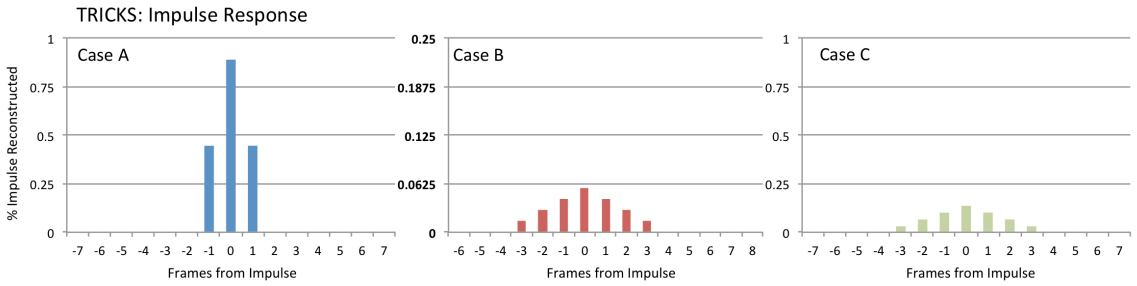

Figure 3.7: Impulse Response Functions for scenarios in which the impulse occurred during the acquisition of the center, middle and outer k-space regions (Cases A, B and C, respectively). Note the different y-axis scale in the plot for Case B; only 2.8 % of the input impulse intensity is reconstructed in the impulse frame.

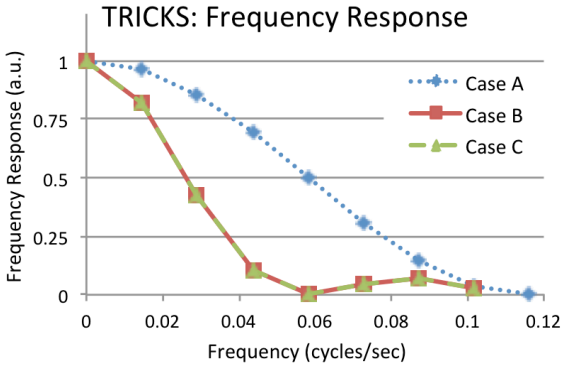

Figure 3.8: Temporal Frequency Response curves for each case in the TRICKS simulation. In each scenario, TRICKS exhibits a spread of impulse signal in the time dimension, the severity of which depends on when the impulse occurs.

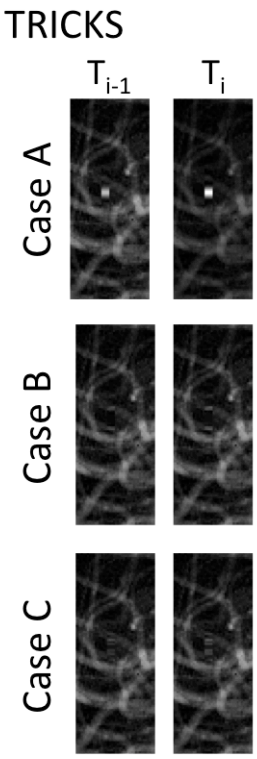

Figure 3.9: Cropped and enlarged images of the time frame preceding the impulse (T_{i-1}) and containing the impulse (T_i). In Case A, the AOI is well represented in the impulse frame, however a low spatial resolution representation of the AOI is spread to the preceding time frame. The AOI cannot be easily distinguished in either frame T_{i-1} or T_i in Case B and Case C. Small amounts of ringing artifact can be seen in these cases. This is due to information that is inconsistent between k-space regions.

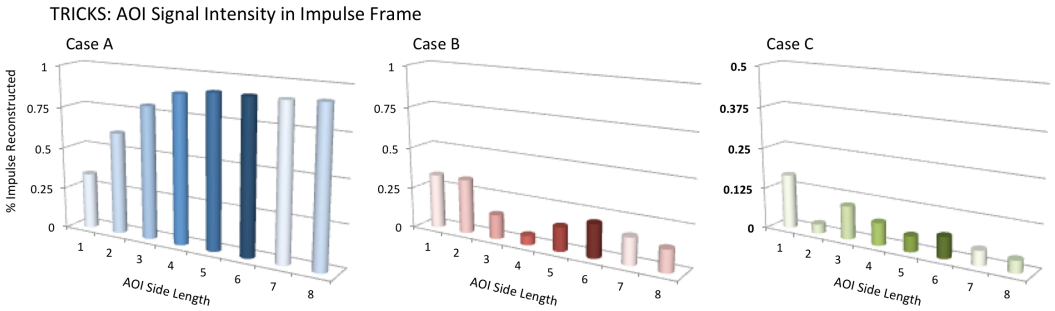

Figure 3.10: Plots of the signal intensity (reported as the percent of the input impulse intensity) of the reconstructed impulse in the impulse frame for Cases A, B and C when different size AOIs were used in the simulation. Note the different y-axis scale for Case C. When the impulse occurs during the acquisition of B or C k-space region, impulse response is poor for all AOI sizes simulated. For Case A, impulse response significantly deteriorates for AOI sizes smaller than 4 x 4 pixels.

The HYPR LR impulse response function is plotted in Figure 3.11. Seventy percent of the impulse signal is reconstructed in the correct time frame and the remaining frames contain comparatively little signal within the AOI. Since little signal was spread to neighboring frames, the frequency response curve (Figure 3.12) is nearly constant for all frequencies. Figure 3.13 shows cropped and enlarged images of HYPR LR time frames before and during the signal impulse (T_{i-1} and T_i). Impulse response results for the simulation with varying side lengths of a square AOI are shown in Figure 3.14.

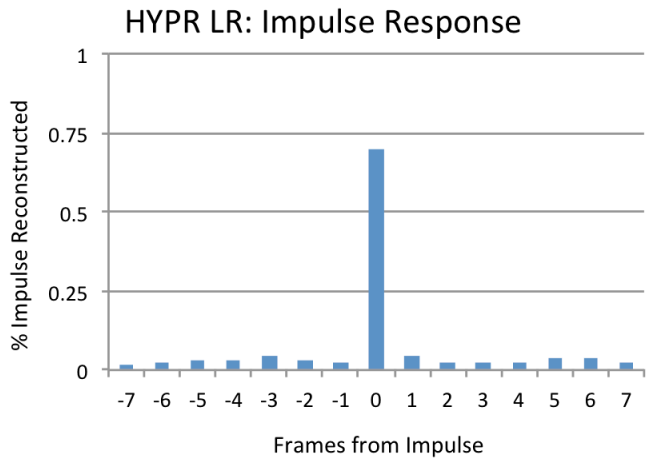

Figure 3.11: Impulse Response Function for the HYPR LR simulation with a 4 x 4 pixel AOI. Seventy percent of the input impulse intensity is reconstructed in the impulse frame with minimal spreading of signal in the time dimension.

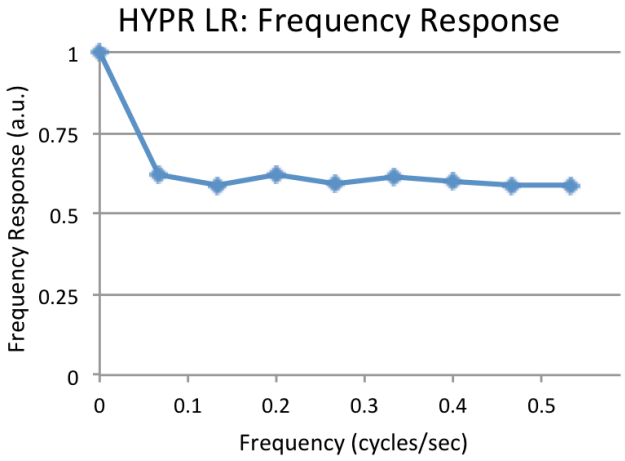

Figure 3.12: Temporal Frequency Response for the HYPR LR simulation.

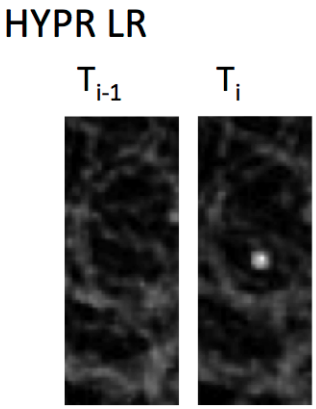

Figure 3.13: Cropped and enlarged images of the time frame preceding the impulse (T_{i-1}) and the frame containing the impulse (T_i). The AOI is represented well in the impulse frame with no detectable spreading of the signal in the temporal domain.

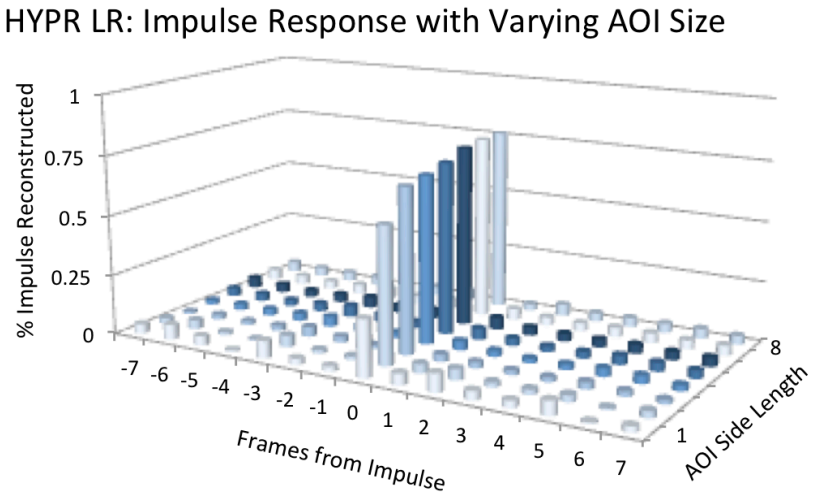

Figure 3.14: Impulse Response Functions for the HYPR LR simulation when different sized AOIs were used. The HYPR LR IRF is consistent for all AOI sizes above 2 x 2 pixels.

3.5 Discussion

Case L is the ideal scenario for the Keyhole method. The temporal impulse response is nearly perfect. In the simulation with a 4 x 4 pixel AOI, however, only 54% of the original impulse intensity is reconstructed. It has been shown in Figure 3.6 that this response improves with increasing AOI size (and conversely deteriorates with decreasing AOI size). With an 8 x 8 pixel AOI, 84% of the impulse signal intensity is reconstructed. With a 1 x 1 pixel AOI, only 15% of the original impulse intensity is reconstructed. While the temporal behavior of the impulse signal is well represented in this case, the spatial representation of the AOI is significantly degraded (see frame T_i for Case L in Figure 3.5). This is expected since only low spatial frequency data were acquired during the impulse. Even in the ideal scenario for the Keyhole reconstruction technique, there is a trade-off between spatial and temporal resolution.

The impulse response function for Case H of the Keyhole simulation can be modeled as:

Equation 3.7

$$IRF_{CaseH}(t) = \left(C_L \delta_{t,t_i} + C_H\right)$$

where C_H is a constant term imposed onto every frame the value of which originates from the high spatial frequency contribution of the reference frame; C_L is the result of contributions of low spatial frequency data from the time frame, and $\delta_{t,ti}$ is the Kronecker delta. The value of the two constants C_H and C_L depend on the spatial frequency content of the AOI; smaller objects have larger C_H, whereas larger objects have larger C_L. In the simulation with a 4x4 pixel AOI, 45% of the signal intensity is erroneously spread to all

time frames in the series. However, in the limit of large objects, for which the high spatial frequency component is minimal (corresponding to a small C_H in Equation 3.2), the impulse response function – and the frequency response curve – will improve. In the simulation with an 8 x 8 pixel AOI, 16% of the impulse intensity is spread to all time frames. While the impulse response of Keyhole in Case H is poor, response functions improve with increasing AOI size.

In Case H, Keyhole reconstructed the AOI with high spatial resolution for the impulse frame. In all other frames, spatial representation of the AOI in the phase encoding direction was severely degraded due to high spatial frequency reference data that were inconsistent with the low frequency time frame data.

The impulse response function for TRICKS can be modeled as a discrete representation of:

Equation 3.8

$$IRF_{TRICKS}(t) \propto tri\left(\frac{t}{r_s}\right)$$

where 'tri' is a triangle function of width $2r_s$ and r_s is the sampling rate for the region being sampled when the impulse occurred; r_s=1 for the Case A and 3 for Cases B and C. The proportionality constant depends on both the case being considered as well as the spatial frequency content of the AOI being simulated. For example, in Case A, the proportionality constant is larger for objects with large low spatial frequency components; the AOI signal intensity in the impulse frame is higher (92% of the input signal) for larger AOIs. The shape of the IRF remains constant, however, regardless of the AOI size.

If the impulse response function is a triangle function, the temporal frequency response function is the discrete representation of:

Equation 3.9

$$TFR(f) = sinc^2(r_s f),$$

with the limiting temporal frequency is defined as $1/r_s$. It is now clear that the best temporal frequency response curve will occur during Case A, since r_s is the smallest for this scenario.

The spatial representation of the AOI associated with TRICKS varies drastically depending on when the impulse occurred. If the impulse occurred during the acquisition of middle or high spatial frequency data, only very low signal intensity is reconstructed in the correct frame. This signal is virtually non-existent in the images (Figure 3.9). If the impulse occurred during the acquisition of the A k-space region, a low spatial resolution representation of the AOI can be seen in the image.

In this study, HYPR LR performs with temporal resolution and spatial fidelity that is superior to and more consistent than similar parameters of other MRA methods tested. Although the composite image used to create the HYPR LR image contained signal that was temporally mismatched to a given time frame, the HYPR LR weighting image successfully suppressed the erroneous signal to values comparable to the background signal. The temporal resolution of HYPR LR is limited by the number of projections needed to construct a single time frame I_t in Equation 3.1 and thus, can be characterized

by the display frame rate. Furthermore, HYPR LR exhibits little spreading of the signal to neighboring pixels, maintaining the temporal resolution of the non-HYPR-processed images.

Now, let us consider an idealization where the only contributing signal in all time frames is that of an impulse signal within an AOI in a single frame. The weighting functions for frames that do not contain the impulse are then zero everywhere. The impulse response function is then

Equation 3.10

$$IRF(t) = h \cdot \delta_{t,t_i}$$

where the only nonzero contribution is from the frame that contains the impulse signal, denoted by the Kronecker delta. The constant h<1 is a reminder that HYPR LR does not always reconstruct the impulse signal intensity fully. The temporal frequency response function is then

Equation 3.11

$$TFR(f) = 1$$

a constant value normalized to 1. The value of h is determined by many factors including, but not limited to: AOI size, undersampling factor in the weighting image and the size of the convolution kernel F. As locations outside the AOI become nonzero, we expect the impulse response function to change only minimally as long as the convolution kernel used in the weighting functions is not so large as to blur other signal producing regions into the AOI. When this occurs, signal from outside the AOI is spread into the AOI, reducing waveform fidelity. If this cross-talk does not occur, signal outside

the AOI can still influence the impulse response function by producing undersampling artifact within the AOI. We can then estimate the impulse response function to be:

Equation 3.12

$$IRF(t) = h \cdot \delta_{t,t_i} + \sum_{n=0}^{i} s_n \delta_{t,n}$$

where the constants $s_n<h$ such that i is the number of frames, represent small contributions from streak artifacts arising from signal outside the AOI. Since these contributions are typically small, we expect the temporal frequency response function to remain approximately constant. The ideal convolution kernel used in HYPR LR processing would be large enough to remove a significant amount of undersampling artifacts thereby minimizing the constant s_n. However, a compromise in filter size must be made to prevent overlap between the AOI and other signal producing regions during the convolution process. Unlike TRICKS and Keyhole, the simulation for HYPR LR exhibits no explicit AOI size dependencies. Instead, the dependency is hidden within the variable h, which is expected to decrease if the AOI becomes prohibitively small. This can be seen in Figure 3.14; impulse response deteriorates with AOI sizes of 2 x 2 pixels and smaller. However, across the majority of simulations, the impulse response and AOI spatial representation are good and more consistent for HYPR LR than the other MRA methods.

It requires mention that this simulation serves only to demonstrate the effect of an impulse signal on the different MRA techniques and to characterize the extent to which they are in fact time-resolved. In a standard clinical situation involving an MRA

examination using the Keyhole method, for example, the reference frame would be taken at the very end of the scan when only residual amounts of a contrast agent is contained within the vessels. The likelihood of capturing a large impulse signal of diagnostic value during the reference frame acquisition is small. Similarly, while impulse response is poor for TRICKS in Case B and Case C, the acquisition scheme is designed to decrease the likelihood of such a scenario occurring. Therefore, the results of this paper provide evidence that Keyhole and TRICKS do not perform well as time-resolved methods under all circumstances; though, the circumstances under which they degrade to the extent shown in this work are extreme and unlikely.

Also, this simulation does not take into account parallel imaging techniques that can be used to increase the speed of Cartesian k-space acquisitions. While the frame rate of Keyhole and TRICKS would improve with the addition of parallel imaging, the scenarios shown here are still valid since they are intrinsic to the view-sharing scheme of the reconstruction methods.

3.6 Conclusions

In this work, the temporal resolution of commercially used magnetic resonance angiography techniques were investigated and compared with the temporal resolution of HYPR LR using a numerical simulation and an analysis analogous to the use of point-spread functions and modulation-transfer functions to describe the spatial resolution of an imaging system. Both Keyhole and TRICKS temporal responses vary drastically depending on the size and timing of the impulse signal. In most cases, the temporal

resolution of the two techniques is not best described as their respective frame update rates. The exception being Case L for Keyhole; when the impulse occurred during the acquisition of low spatial frequency data, the impulse response function was near perfect, however there was severe loss of spatial resolution in the phase encode direction.

The HYPR LR method showed a more consistent impulse response. The AOI was clearly visible in the correct frame with minimal spreading of the signal in either space or time dimensions. In this study, the weighting image was reconstructed using a radially symmetric Gaussian convolution kernel that reduced the spatial resolution of the weighting image by a factor of 5. The relative success of the HYPR LR method is dependent upon many user-chosen parameters including the convolution kernel (F), and the weighting image undersampling factor. Temporal and spatial resolution could deteriorate if a large kernel is used, causing cross-talk to occur between the AOI and neighboring signal producing regions. Poor results could also be simulated if undersampling factors were too high, resulting in numerous, high intensity undersampling artifacts in the weighting image. With prudent and conservative choices for the convolution kernel and undersampling factor, HYPR LR exhibits high temporal resolution that is best described by the weighting image update rate.

Chapter 4: Use of a Computer-Controlled Motion Phantom to Investigate the Temporal and Spatial Fidelity of HYPR Processing

4.1 Introduction

Time-resolved contrast-enhanced MR Angiography (CE-MRA) remains a highly utilized clinical technique for evaluation of vascular diseases. Despite significant advantages, including providing three-dimensional information, MR based methods have been unable to provide sufficiently comparable in-plane spatial resolution and temporal resolution to x-ray digital subtraction angiography (DSA). Considerable research has been performed with the goal of improving CE-MRA through accelerated data acquisition and reconstruction methods(26,29,32,40,48,49).

Phantom experiments and *in vivo* comparisons of advanced time-resolved CE-MRA methods are necessary and instructive to validate a technique. However, in certain

phantom experiments and *in vivo*, the exact temporal dynamics of the object being imaged are unknown. Therefore, comparisons and precise judgments of the temporal and spatial fidelity of reconstruction techniques based solely on such experiments can result in a vague interpretation. Previously, an experimental set-up similar to the one used in this work was used to facilitate a thorough investigation of the temporal behavior of Cartesian view-shared time-resolved MRA techniques(50). In the work reported here, a computer-controlled motion phantom was used to translate an object through the image field-of-view (FOV) in a way that mimics contrast traveling through the vasculature of the lower extremities in order to validate the accuracy of a constrained reconstruction technique used in time-resolved CE-MRA of the peripheral vessels.

Highly constrained backPRojection (HYPR)(40) is a constrained image reconstruction technique that aims to produce time-resolved images with high spatial and temporal resolution while providing high signal-to-noise ratios (SNR). The method utilizes anatomical or structural constraints from a well-sampled, time-averaged composite image in combination with temporal information from highly undersampled weighting images to reconstruct a time series. Both the composite and temporal weighting images are required to have high SNR. Since the composite image is formed using a large amount of data collected over a long temporal duration, high SNR occurs naturally. This is not the case for the temporal weighting image, which is highly undersampled; additional steps are taken to ensure sufficient SNR. These steps vary depending on the specific HYPR algorithm being utilized, but typically spatial filtering is performed to increase the SNR of the weighting image.

When the HYPR algorithm is used, it is assumed that sufficient levels of signal sparsity and spatio-temporal correlation are present in the data and the method has typically shown the best performance in these settings. Therefore, time-resolved CE-MRA is likely to be well-suited for the technique. Several authors have shown that when applied to CE-MRA, reconstructions based on the HYPR concept exhibit a decrease in undersampling artifacts and an increase in SNR compared to corresponding, non-HYPR-processed undersampled images(41-43,51-54).

The spatial and temporal fidelity of images produced with HYPR-based algorithms has been evaluated using both numerical simulations(41,42,51-53) and phantom experiments(54,55) as well as *in vivo* experiments(41-43,55). As a result of these works, the spatial resolution of HYPR images has been theorized to be equal to the composite image spatial resolution, regardless of the amount of spatial filtering applied to the weighting image. The temporal resolution of HYPR images has been theorized to be equal to the weighting image temporal resolution, regardless of the amount of temporal averaging represented in the composite image. In HYPR images, spatial and temporal domains have a complicated relationship due to the multiplication of the low spatial resolution, high temporal resolution weighting image with the high spatial resolution, low temporal resolution composite image. Therefore, measurements of pure spatial resolution or temporal resolution are difficult and potentially misleading. However, certain measurements and observations can be made of characteristics that are indicative of

images with high spatial and temporal resolution. The terms *spatial fidelity* and *temporal fidelity* refer to such measurements and observations and will be discussed below.

In this chapter, the spatial and temporal fidelity of HYPR processed images is investigated using a computer-controlled phantom experiment designed to model the spatio-temporal characteristics of peripheral MRA. The phantom and the acquisition and reconstruction methods were designed based on our *in vivo* research studies(56-59). The goal of this experimental set-up was to provide not only well-defined temporal dynamics and spatial characteristics of the motion phantom, but also circumstances that imitate *in vivo* scenarios.

4.2 Methods

4.2.1 Experimental Set-Up

A custom built computer-controlled motion stage (Hardware: Velmex linear stage, Parker Hannifin controller, drive and motor. Software: Motion Planner, Parker Hannifin) was used to translate an object through the imaging FOV during data acquisition in order to mimic a bolus of contrast material traveling through vasculature. As shown in Figure 4.1, this dynamic object was composed of a single, dilute-gadolinium-filled tube with two distinct, concentric sections: an artery component (6.35 mm inner diameter), which was chosen to represent the initial passage of a contrast bolus through an artery of interest, and a wider section (15.8 mm inner diameter) that was chosen to represent a combination of the artery in addition to veins running parallel to and on opposite sides of the artery.

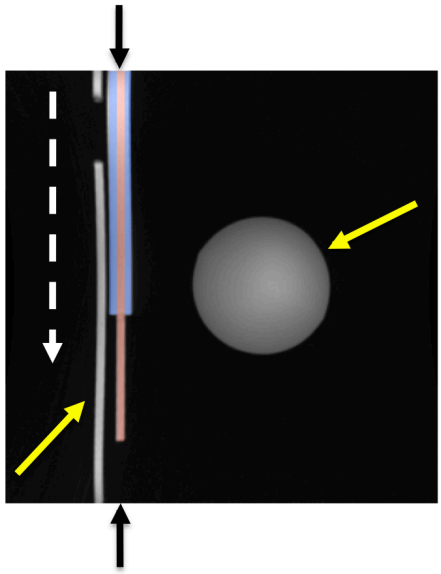

Figure 4.1: Coronal MIP of imaging FOV. This image was acquired while the dynamic object (between black arrows) was held stationary at the point of maximum displacement. Solid yellow arrows indicate stationary objects. The dashed white arrow indicates the direction of motion of the dynamic object. The dynamic object is shaded red and blue to point out the artery and vein components, respectively. The different colors should not be interpreted as representing a physical barrier defining the artery and vein; the entire dynamic object is confluent.

In this design, the artery and vein components are confluent – there is no distance separating the two sections. While this represents an unlikely *in vivo* scenario, it provides a useful test to illustrate the characteristics of the reconstruction technique when arteries and veins with minimal wall thicknesses are touching, corresponding to relatively low sparsity and spatio-temporal correlation – the most challenging scenario for the HYPR reconstruction process. Figure 4.1 shows a coronal maximum intensity projection (MIP) of the imaging FOV (32 cm) while the dynamic object is stationary at its point of maximum displacement – i.e. with no motion present. The spherical and long cylindrical phantoms highlighted with solid yellow arrows are stationary aspects of the

phantom set-up (the signal void in the long cylindrical phantom is an air bubble that will not affect the outcome of the experiment). The dynamic object (between the black arrows) is shaded red and blue to indicate the artery and vein components, respectively. The computer-controlled motion stage and sharp edges of the phantom were chosen to provide well-defined inputs to properly characterize the behavior of the reconstruction technique.

The motion stage was programmed to have a maximum displacement of 24.0 cm. Data acquisitions were performed during phantom translation with velocities of 5.0 and 10.0 mm/s. These velocities were chosen to allow for an accurate characterization of the temporal fidelity of HYPR processing. The motion stage was programmed to traverse 1.0 cm after pre-scanning was complete and prior to triggering the scanner to begin data acquisition. This was to ensure that the motion stage had completely ramped up to its programmed velocity so that the velocity during data acquisition was constant. Also, for each acquisition, the total time allowed for playing of discarded acquisitions was held constant, ensuring that the motion stage was in the same position for the start of data acquisition for all experiments for a given programmed velocity.

4.2.2 Data Acquisition

Data were acquired on a 3.0T scanner (Discovery MR750, GE Healthcare) using a 32-channel phased array torso coil (GE Healthcare). The 3D radial vastly undersampled projection reconstruction (VIPR)(39) method was used for data acquisition. The acquisition parameters were chosen to mimic the parameters used in our *in vivo*

research studies for obtaining data for HYPR-processed images of the peripheral vasculature and included: image FOV: 32.0 x 32.0 x 32.0 cm; imaging matrix: 320 x 320 x 320; 1.0 mm isotropic spatial resolution; fractional echo 80% with 256 acquired points per radial projection; TE/TR: 1.1/4.1ms; flip angle: 20°; receiver BW: ±125kHz; radial projections per frame: 640; undersampling factor (compared to fully sampled Cartesian matrix of the same size): 250; total scan time: 50 seconds. Individual time frames were acquired in 2.59 seconds/frame representing the time to collect a single undersampled subset of angular projections spanning all of k-space.

4.2.3 Data Reconstruction

Data from the VIPR acquisition were reconstructed into two distinct image series, which were analyzed independently. Images from these series are referred to as: Time-Frame and HYPR. The Time-Frame images for a given exam were reconstructed from undersampled time frame data (k_t) using a gridding algorithm(35) (including weighting terms to compensate for sampling density) and a 3D Fourier transform. No extraneous processing (i.e. view-sharing or HYPR) was applied to the data during reconstruction. In other words, there is no source of temporal inaccuracy in the reconstruction of any image in the Time-Frame series beyond the motion of the object itself during the acquisition of that time frame.

HYPR time frames were processed using the HYPR LR algorithm(46). The generalized HYPR LR image reconstruction formula can be expressed as:

Equation 4.13

$$I_H(t) = I_C \cdot I_W(t) = I_C \cdot \frac{\Phi(k_t)}{\Phi(k_t^C)}$$

where I_C is a well-sampled composite image with high SNR, high spatial resolution, and limited or no temporal information; $I_W(t)$ is the unique weighting image for time frame t (note that both the HYPR weighting image and Time-Frame image for a given time frame originate from the same k-space dataset, (k_t)); Φ represents a weighting image reconstruction technique for k-space data (k_t) that reduces aliasing artifacts and improves SNR relative to the corresponding Time-Frame image. This reconstruction technique (Φ) may vary for different data acquisition trajectories. For the VIPR acquisition described above, Φ represents a low-spatial-resolution reconstruction of the given k-space data. SNR improvement (and subsequent spatial resolution loss) was achieved by not applying sampling density compensation terms to spatial frequencies outside the Nyquist radius, computed based on the level of undersampling in the time frame.

Figure 4.2 shows the magnitude of a one-dimensional profile through the isotropic, three-dimensional point-spread-functions (PSFs) corresponding to the reconstruction techniques used for Time-Frame images (gridding with full density compensation and 3D Fourier transform) and HYPR weighting images (gridding with some density compensation and 3D Fourier transform). Full width at half maximum and full width at tenth maximum (FWHM/FWTM) values for the Time-Frame image and HYPR weighting image PSFs are: 1.0/1.8 pixels and 2.84/5.87 pixels, respectively (estimated using linear interpolation to find locations of half and tenth maximum).

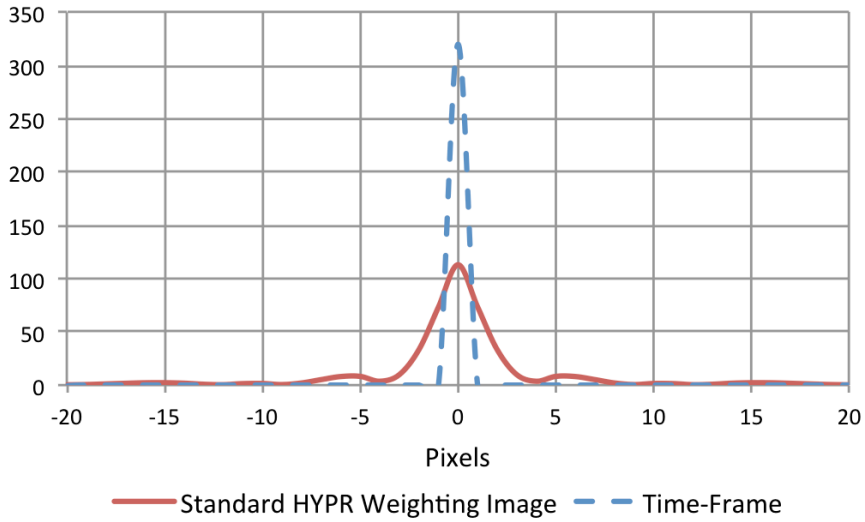

Figure 4.2: Point-spread-functions corresponding to the reconstruction techniques used for Time-Frame and standard HYPR weighting images. FWHM/FWTM values for standard HYPR weighting image and Time-Frame image: 2.84/5.87 pixels and 1.0/1.8 pixels, respectively (estimated using linear interpolation).

To study the effect that the weighting image reconstruction technique has on the resulting HYPR image, two other weighting image reconstruction techniques were investigated: ΦH.Res and ΦL.Res. The former results in less dampening of high spatial frequency information and a weighting image with higher spatial resolution, but lower SNR than the standard HYPR weighting image described above. The latter dampens signal from more high spatial frequencies and results in a lower spatial resolution weighting image with higher SNR than the standard HYPR weighting image. FWHM/FWTM values for ΦH.Res and ΦL.Res point-spread-functions are: 1.16/2.91 and 4.08/9.12 pixels, respectively.

Unless specifically noted, the HYPR weighting image reconstruction technique (Φ) analyzed in Figure 4.2 is the technique used in this work and the composite image is reconstructed using a time average of all the acquired data (acquired during 50 seconds), unless otherwise noted. The well-sampled composite image is formed using 20,480 radial projections (undersampling factor of 7.5) and the same density compensation technique that is used for the Time-Frame images. These are the strategies typically used for our *in vivo* research studies(56-59).

4.2.4 Data Analysis

Spatial Fidelity

The HYPR process as described above involves the multiplication of two images with different spatial resolutions. The resulting HYPR image spatial resolution has been reported theoretically as being equal to that of the HYPR composite image regardless of the spatial resolution of the weighting image after the reconstruction technique (Φ, Φ:H. Res or Φ:L.Res) is applied. In this study, the accuracy of this assumption is investigated by measuring signal profiles in the final HYPR images through the artery component in the direction orthogonal to motion.

Profiles from HYPR images were compared with profiles from corresponding images of interest: Time-Frame and HYPR composite images. Profiles were obtained by averaging the signal intensity along six neighboring line profiles placed in a single, central coronal

slice. Averaging across coronal slices was not feasible since the tube width varied in the anterior/posterior direction due to the curvature of the tube.

It is important to note that there are two distinct scenarios that require separate consideration since the profiles measured from a HYPR image may vary depending on the structures present in each HYPR component image (weighting and composite). First, a profile was taken at a point (in frame 13 of the series) where the artery component was the only structure enhanced in both the weighting image and the composite image. This profile is referred to as $P_{A,A}$, standing for Artery (in the weighting image), Artery (in the composite image). This is anticipated to represent the best-case scenario for the HYPR technique. Second, a profile $P_{A,AV}$, standing for Artery (in the weighting image), Artery + Vein (in the composite image) was taken (in frame 4 of the series) at a point along the dynamic object where only the artery component was enhanced in the weighting image, but the artery and vein components were enhanced in the composite image. This is expected to represent a challenging scenario for HYPR – especially since the artery and vein components are confluent in this experimental set-up, as noted above.

Temporal Fidelity

A clinical benefit provided by a temporally-resolved sequence is its ability to demonstrate, in each time frame, a temporally-finite amount of information from a temporally-changing object. The temporal resolution of a series of HYPR images has often been theoretically reported as the temporal resolution of the corresponding Time-Frame image. This is done even though information acquired outside the given temporal

resolution window is included in the HYPR composite image and therefore used in the HYPR image reconstruction process. In this study, the accuracy of this assumption is investigated by i) plotting profiles from Time-Frame and HYPR images of the leading edge of the dynamic component of the phantom; ii) measuring the location of the leading edge of the dynamic component of the phantom as a function of time in both Time-Frame and HYPR image series; and iii) plotting the different enhancement patterns of the artery and vein components in both Time-Frame and HYPR image series.

Due to the continuous motion of the phantom during data acquisition and the inherent time averaging of low spatial frequency data collected within a given time frame with the VIPR acquisition, a certain amount of edge blur in the direction of motion is expected. Therefore, the leading edge is defined as the time averaged position of the most distal edge of the artery component during the interval of data acquisition for a given time frame. In this work it is assumed that all additional blurring of the leading edge is due to losses in temporal fidelity imposed by the image reconstruction technique.

To investigate and assess the temporal fidelity associated with HYPR processing, a profile through the dynamic object in the direction of motion was measured by averaging profiles from three neighboring lines placed in a central coronal slice of the 3D image. Profiles were considered for comparison only if the leading edge was in the central 50% of the image FOV. This restriction was imposed to minimize the effects of receiver coil sensitivity and possible errors in the gradient non-linearity correction, which are worse with increasing distance from isocenter. Along a profile, the absolute location of the

phantom edge was defined as the spatial location where the signal was equal to 50% of the difference in mean signals within and outside of the artery component.

Additionally, the ability of HYPR processing to accurately maintain and represent different temporal patterns within the same time series was examined. Three-dimensional ROIs of size (4 x 3 x 5 pixels) were placed in the path of the artery and vein components of the dynamic object in Time-Frame and HYPR time series. Mean signals within these ROIs were measured in consecutive time frames.

As noted above, the composite image in HYPR processing is generated using data extending beyond the specific time frame of interest. To investigate how this affects the ability to discern temporal changes in a HYPR image, an analysis was performed by reconstructing HYPR time series using a sliding window composite of shorter temporal length.

4.3 Results

4.3.1 Spatial Fidelity

Figure 4.3 shows $P_{A,A}$ and $P_{A,AV}$ profiles for Time-Frame and HYPR series and for the HYPR composite image. Single slices of Time-Frame, HYPR and HYPR composite images are also shown. The red horizontal lines on the images illustrate the measurement locations of the two profiles taken along the dynamic object. Note that in both frames (Figures 4.3a and 4.3b), the SNR of the HYPR image is significantly higher

than the SNR of the Time-Frame image, though there is almost no evidence of spatial fidelity loss in the HYPR images or profiles.

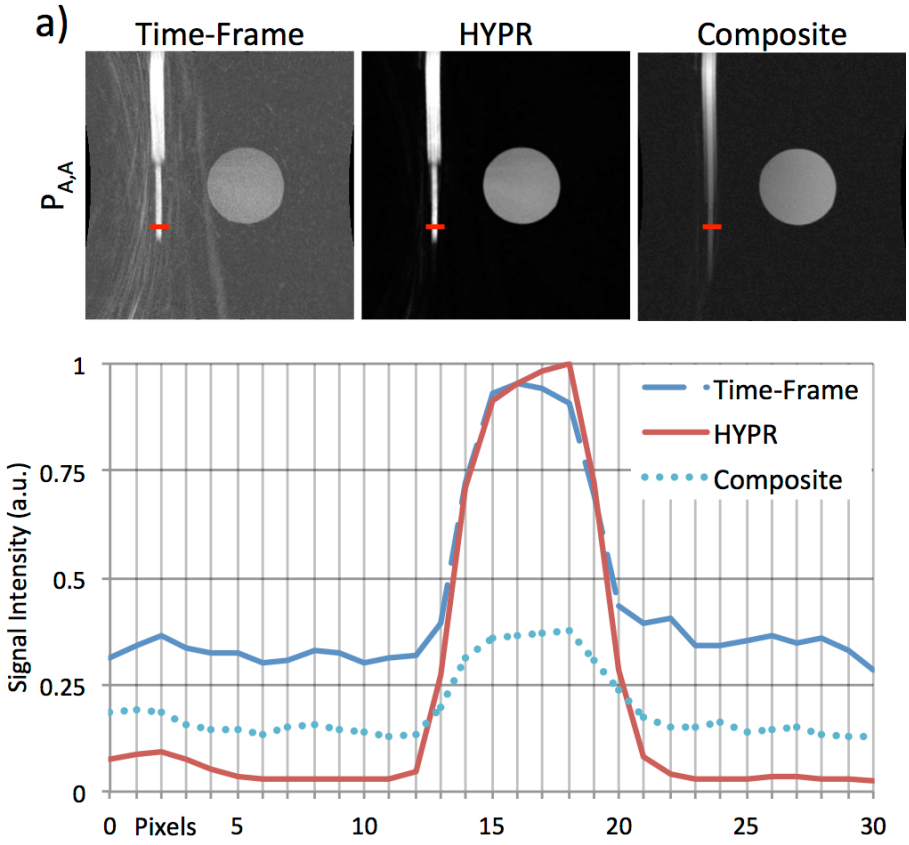

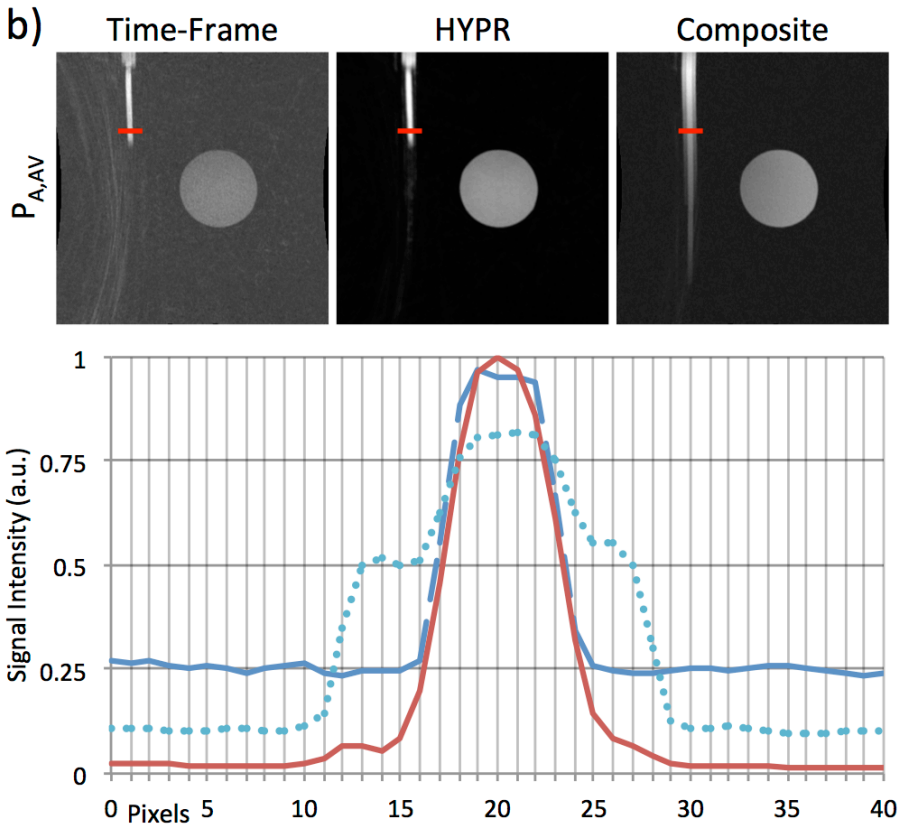

Figure 4.3: The spatial locations of $P_{A,A}$ (a) and $P_{A,AV}$ (b) are shown in the Time-Frame, HYPR and HYPR composite single slice images. Note that in (a), the artery component is the only structure present in both the Time-Frame and HYPR composite images, while in (b) both the artery and vein components are enhanced in the HYPR composite image. $P_{A,A}$ (a) and $P_{A,AV}$ (b) profiles are plotted. The legend in (a) is valid for (b).

Figures 4.4a and 4.4b show $P_{A,A}$ and $P_{A,AV}$ profiles for Time-Frame, standard HYPR, HYPR:ΦH.Res and HYPR:ΦL.Res series. Single slice images from the corresponding time frames are also shown. Figures 4.4c and 4.4d show MIP images that have been cropped and enlarged to show the section of the artery component from which $P_{A,A}$ and $P_{A,AV}$ profiles were measured.

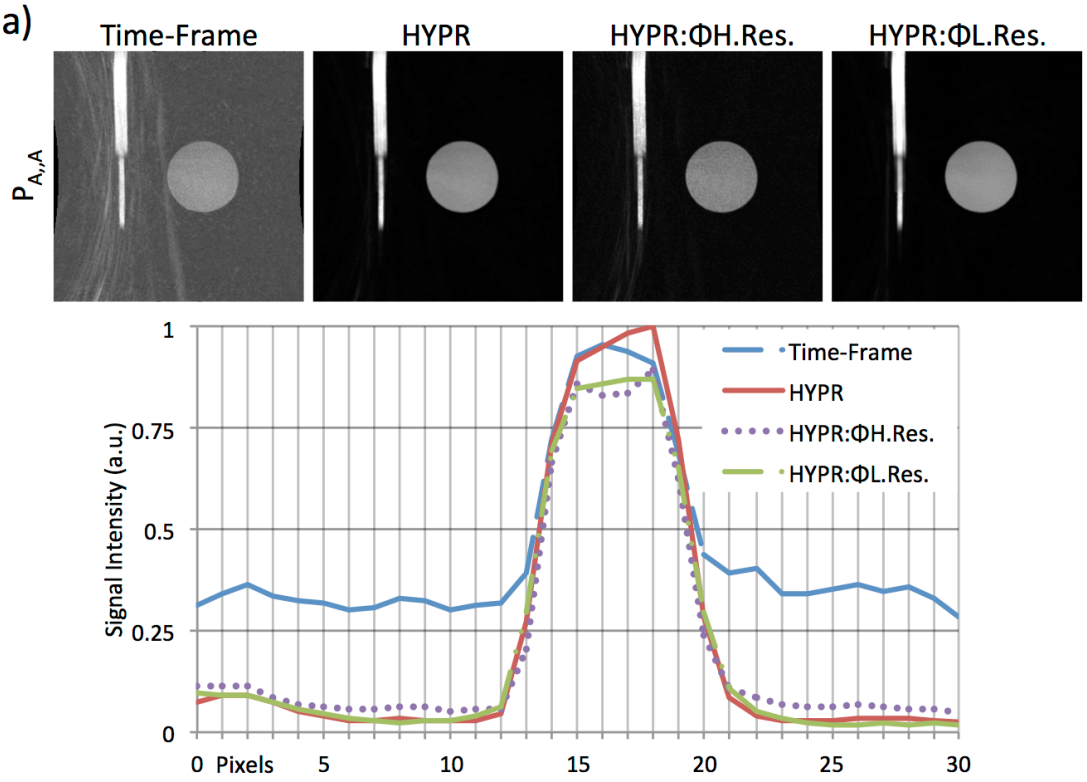
a)
Time-Frame
HYPR
HYPR:ΦH.Res.
HYPR:ΦL.Res.
P_A,,A
Signal Intensity (a.u.)
1
0.75
0.5
0.25
0
0 Pixels
5
10
15
20
25
30
Time-Frame
HYPR
HYPR:ΦH.Res.
HYPR:ΦL.Res.

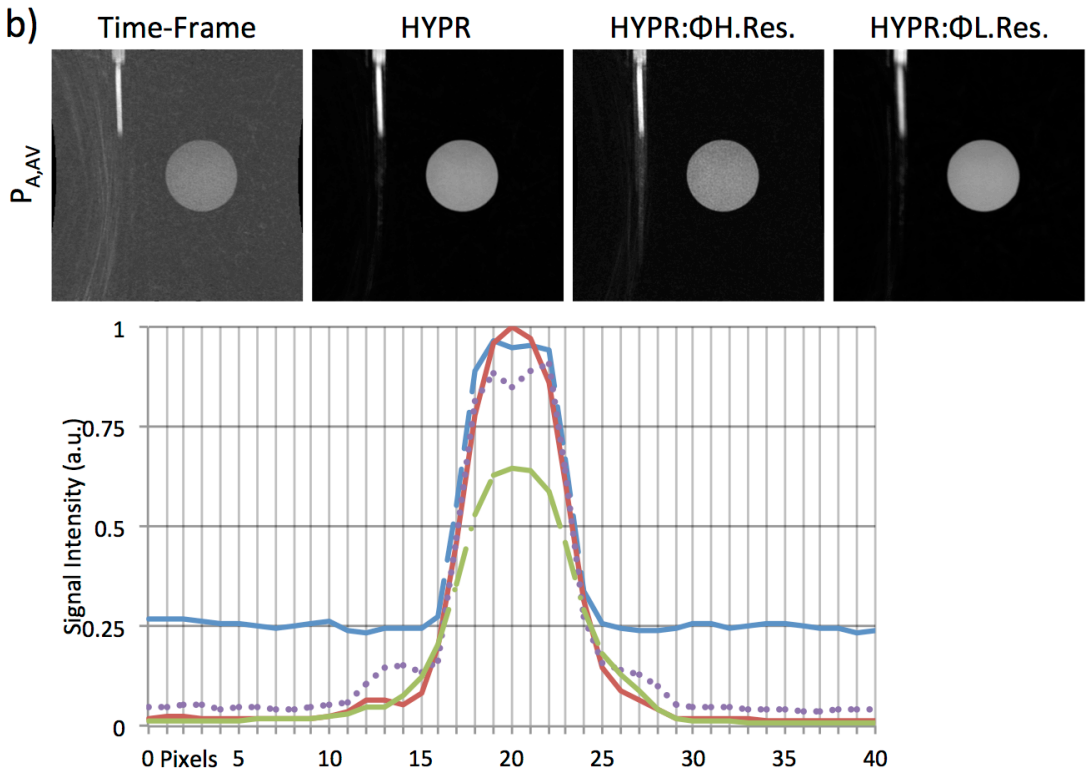
b)
Time-Frame
HYPR
HYPR:ΦH.Res.
HYPR:ΦL.Res.
P_A,AV
Signal Intensity (a.u.)
1
0.75
0.5
0.25
0
0 Pixels
5
10
15
20
25
30
35
40

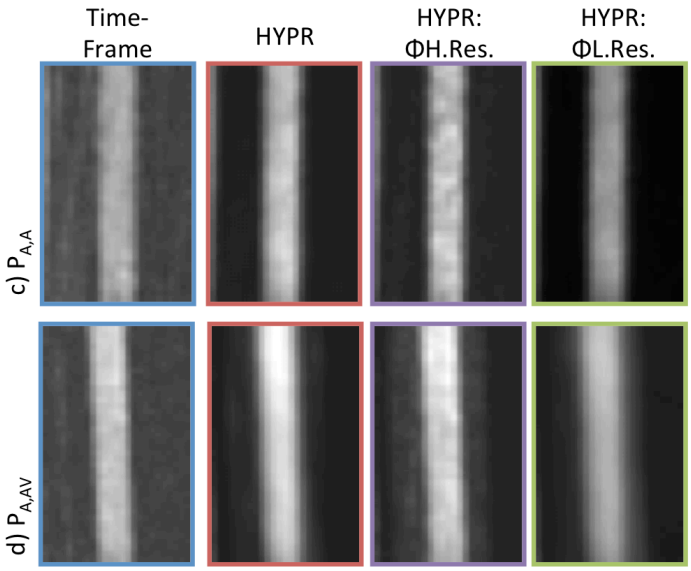

Figure 4.4: $P_{A,A}$ (a) and $P_{A,AV}$ (b) profiles from a Time-Frame image and from a standard HYPR image (reconstructed with the standard weighting image), as well as from HYPR images reconstructed with higher spatial resolution weighting images (HYPR:ΦH.Res) and lower spatial resolution weighting images (HYPR:ΦL.Res). The legend from (a) applies to (b). (c-d) MIPs of Time-Frame (TF), standard HYPR, HYPR:ΦH.Res and HYPR:ΦL.Res images cropped and enlarged to show the region from which $P_{A,A}$ (c) and $P_{A,AV}$ (d) profiles were measured.

To quantify the spatial fidelity of each analyzed image, FWHM and FWTM values of the $P_{A,A}$ and $P_{A,AV}$ profiles for each reconstruction technique were calculated and are reported as mean ± standard deviation in Table 4.1. FWHM and FWTM values were calculated for each of the six neighboring line profiles by linearly interpolating between locations along the profile with values closest to half and tenth the maximum profile value, respectively. FWTM values were unattainable for Time-Frame profiles, since profile values never decreased to one tenth of the maximum signal intensity. Note that these FWHM/FWTM values cannot be directly compared to values from Figure 4.2, which measure the FWHM/FWTM of point-spread-functions.

$P_{A,A}$

	Truth	Time-Frame	HYPR	HYPR: ΦH.Res.	HYPR: ΦL.Res.
FWHM	4.18 ± 0.02	6.56 ± 0.15	5.99 ± 0.07	5.89 ± 0.12	6.24 ± 0.05
FWTM	7.25 ± 0.05	--	8.67 ± 0.10	9.46 ± 0.58	9.20 ± 0.18

$P_{A,AV}$

	Truth	Time-Frame	HYPR	HYPR: ΦH.Res.	HYPR: ΦL.Res.
FWHM	4.18 ± 0.02	6.80 ± 0.07	6.25 ± 0.01	6.56 ± 0.05	10.0 ± 0.03
FWTM	7.25 ± 0.05	--	10.60 ± 0.05	16.48 ± 0.40	14.08 ± 0.20

Table 4.1: Full width at half maximum (FWHM) and full width at tenth maximum (FWTM) values of $P_{A,A}$ and $P_{A,AV}$ profiles for Time-Frame, standard HYPR and HYPR images reconstructed with alternative weighting image reconstruction techniques (HYPR:ΦH.Res and HYPR:ΦL.Res). Truth was obtained by measuring FWHM/FWTM values on a fully-sampled image acquired when the phantom was stationary, which characterizes the best possible representation of the width of the artery component.

4.3.2 Temporal Fidelity

Figure 4.5 shows leading edge plots of Time-Frame, HYPR and HYPR composite images for two consecutive time frames. The shaded grey box represents the calculated data acquisition window (CDW), defined as the distance the phantom moved during the data acquisition of a given time frame; phantom edge blur is expected and acceptable within the calculated data acquisition window due to motion during the acquisition. To the right of each plot are cropped and enlarged MIP images associated with each of the two time frames.

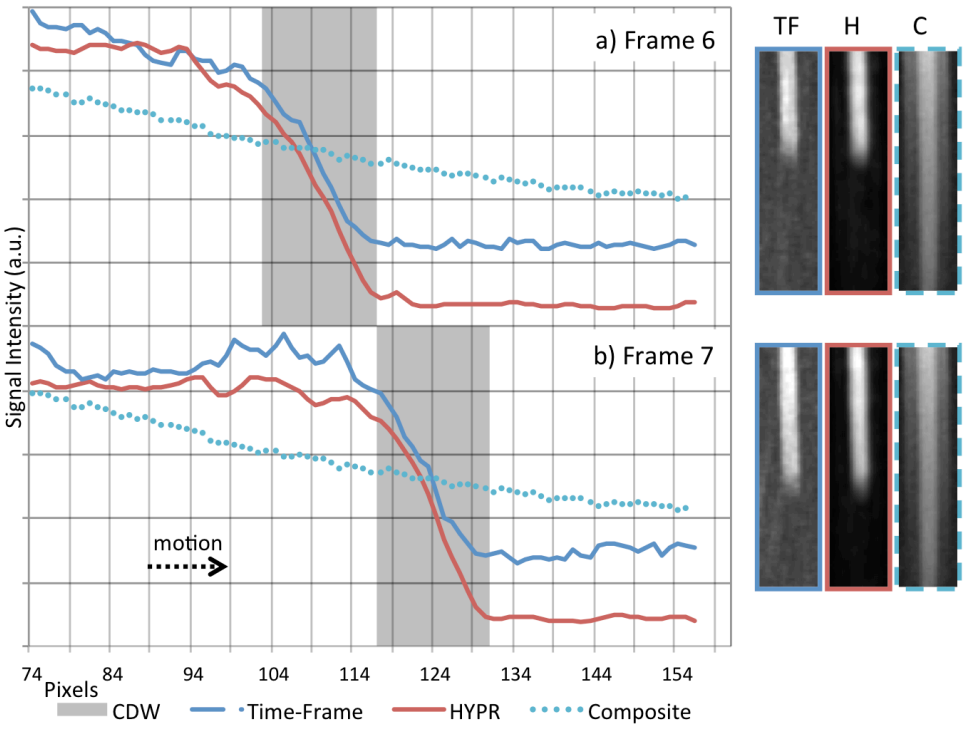

Figure 4.5: Plots of the leading edge from two consecutive HYPR (H) and Time-Frame (TF) frames are shown with a corresponding plot from the composite (C) image. The grey box indicates the Calculated Data acquisition Window (CDW) – or the known positions of the phantom edge during data acquisition for the given time frame.

Figure 4.6 shows absolute locations of the phantom edge as measured from consecutive frames in the HYPR time series plotted as a function of time for programmed phantom velocities of 5.0 and 10.0 mm/s. In both studies, phantom velocity (represented by the trend-line slope) corresponds well with the velocities programmed into the motion phantom. Further, it is highly linear; R^2 values (0.9991 for 10.0 mm/s velocity and 0.9997 for 5.0 mm/s velocity) suggest that HYPR reconstruction accurately depicted the constant velocity programmed for the motion stage.

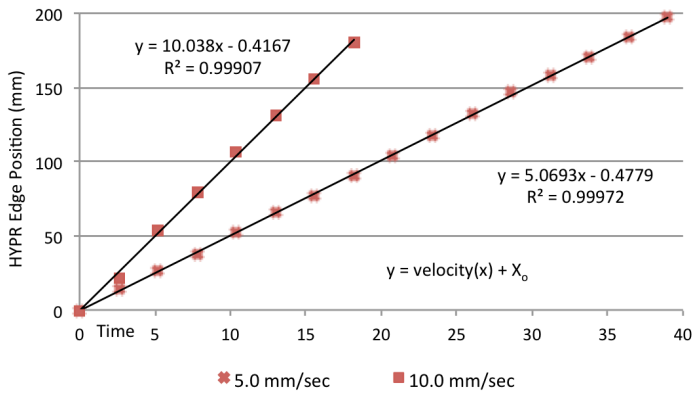

Figure 4.6: Phantom leading edge locations measured in consecutive time frames from HYPR image series acquired with different phantom velocities.

Figure 4.7 shows mean artery and vein component ROI signals from consecutive frames measured from Time-Frame and HYPR time series.

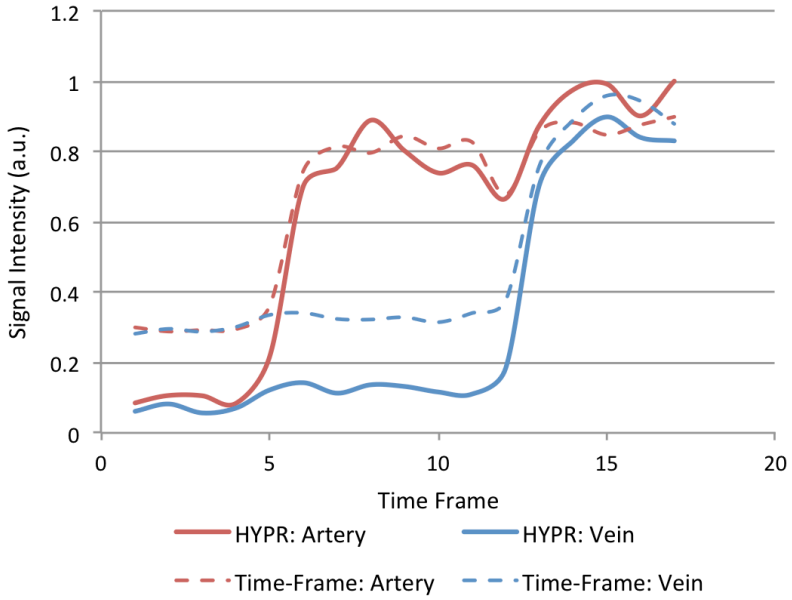

Figure 4.7: Mean artery and vein component ROI signals from consecutive frames of Time-Frame and HYPR time series. The signals measured in the HYPR series for arterial and venous components remain consistent with those measured in the Time-Frame series.

Figure 4.8 shows comparisons of leading edge blur in HYPR images reconstructed with composite image temporal lengths of 50 and 21 seconds (full and sliding window composites, respectively); two consecutive time frames for each technique are shown. The times reported in each legend entry in Figure 4.8 represent the longest temporal duration used in the given reconstruction process for each entry. HYPR: 50 sec is the HYPR image, reconstructed using a 50 second, full composite. Composite: 50 sec is the composite image used in HYPR: 50 sec. Note that the profile for Composite: 50 sec shows no temporal change (it is identical for both time frames); this is because it refers to a composite image containing all the temporal data in the series (i.e. full composite). Composite: 21 sec corresponds to the composite image used in HYPR: 21 sec and is a sliding window composite image.

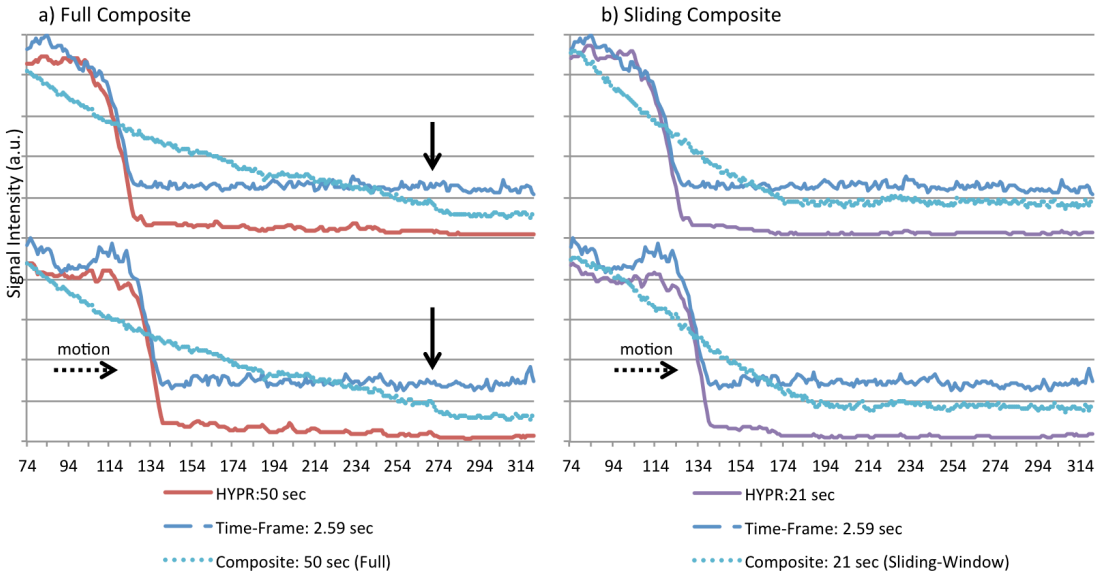

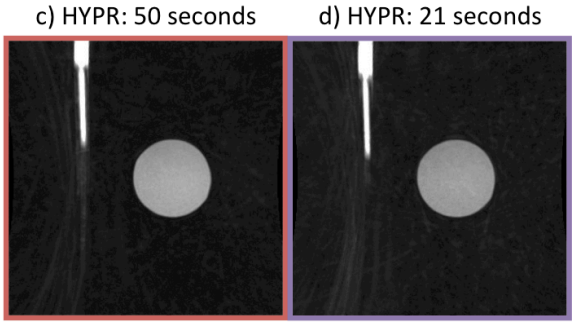

Figure 4.8: Leading edge profiles measured in the direction of motion from HYPR images reconstructed with composite image temporal lengths of 50 and 21 seconds. The times reported in the legend entry represent the longest temporal duration used in the given reconstruction process for each entry. Composite: 50 sec corresponds to a full composite, while Composite: 21 sec corresponds to a sliding window composite. Un-cropped, single slice images from HYPR datasets reconstructed using a full composite (c) and a sliding window composite (d) are shown. Note the increased amount of undersampling artifacts present in (d).

4.3.3 In vivo

Figure 4.9 shows images acquired from a patient with peripheral artery disease. Coronal MIP images of an arterial time frame are shown for Time-Frame and HYPR reconstructions. The HYPR composite image is also shown. In Figure 4.9d, profiles orthogonal to the vasculature obtained from a single coronal slice exhibiting an artery flanked by veins to the right and left are shown. Only the artery is enhanced in the time frame shown, whereas both artery and vein are enhanced in the composite image (an arrangement analogous to that of the $P_{A,AV}$ profile in the phantom scan).

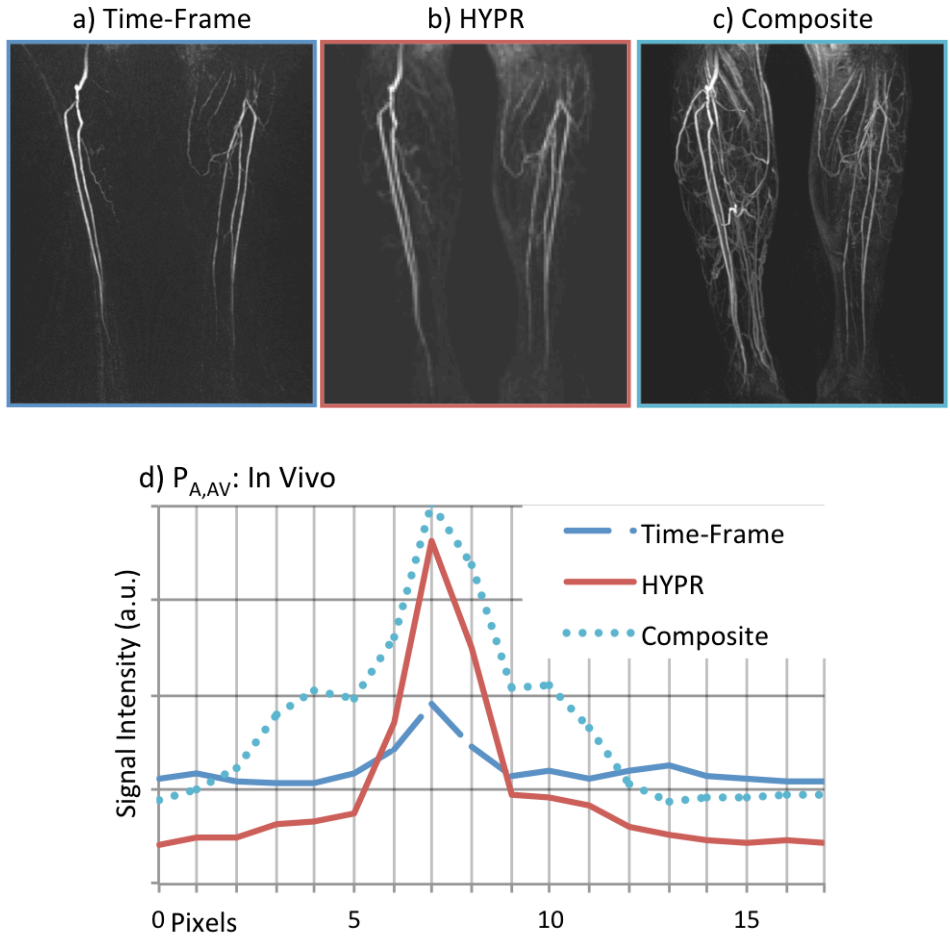

Figure 4.9: Coronal MIP images of Time-frame, HYPR and HYPR composite datasets from a patient with peripheral arterial disease (a-c) and profiles (d) orthogonal to the vasculature obtained from a single coronal slice exhibiting an artery flanked by veins to the right and left are shown. Only the artery is enhanced in the time frame shown, whereas both artery and vein are enhanced in the composite image (an arrangement analogous to that of $P_{A,AV}$ in the phantom scan).

4.4 Discussion

4.4.1 Spatial Fidelity

Figure 4.3a shows that, in the ideal case of similar structures represented in both the weighting and composite images, HYPR processing – and specifically a well-chosen

weighting image reconstruction technique, Φ – does not result in a loss of spatial fidelity. FWHM and FWTM values for $P_{A,A}$ in Table 4.1 support this assessment. In this case, and with these reconstruction parameters, the use of a low spatial resolution HYPR weighting image does not result in a HYPR image with decreased spatial fidelity. In this case, despite the weighting image being blurred, there are no venous components (or any other structures) near the arteries in the weighting image, so nothing (except noise) can be inadvertently weighted to cause misrepresentation of the arterial structures in the final HYPR image. The noise in the composite images used in HYPR processing is intentionally kept low.

Of more interest are the $P_{A,AV}$ results shown in Figure 4.3b where the artery and vein components are enhanced in the composite image and the vein component requires adequate suppression by the weighting image in order to accurately reflect the state of the phantom in the given time frame. At high signal values (i.e. above the background signal intensity of the Time-Frame profile), the profiles of the Time-Frame and HYPR images are comparable. The FWHM values reported in Table 4.1 for these images support this observation. However, FWTM values for HYPR $P_{A,AV}$ profiles reflect an incorrectly wide profile. Examination of the plot in Figure 4.3b shows this loss of spatial fidelity is due to the composite image signal (from the venous component) not being fully suppressed. This is due to non-zero values in the weighting image at those locations.

Non-zero values in inappropriate locations in the HYPR image can be due either to i) the intentional blurring of the weighting image, which has a local impact on structures in the

composite image that are close to the arterial component or ii) non-zero noise in the weighting image, which has a global impact on all structures in the composite image. In either case, the result is that a very low signal intensity imprint of the composite profile still remains in the HYPR profile. This phenomenon is not indicative of a loss of spatial resolution but rather is caused by inaccurate temporal weighting of the content in the composite image. This is a potential artifact due to HYPR processing. Note however, that the artifactual signal is of extremely low intensity.

In the case where a vein is touching an artery (as in the experimental set-up), the inappropriate weighting of the vein may make the artery appear blurred, as is manifest by the widening of the FWTM in this example. However, the FWHM is unaffected by this phenomenon. Also, if there were any gap between the artery and vein, the profile would decrease at the edge of the artery, and the inappropriate weighting of the vein would cause a side-lobe in the profile, which would not manifest as blur to the artery in the HYPR image.

For HYPR:ΦH.Res, the $P_{A,A}$ profile (Figure 4.4a) and FWHM value (Table 4.1) shows high spatial fidelity. However, there is a deficiency observed in the $P_{A,AV}$ profile (Figure 4.4b) at low signal intensities that is confirmed in the measurement of FWTM. This deficiency is due to inadequate SNR in the weighting image. This occurs because HYPR:ΦH.Res images are reconstructed with a weighting image of higher spatial resolution, but lower SNR than the standard HYPR weighting image. The deficiency of the HYPR:ΦH.Res reconstruction is a result of increased background signal (noise and

streak artifacts) in the entire weighting image causing inappropriate structures in the composite image to be weighted by non-zero values. In other words, signal from the vein component in the composite image is not adequately suppressed due to the higher noise floor in the weighting image. The resulting artifact manifests as a global, low signal imprint of the composite image in the final HYPR image.

For HYPR:ΦL.Res, $P_{A,A}$ profiles (Figure 4.4a) and FWHM and FWTM values (Table 4.1) also demonstrate high spatial fidelity. However, there is a deficiency in the $P_{A,AV}$ profile (Figure 4.4b) and corresponding $P_{A,AV}$ FWHM and FWTM values. In this case, the deficiency is not a result of inadequate weighting image SNR – SNR of the HYPR:ΦL.Res weighting image is higher than that of the standard HYPR weighting image – but rather inadequate high spatial frequency information in the weighting image. The PSF of ΦL.Res is broad and creates a weighting image that is very blurred. Upon multiplication with the composite image, this blurred weighting image inappropriately weights the vein component in close proximity to the artery component. This deficiency is distinct from the composite image imprint artifact seen in HYPR:ΦH.Res as it is not global, and negatively impacts both the FWHM and FWTM values when other structures are nearby.

4.4.2 Temporal Fidelity

Figure 4.4 shows that HYPR images exhibit very high temporal fidelity. In each plot it is apparent that high signal intensity from the composite image is being sufficiently suppressed by the HYPR weighting image in each time frame. There is no significant

increase in temporal blur after HYPR processing; leading edge blur in images from both Time-Frame and HYPR reconstructions remains within the calculated data acquisition window. The benefits of HYPR processing can be appreciated by observing the images shown in Figure 4.4; the HYPR image exhibits a significant decrease in undersampling artifacts and background noise (due to the contribution from the composite image), while maintaining temporal information similar to that represented in the Time-Frame image (despite the contribution from the composite image).

The measured leading edge locations plotted for consecutive HYPR time frames in Figure 4.5 accurately depict the linear velocity programmed for the two separate experiments with velocities of 5.0 mm/s and 10 mm/s. Note that the velocities measured from the HYPR time frames are represented by the slope of the trend lines. The high degree of linearity might not be attainable in techniques that rely on view-sharing, since the center of k-space could be shared from either previous or future time frames, resulting in a non-linear relationship between edge locations measured in consecutive time frames.

Figure 4.6 shows that different temporal patterns within the time series are well maintained and represented after HYPR processing. The signal enhancement curves measured from ROIs in both artery and vein components remain consistent between Time-Frame and HYPR series. In other words, HYPR processing does not result in significant early venous enhancement.

Figure 4.7 illustrates how composite images formed using data acquired over long collection intervals affect the temporal fidelity of the resulting HYPR image. Figure 4.7a demonstrates the low signal imprint artifact mentioned above: signal from structures in the composite image appear as low intensity signal in the final HYPR image. The vertical black arrow in Figure 4.7a points to the location where the artery component terminates in the composite image (end of the phantom trajectory). In the profile from the HYPR image, a low signal intensity can be seen that extends from the leading edge of the phantom in each time frame to the end of the phantom trajectory in the composite image (the vertical black arrow), demonstrating the imprint artifact.

Figure 4.7b demonstrates that – if necessary – this imprint phenomenon can be mitigated with the use of a sliding window composite image of shorter temporal duration. The artifact is still present, but extends over a shorter distance due to decreased amount of data used to form the composite (shorter acquisition length). The vertical black arrow is not shown in Figure 4.7b, but the imprint can be seen to disappear at about 174 mm (horizontal axis) for the frame shown on the lower section of the plot. The imprint artifact and the mitigation thereof can be seen in the images shown in Figures 4.7c and 4.7d, respectively (which have been windowed and leveled in a dramatic fashion in order to show the artifact). However, Figures 4.7c and 4.7d demonstrate the penalty for implementing HYPR reconstruction with a more undersampled composite image: undersampling artifacts are more pronounced in the HYPR result when a sliding composite is used. Iterative HYPR methods(51,60,61) have been shown to mitigate the imprint artifact while avoiding the penalty associated with using an undersampled

composite image. However, it should be noted that the signal intensity of this imprint is very low and is not discernible in *in vivo* images.

4.4.3 In vivo

As noted above, since the exact temporal kinetics of a contrast-enhanced bolus are not known, conclusions regarding the exact position of the contrast bolus are difficult to support with *in vivo* data. However, the plot in Figure 4.8d confirms the results of the motion phantom experiment for analysis of the spatial fidelity of HYPR images and possible unintentional enhancement of nearby vessels due to the spatial blur in the weighting image. Given an appropriate weighting image reconstruction technique, enhanced structures in the composite image that are not enhanced in the weighting image can be adequately suppressed in the HYPR images in *in vivo* studies.

4.4.4 Study Limitations

As noted above, this study was designed to mimic a contrast bolus traversing peripheral vasculature, however there are some limitations to the study. First, although the arterial and venous signals of the phantom were confluent, the filling pattern occurred in a parallel direction. Filling of peripheral vasculature *in vivo* is anti-parallel. For the purposes of this study the filling direction of venous signal relative to arterial signal was assumed to have no effect on the study outcome.

Second, the sharp edges of the phantom over-express high spatial frequencies and result in streak artifacts of higher intensity than typically found *in vivo* with projection reconstruction. This was an intentional design choice of the motion phantom to provide well-defined sharp edges to improve measurements of temporal and spatial fidelity.

Third, the motion phantom velocities used in this experiment were significantly lower than blood velocities found *in vivo*. This decision was made to ensure that multiple time frames of phantom motion would be acquired given our FOV and undersampling parameters. Although we believe that the findings of this study may be extended to more complex, *in vivo*-like dynamics, including faster and non-constant blood velocities, further studies would be needed to confirm this belief.

4.5 Conclusions

In HYPR processing, a highly undersampled temporal weighting image is intentionally blurred and multiplied by a high SNR, nearly fully sampled composite image that contains temporally averaged information. In theory, the HYPR image spatial resolution is related to the composite image spatial resolution, while the HYPR image temporal resolution is related to the weighting image temporal resolution. The purpose of this work was to investigate the spatial and temporal fidelity of HYPR processing using a computer-controlled motion phantom designed to simulate the imaging environment encountered in peripheral MRA.

One potential limitation of the HYPR algorithm is that the spatial blur imposed on the weighting image may result in unintentional temporal weighting of nearby vessels. In this work, it was demonstrated that these effects were small, and could be controlled by ensuring that the weighting image reconstruction technique is strategically chosen to yield a narrow point spread function while providing a sufficient increase in weighting image SNR and decrease in undersampling artifacts. The penalties for using a sub-optimal weighting image reconstruction technique were discussed. It was shown that in general, with the use of an optimized weighting image reconstruction technique, the spatial fidelity of the HYPR image is not reduced. Signal intensity profiles measured in the HYPR processed images yielded FWHM values very similar to those measured in Time-Frame images. These results were confirmed by observing the same phenomenon in profiles obtained from *in vivo* images.

Measurements of the position and blur of the leading edge of the motion phantom demonstrated that HYPR processing effectively preserved the temporal fidelity inherent in the weighting image, despite being multiplied by the composite image. There was a small amount of signal from the composite image that was imprinted on the HYPR image, but the amplitude of this signal is small, and is not seen in *in vivo* images, presumably because this signal is lost in the noise. HYPR processing also preserved the different temporal behaviors of the artery and vein components within a single time series. Furthermore, the measured locations of the leading edge in consecutive time frames accurately portrayed the constant phantom velocity that was programmed for the experiment.

Finally, while this experiment was specifically designed to mimic a peripheral MRA examination, we believe these findings to be applicable to a broad range of anatomical regions with similar temporal-spatial correlation and sparsity where HYPR may be used as a post-processing technique.

Chapter 5: Hybrid 3D Radial Acquisition with Parallel Imaging and HYPR Reconstruction

5.1 Introduction

It has been shown that the hybrid 3D radial (stack-of-stars/SOS) k-space trajectory is well-suited for dynamic contrast-enhanced MR angiography of the peripheral vasculature (32,62,63). This is due in large part to the high compatibility of the trajectory with the anatomical geometry. HYPR reconstruction has also been used with SOS to increase either temporal or spatial resolution of peripheral angiography exams while maintaining high SNR and limiting the effects of angular undersampling(43).

Conventionally, to conform to the geometry of the lower legs, radially sampled planes were acquired in the coronal orientation, with the slice direction along the anterior/posterior (A/P) direction of the subject. Spins within a thick A/P slab were excited; the thickness of the slab was determined by the desired coverage in the slice direction. The major vasculature resided within the excitation slab, however the entire anatomy in the A/P direction was not necessarily excited. Conversely, while only the prescribed extent of spins was excited in the A/P direction, there was no limitation on the superior/inferior (S/I) extent of spin excitation (Figure 5.1a). Unfortunately, excited spins outside of the imaging FOV can cause strong undersampling artifact due to increased undersampling factors of these spins and the increasing gradient non-linearity at the edge of the B_0 field.

To avoid the increased undersampling artifact originating from excited spins outside the field of view, Du et al. (64) proposed a scheme for dynamic contrast-enhanced MR angiography of the peripheral vasculature wherein radially sampled planes were acquired in the coronal orientation, but the excitation was performed in the S/I direction. With this approach, only the spins within the imaging FOV in the S/I direction were excited (Figure 5.1b). To avoid wrap-around artifact from excited but un-encoded spins, this approach necessitates increased slice coverage to ensure the inclusion of the entire extent of the excited spins in the A/P direction. In order to maintain high temporal resolution, a degradation of the through-plane spatial resolution was required when the S/I excitation scheme was utilized.

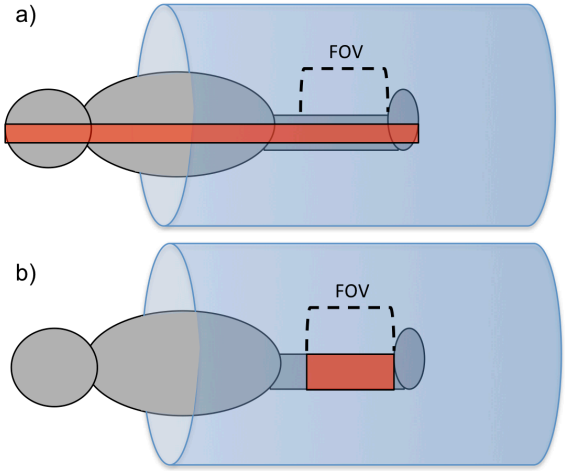

Figure 5.1: a) Coronal excitation of spins for a conventional peripheral MR angiography exam. Note that only a prescribed extent of spins in the anterior/posterior direction are excited (denoted by the red box), however there is no limitation to spin excitation in the superior/inferior direction. b) In the axial excitation, the superior/inferior extent of spin excitation is limited, but spins from the entire anatomy in the anterior/posterior direction are excited.

However, one feature of the SOS k-space trajectory is its compatibility with robust, Cartesian parallel imaging techniques in the slice direction. In this work, a coil-by-coil data-driven parallel imaging algorithm was applied to the slice-encoding direction of a SOS acquisition to achieve high through-plane spatial resolution while maintaining high temporal resolution.

5.2 Methods

All examinations were performed on a 3.0T scanner (Discovery MR750, GE Healthcare) using a 32-channel phased array abdominal coil (GE Healthcare). A resolution phantom was imaged using the following protocol to verify the prescribed increase in through-plane spatial resolution after the implementation of auto-calibrated reconstruction with

Cartesian-sampling (ARC) parallel imaging: 0.9375 x 0.9375 mm in-plane spatial resolution; 1.5 mm (SOS) or 1.0 mm (SOS + ARC) slice thickness; 512 x 512 in-plane imaging matrix; 512 projections/slice; TE/TR: 1.4/5.0 ms; flip angle/bandwidth: 15°/±125.0 kHz.

For *in vivo* studies, data were acquired from four healthy volunteers using the imaging protocol described below. Gadobenate dimeglumine contrast agent (MultiHance, Bracco Diagnostics) was administered via an MR compatible power injector at a rate of 3.0 ml/s and dose of 0.1 mmol/kg of body weight after the acquisition of a pre-contrast mask that was also accelerated with parallel imaging. A saline flush of 20.0 ml at 3.0 ml/s followed the contrast material injection. Informed, written consent was obtained from all volunteers, in accordance with the Institutional Review Board-approved protocol.

Other *in vivo* imaging parameters included: either 0.9375 x 0.9375 mm or 1.0 x 1.0 mm in-plane spatial resolution over a 480 mm field of view (FOV); 1.0 mm slice thickness covering the entire A/P extent of the anatomy; 75 – 85% fractional echo; 6.2 – 6.6 seconds/frame; 20 projections/slice/frame; angular undersampling factor of 37.6 - 40 (compared to Cartesian acquisition of the same matrix size); TE/TR: 1.4/5.0 ms; flip angle/bandwidth: 15°/±125.0 kHz.

5.2.1 SOS Acquisition with Parallel Imaging

Figure 5.2a diagrams the classic SOS k-space trajectory, wherein Cartesian phase encoding is employed in the slice – or k_z – direction and data are sampled radially in the

k_x-k_y plane. In this implementation, ZIPR(32) encoding was utilized; all slices of a given projection angle were acquired before advancing to the next projection, filling up a projection readout by slice-encoding plane for each projection angle. Projection angle acquisition order was determined by the Golden Angle scheme(65).

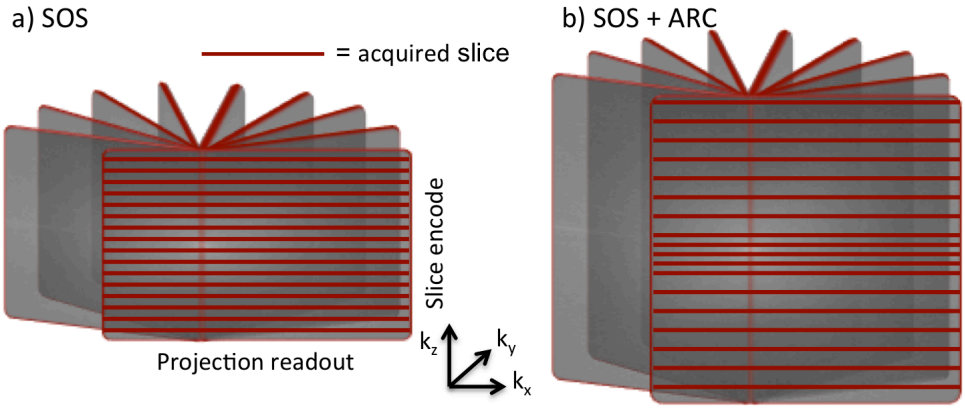

Figure 5.2: a) The classic Stack-of-stars (SOS) trajectory. K-space is radially sampled in plane, while Cartesian phase encoding is employed in the slice direction. b) The SOS trajectory with parallel imaging employed in the slice encoding direction. Improvements in spatial resolution due to the addition of parallel imaging will manifest in the slice encoding direction.

Figure 5.2b shows how the classic SOS trajectory was altered by the inclusion of parallel imaging. The spatial resolution improvements resulting from the addition of parallel imaging manifest in the A/P – or k_z – direction. Note that in Figure 5.2b, every other slice is left un-acquired, except for central slices (16 slices in this work), which are fully sampled. This leads to an acceleration factor of R≈2. The fully sampled, central region serves as the auto-calibration lines necessary to determine the reconstruction weights in the parallel imaging reconstruction algorithm.

5.2.2 Parallel Imaging Reconstruction

Parallel imaging reconstruction was performed using a coil-by-coil data-driven calibration technique similar to the GRAPPA method(66) - Auto-calibrated Reconstruction with Cartesian sampling (ARC)(67). Mask subtraction of k-space data was performed prior to parallel imaging calibration and reconstruction. A kernel size of 5 points along the readout direction x 7 points along the slice-encoding direction was used for the ARC algorithm, which was performed for every accelerated projection readout by slice-encoding plane.

5.2.3 HYPR Reconstruction

For the *in vivo*, dynamic studies, time frames were processed using the HYPR LR(46) algorithm. The generalized HYPR LR image reconstruction formula can be expressed as:

Equation 5.1

$$I_H(t) = I_C \cdot I_W(t) = I_C \cdot \frac{\Phi(k_t)}{\Phi(k_t^C)}$$

where I_C is a well-sampled composite image with high SNR, high spatial resolution, and limited or no temporal information; $I_W(t)$ is the unique weighting image for time frame t; Φ represents a low spatial resolution weighting image reconstruction technique for k-space data (k_t) that is applied in an effort to reduce aliasing artifacts and improve SNR relative to the corresponding non-HYPR-processed image. In the implementation used here, HYPR processing is performed on each two-dimensional coronal slice individually, and the spatial resolution loss in the weighting image manifests in-plane only.

5.3 Results

Figure 5.3 confirms the increase in spatial resolution attainable when the SOS + ARC protocol is used. The figure shows axially reformatted images of a spatial resolution phantom from datasets acquired in the coronal orientation; the slice encoding direction of the SOS (a) and SOS + ARC acquisition (b) is labeled. Both images are fully-sampled in the angular dimension; there is no angular undersampling. The improvement in spatial resolution – from 1.5 mm to 1.0 mm – can easily be appreciated. It should be noted that not only was spatial resolution in the slice direction improved with the implementation of parallel imaging, but the temporal resolution of the SOS + ARC protocol is superior to the lower spatial-resolution SOS protocol. This is represented by the data acquisition time reported in Figure 5.3.

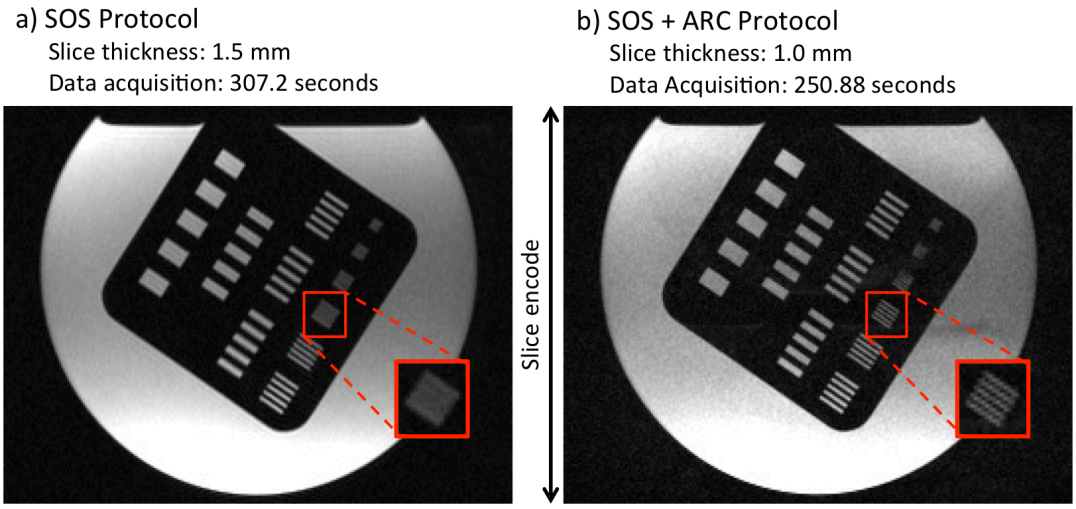

Figure 5.3: Results from a resolution phantom scanned with the classic SOS protocol (a) and the SOS + ARC protocol (b). The improved spatial resolution can easily be appreciated by inspection of the highlighted segment of the images. The improvement in scan time is indicative of the improved temporal resolution possible with the SOS + ARC protocol.

Figure 5.4 demonstrates the aliasing artifact present in the SOS + ARC acquisition protocol if ARC reconstruction is not used (Figure 5.4a) and successful un-aliasing of accelerated data after ARC reconstruction (Figure 5.4b). Data shown are in the form of a fully sampled, non-time-resolved MR angiogram. Restricted axial maximum intensity projections (MIPs) and sagittally reformatted MIPs of a single leg are shown on the left and right columns, respectively. Red arrows highlight easily distinguished aliased vessels in 5.4a and the corresponding lack of aliasing in 5.4b.

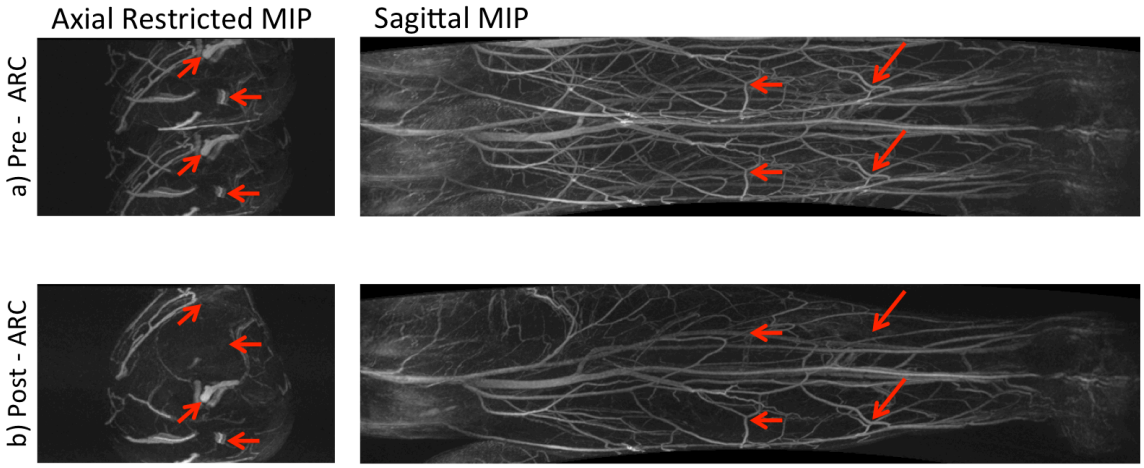

Figure 5.4: a) Data acquired with the SOS + ARC protocol prior to ARC reconstruction. Aliasing artifact is clearly present (red arrows) in both the axial limited MIP (left) and the sagittal MIP (right) of a single leg. b) Data acquired with the SOS + ARC protocol after ARC reconstruction was performed to unwrap phase aliasing. Locations of aliasing artifact in (a) are now free of such artifact after ARC reconstruction (red arrows).

Figures 5.5 and 5.6 compare results from SOS and SOS + ARC protocols with HYPR LR reconstruction for the same healthy volunteer. In Figure 5.5, four consecutive coronal MIP time frames are shown for each protocol (5.5a: SOS and 5.5b: SOS + ARC). In-plane resolution for both exams is 0.9375 x 0.9375 mm. The SOS series shown in Figure

5.5a was the last of three contrast agent material injections administered to this volunteer. There is residual contrast agent material that was not sufficiently removed by the mask subtraction (red arrows). This venous signal is apparent in the non-HYPR-processed images, therefore it is not a result of HYPR processing. Note that the benefits resulting from the implementation of parallel imaging manifest as an improvement in both spatial and temporal resolution: 1.5 mm slice thickness versus 1.0 mm slice thickness and 7.0 seconds/frame versus 6.3 seconds/frame. The MIP images in Figure 5.6 are from a single arterial time frame and have been reformatted into the sagittal direction to illustrate the improved slice thickness. The right and left legs of the volunteer are shown in individual MIP images for each protocol (labeled R and L, respectively).

a) SOS : Coronal MIPs

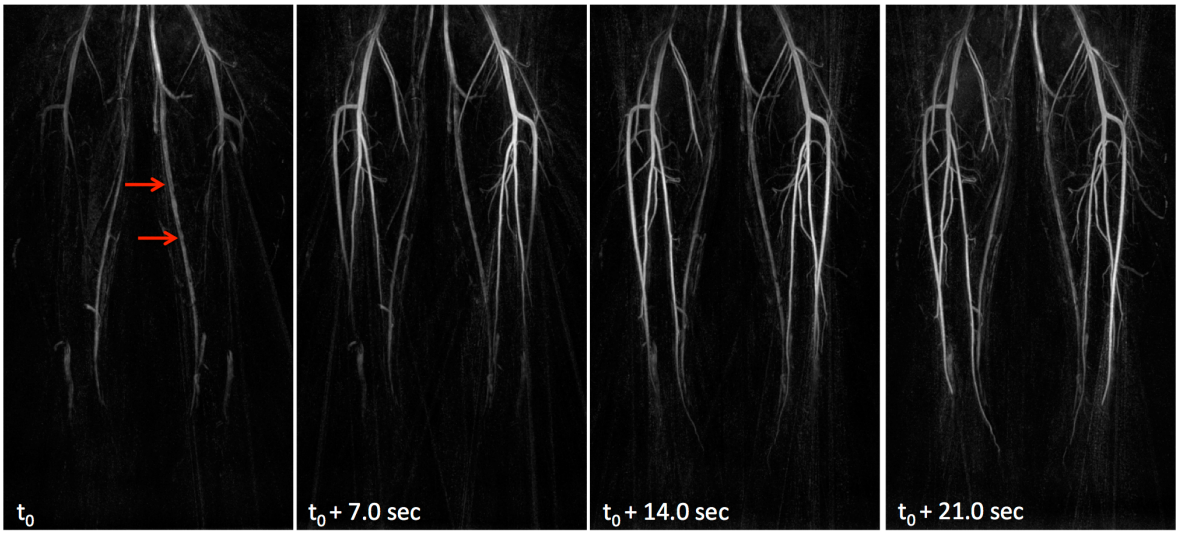

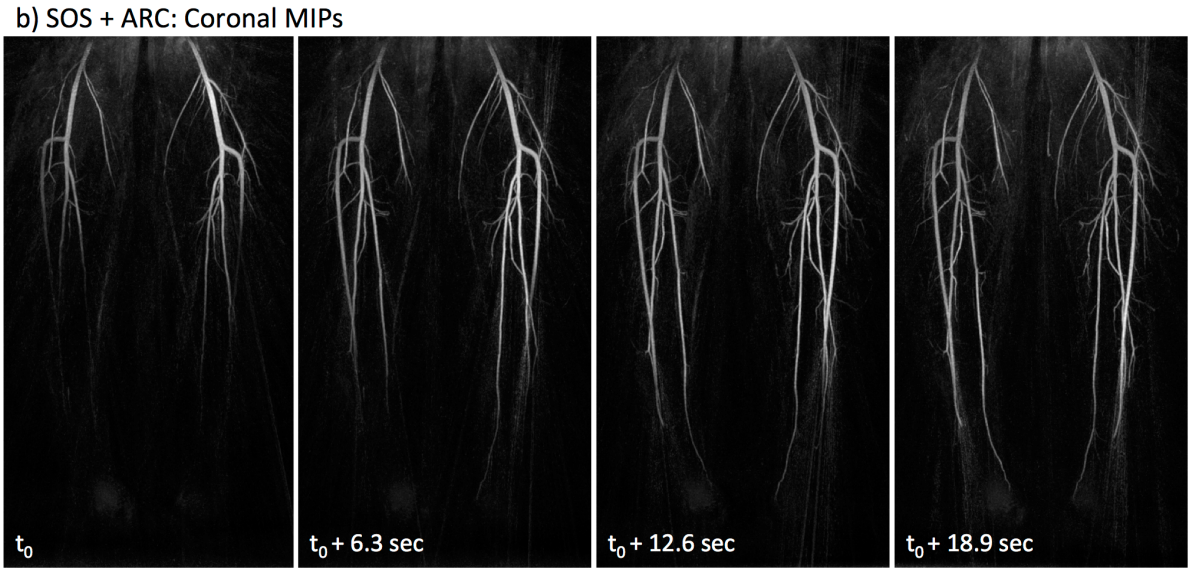

Figure 5.5: Four consecutive arterial MIP images obtained and reconstructed with HYPR LR from a healthy volunteer with a) an SOS protocol and b) an SOS + ARC protocol. The red arrows in Figure 5.5a point to an area of erroneous, early venous enhancement. Other imaging parameters include: 10.9 ml gadobenate dimeglumine; 0.9375 x 0.9375 mm in-plane spatial resolution; 106 and 61 slices acquired for a) and b) respectively. The SOS series in a) was the third of three injections in the examination, while the SOS + ARC series in b) was the second of three injections.

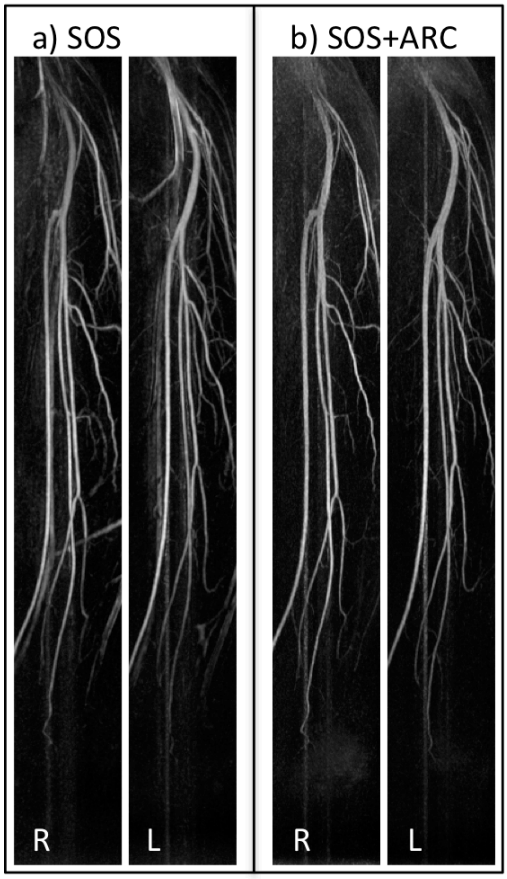

Figure 5.6: Sagitally reformatted MIP images reconstructed with HYPR LR of the right and left (R and L) legs of the healthy volunteer from Figure 5.5. Image series were obtained with a) an SOS protocol and b) an SOS + ARC protocol.

Figures 5.7 and 5.8 show results from the SOS + ARC acquisition protocol and HYPR LR reconstruction for two healthy volunteers. Results are presented as coronal MIP images of consecutive time frames and a sagitally reformatted, arterial frame MIP of the volunteer's right leg. The addition of parallel imaging to the protocol resulted in an improvement in both temporal and spatial resolutions for the datasets shown in Figures 5.7 and 5.8. For comparison, with no parallel imaging, imaging parameters for the healthy volunteers shown would be: 1.5 mm slice thickness and 7.84 seconds/frame

(Figure 5.7); 1.5 mm slice thickness and 7.2 seconds/frame (Figure 5.8). Imaging parameters for the SOS + ARC results shown are 1.0 mm slice thickness for both datasets and 6.6 seconds/frame and 6.2 seconds/frame, respectively. Other imaging parameters can be found in the figure caption.

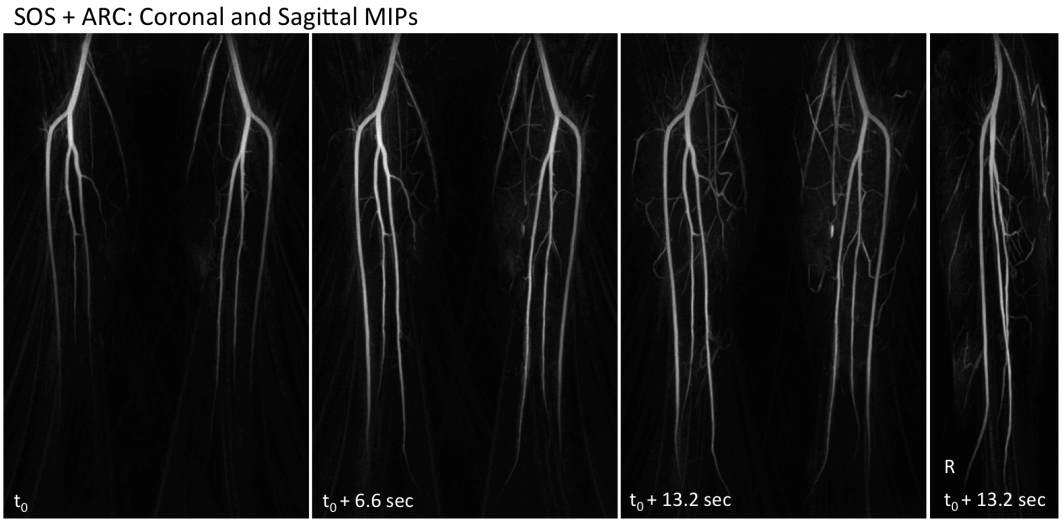

Figure 5.7: Three consecutive MIP time frame images and a sagitally reformatted MIP image of a single leg from a healthy volunteer. Data were acquired with the SOS + ARC protocol and reconstructed with HYPR LR. Other imaging parameters include: 18.3 ml gadobenate dimeglumine; 1.0 x 1.0 mm in-plane spatial resolution; 68 acquired slices. The series shown was acquired during the first of three injections administered during the examination.

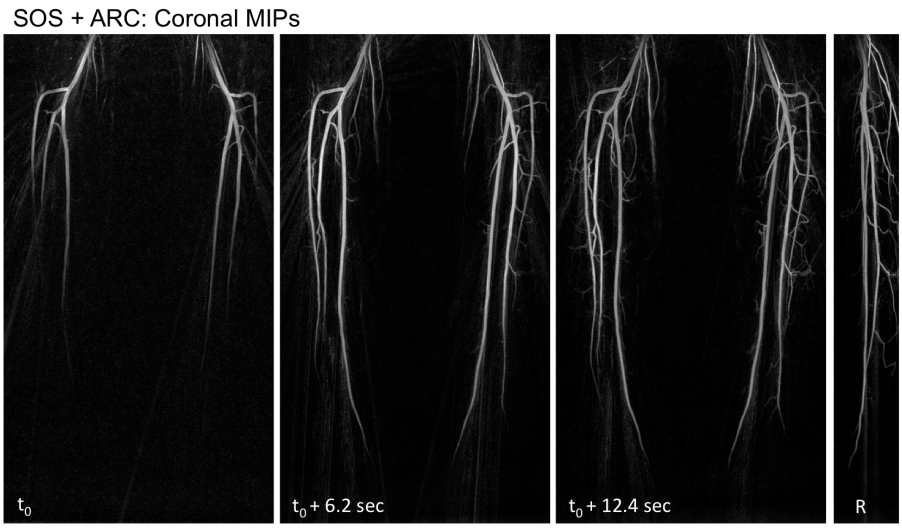

Figure 5.8: Three consecutive MIP time frame images and a sagitally reformatted MIP image of a single leg from a healthy volunteer. Data were acquired with the SOS + ARC protocol and reconstructed with HYPR LR. Other imaging parameters include: 12.6 ml gadobenate dimeglumine; 0.9375 x 0.9375 mm in-plane spatial resolution; 62 acquired slices. The series shown was acquired during the first of three injections administered during the examination.

5.4 Discussion

This study is not without limitations, one of which is the relatively small sample size; four healthy volunteers were scanned using the SOS + ARC protocol. While the combination of ARC parallel imaging and SOS k-space trajectory was generally successful and provided improvements in both spatial and temporal resolution compared to a SOS protocol with A/P excitation and no parallel imaging, it was found that other acquisition techniques described in forthcoming chapters could offer even further improvements.

Another limitation is the use of the Golden Angle projection-ordering scheme. In radial sampling, it is important to evenly space the projection angles to ensure uniform angular

sampling. The most effective way to enforce evenly spaced projections requires *a priori* knowledge of the number of projections/slice/frame to be used during the reconstruction. However, the optimal number of projections is not always known during the early, developmental stages of a protocol. The Golden Angle scheme allows more freedom to retrospectively adjust the number of projections included in a single frame while minimizing angular clumping.

5.5 Conclusion

In this work, a coil-by-coil data-driven parallel imaging technique was successfully applied to the slice encoding direction of a hybrid 3D radial trajectory. Aliasing artifacts due to the parallel imaging acquisition were successfully un-wrapped; no residual aliasing artifacts were seen. The implementation was achieved with no significant g-factor related loss of SNR(68).

The utilization of the anterior/posterior excitation slab reduced the number and intensity of undersampling artifacts from signal outside the imaging field of view. The combination of SOS + ARC acquisition protocol and HYPR LR reconstruction allowed for high quality time-resolved images with spatial and temporal resolution superior to previous techniques. While the implementation of parallel imaging allowed for a significant improvement in slice thickness, this improvement might be difficult to recognize by visual inspection of data acquired from healthy volunteers. It is hypothesized that the improvement in slice thickness would be more highly appreciated in a patient with PAD; a more accurate and confident assessment of stenosis severity would be possible with

the spatial resolution offered by the SOS + ARC protocol. This hypothesis was not tested in the work presented here.

The technique described in this chapter is readily applicable to the imaging of other anatomy. For example, the hybrid 3D radial k-space trajectory has been implemented for imaging intra-cranial aneurysms or fast imaging of the coronary arteries. Both of these applications could benefit from the improved spatial and temporal resolution possible with the SOS + ARC protocol.

Chapter 6: True 3D Radial Acquisition with HYPR Reconstruction for Peripheral MR Angiography

6.1 Introduction

Unlike the hybrid 3D radial (SOS) acquisition strategy, which samples k-space radially in two dimensions and employs Cartesian phase encoding in the slice direction(32), the vastly undersampled isotropic projection reconstruction (VIPR) acquisition strategy samples lines in k-space that are truly radial in three dimensions(39). The potential benefits and challenges of applying the VIPR sampling strategy to peripheral MRA exams were discussed in Chapter 2. In summary, though the large, isotropic field of view provided by VIPR is not well tailored to the anatomy, the VIPR trajectory offers higher undersampling factors combined with more benign undersampling artifacts compared to

the SOS acquisition. These benefits make VIPR well-suited to dynamic, contrast-enhanced MR angiography applications, regardless of anatomic geometry.

Studies have previously been performed to investigate the application of VIPR to peripheral MR angiography exams. These studies typically achieved 1.25 – 1.5 mm spatial resolution utilizing tornado filtering(69) to reconstruct a time-resolved series. Also, a single dose (0.1 mmol/kg) of gadolinium-based contrast agent was employed for each station of these studies, which corresponded to a triple dose of contrast per examination. Also, exams in these studies were performed on a 1.5 T scanner with an 8-channel peripheral vascular coil. In this work, the VIPR k-space acquisition is combined with HYPR LR(46) reconstruction to achieve time-resolved, contrast-enhanced images of the peripheral vasculature with 1.0 mm isotropic spatial resolution and 4.5 – 6.5 second temporal resolution. Furthermore, the feasibility of acquiring a time-resolved dataset using fractional doses (<0.1 mmol/kg) of contrast agent was investigated.

6.2 Methods

A robust VIPR acquisition and HYPR LR reconstruction protocol was developed based on the results of exams performed on 15 healthy volunteers using a 3.0T scanner (Discovery MR750, GE Healthcare) and a 32-channel phased array abdominal coil (GE Healthcare). For each time series, a full, 0.1 mmol/kg dose of gadobenate dimeglumine (MultiHance, Bracco Diagnostics) was injected at a rate of 3.0 ml/s by an MR-compatible power injector after the acquisition of a non-contrast-enhanced mask dataset. The contrast injection was immediately followed by 20.0 ml flush of saline delivered at 3.0

ml/s. Axial excitation was used for VIPR acquisitions to yield the benefits described in the previous chapter. For each volunteer in this stage of the project, between 40,000 and 45,000 unique projection angles were acquired during the course of data acquisition. Note that the 480 x 480 x 480 imaging matrix was undersampled by a factor of 8 to 9. This is important because, though the composite image in HYPR LR reconstruction may utilize all the data acquired and therefore be called a “full composite”, the three-dimensional matrix corresponding to the composite image was not fully-sampled. The projections were prospectively sorted into subsets of 1,000 – 1,500 equally spaced projection angles that uniformly sampled the surface of the k-space sphere. These subsets, or interleaves, contained the information for a single time frame. The projection angle order of acquisition within each interleave was sequential, while the order of the interleaves themselves was bitreversed. Other typical scan parameters for this stage of the project include: 480 x 480 x 480 mm field of view; 1.0 x 1.0 x 1.0 mm spatial resolution; fractional echo of 75-85%; TR/TE/FA/BW of 4.8ms/1.1ms/20°/±125kHz.

HYPR LR reconstruction was performed on the data from each healthy volunteer exam. The composite image was reconstructed using all the data acquired, between 40,000 and 45,000 projections. The weighting image was created using the projections from a single subset of data, typically 1,000 to 1,500 projections. Weighting image SNR was improved by utilizing a low spatial resolution reconstruction technique; k-space data outside a radius of 100 pixels were dampened prior to performing the Fourier transform. This strategy is discussed in more detail below.

After the initial 15 healthy volunteer exams were performed and the robust acquisition/reconstruction protocol described above was established, the feasibility of utilizing said protocol to obtain high quality time-resolved, contrast-enhanced MRA exams of the peripheral vasculature using contrast doses less than 0.1 mmol/kg was explored. Seventeen healthy volunteers were recruited for this stage. On each volunteer, three separate injections and imaging series were acquired using 0.025, 0.05 and 0.1 mmol/kg of gadoenate dimeglumine (quarter and half and full doses, respectively). The order of the assorted contrast dose injections varied, but is noted alongside the results presented below. Multiple injection protocols were tested during this time with the intent of creating a robust protocol to apply to a cohort of patients. Injection protocols under investigation included: adjusting the contrast injection rate so that the total time of the injection remained constant and diluting the contrast with saline so that the total volume injected for each contrast dose remained constant.

In the third stage of this project, ten patients diagnosed with peripheral artery disease were recruited and examinations were performed using the VIPR/HYPR LR protocol with the injection of fractional doses of gadobenate dimeglumine. The injection protocol for patient examinations is summarized in Figure 6.1. For fractional doses, the contrast bolus was diluted with saline so the total volume of the bolus remained constant among the three injections: 0.2 ml/kg. A 20 ml saline flush was administered immediately following the contrast media injection. All volumes were injected at a rate of 3.0 ml/s. A waiting period of 20 minutes was maintained between contrast-enhanced acquisitions to limit the negative effects of having contrast agent on-board in later acquisitions. The

contrast doses administered in the first and second injections were randomized between quarter and half doses. The full contrast dose was always the third injection.

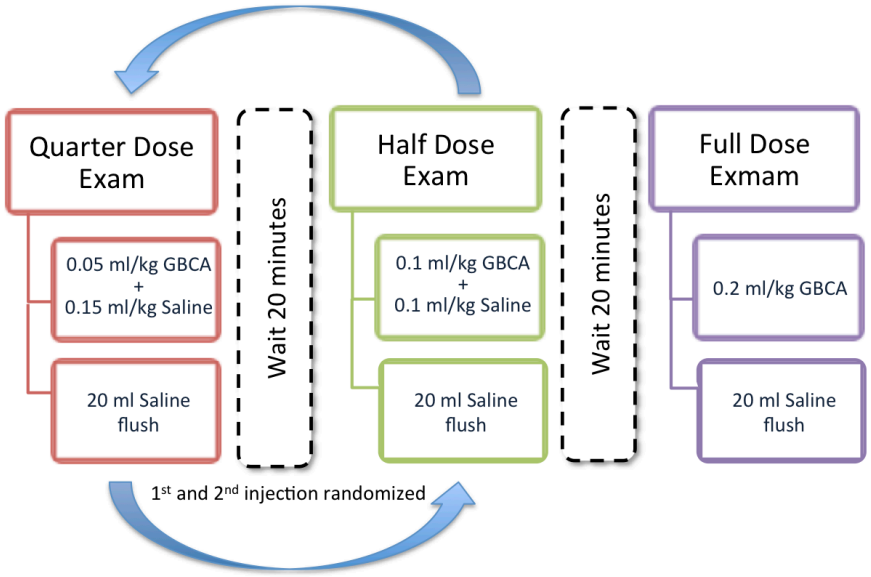

Figure 6.1: The injection protocol for the patient examinations. Note that the dose administered first was randomized between quarter and half doses.

The data acquisition parameters for patient examinations included: 400 x 400 x 400 mm field of view; 1.0 x 1.0 x 1.0 mm spatial resolution; 36,000 unique projection angles acquired (undersampled by a factor of 7); 1,200 projections/frame (undersampled by a factor of 209 compared to a Cartesian matrix of the same size); 5.28 seconds/frame; fractional echo of 80%; TR/TE/FA/BW of 4.4ms/1.2ms/20°/±125kHz.

Typically during the reconstruction of a VIPR dataset, weighting factors are applied to normalize the effective sampling density across k-space, see the difference between 'VIPR' and 'Fully Compensated VIPR' in Figure 6.2a, which plots a one-dimensional profile through isotropic, three-dimensional effective sampling density functions of VIPR

trajectories with and without density compensation terms. During the formation of the HYPR LR weighting image, SNR and undersampling artifact level were improved by utilizing a low resolution reconstruction of the time frame data; density compensation weights were not applied to k-space data outside a radius of 100 pixels, which had the result of effectively rolling off the signal from high spatial frequencies like $\frac{1}{k_r^2}$, see Figure 6.2a. A one-dimensional profile of the isotropic, three-dimensional weighting image reconstruction technique point-spread-function (PSF) is plotted in Figure 6.2b, along with the PSF of a fully compensated VIPR image. The weighting image reconstruction technique introduces a very small amount of image blur into the weighting image. HYPR LR reconstruction was performed on the patient datasets using a full composite image (36,000 projections).

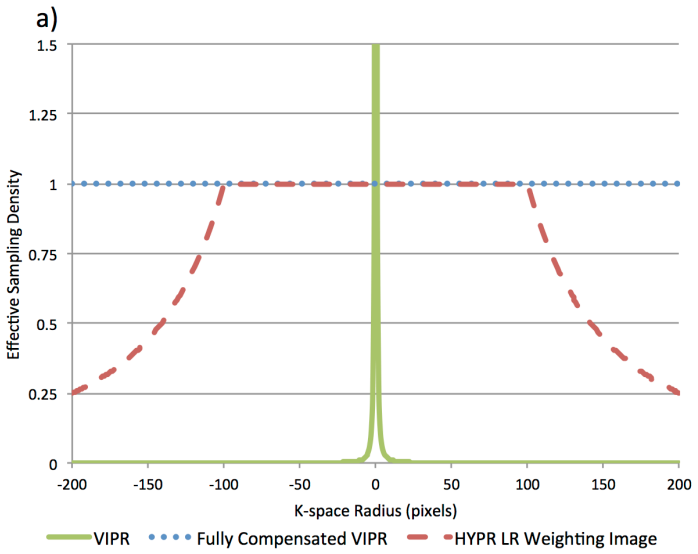

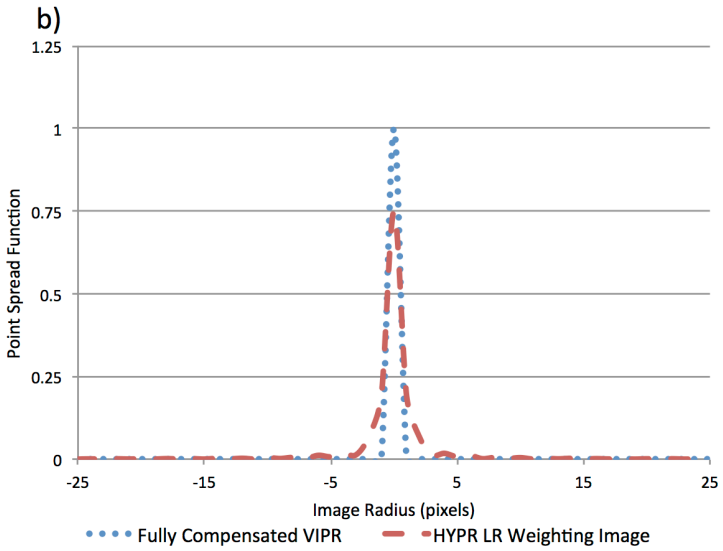

Figure 6.2: One-dimensional profiles through the three-dimensional, isotropic effective sampling density (a) and point-spread-functions (b) for VIPR, Fully Compensated VIPR and HYPR LR Weighting Images.

6.3 Results and Discussion

Figure 6.3 shows maximum intensity projections (MIP) images of three consecutive arterial time frames from an examination of a healthy volunteer with 0.1 mmol/kg of contrast agent (13.6 ml for this volunteer). In Figure 6.3a, undersampled non-HYPR-processed time frames are shown. Undersampling artifacts can easily be seen and are highlighted by the red arrows in Figure 6.3a. However, SNR is still relatively high, especially considering the aggressive level of undersampling by a factor of 346 compared to a fully sampled VIPR dataset.

The HYPR LR result (Figure 6.3b) shows improvements with regard to both the level of artifact and SNR. The small artery (yellow arrow) branching from the volunteer's right

posterior tibial artery is clearly visible in the HYPR LR time frame due to the increased SNR. Furthermore, the undersampling artifacts visible in Figure 6.3a are removed by HYPR LR processing (red arrows). These improvements are achieved with no visible penalty to temporal fidelity.

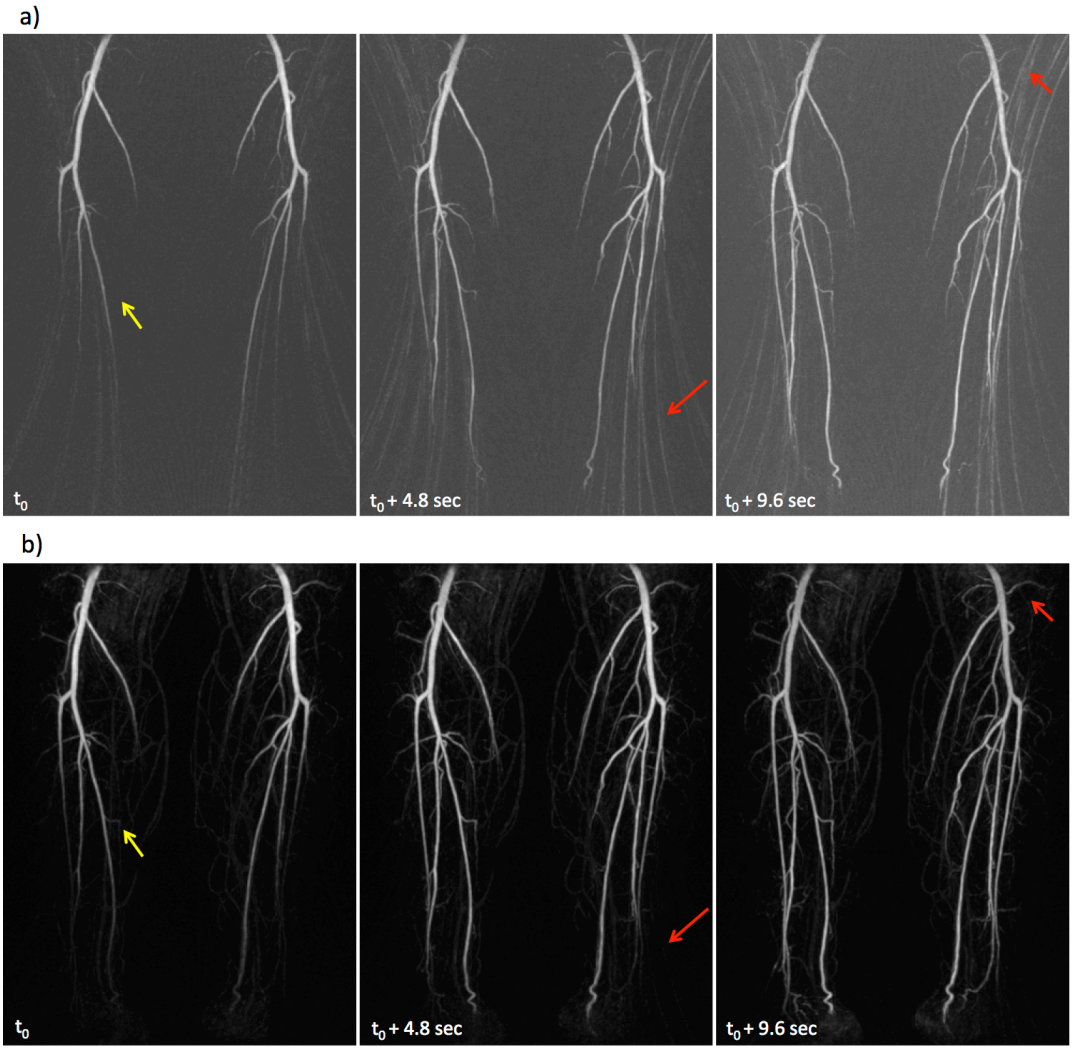

Figure 6.3: MIP images of three consecutive arterial time frames from a healthy volunteer. Non-HYPR-processed (a) and HYPR LR (b) images are shown. Undersampling artifacts (red arrows) are removed by HYPR LR processing and SNR improvement can be appreciated by the visualization of the small branching artery in the HYPR LR images (yellow arrow).

Figure 6.4 shows coronal MIP images of HYPR LR arterial time frames from a healthy volunteer (weight: 58 kg) after a quarter (6.4a: 2.9 ml), half (6.4b: 5.8 ml) and full (6.4c: 12.0 ml) dose of contrast agent was administered. The order of injection during the examination matches the order of display in Figure 6.4. In this exam, the rate of injection was adjusted for each contrast dose so that the total time of contrast injection remained constant; the contrast agent was not diluted. Imaging parameters specific to this volunteer include: 1.0 mm isotropic spatial resolution; 1,500 projections/frame (undersampling factor of 240 compared to a fully sampled VIPR dataset); 6.75 second temporal resolution. Note that the three images shown are from separate injections; direct comparison of the temporal information contained in each image is not meaningful. There is slightly lower SNR in the quarter dose exam, however all three contrast doses result in high quality peripheral MR angiograms.

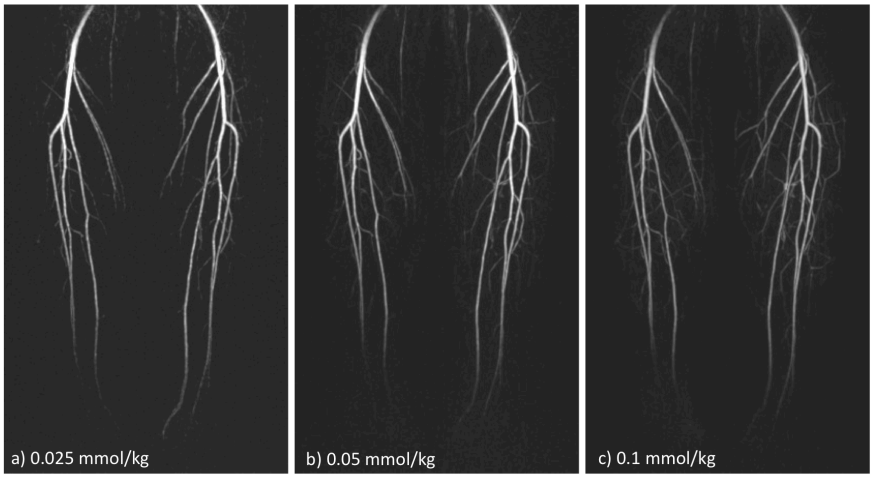

Figure 6.4: MIP images of HYPR LR arterial time frames from a healthy volunteer obtained after a quarter (a), half (b) and full (c) dose of gadobenate dimeglumine was administered. The order of injection matches the order of display. The doses were injected intravenously at a rate of 0.75 ml/s (a), 1.5 ml/s (b) and 3.0 ml/s (c).

Figure 6.5 shows arterial MIP images of HYPR LR time frames from a healthy volunteer (weight: 108 kg) after quarter (6.5a: 5.0 ml), half (6.5b: 10.0 ml) and full (6.5c: 20.0 ml)

doses of contrast agent were administered. In this case, the volunteer's full dose based on weight (21.6 ml) exceeded the maximum volume per injection allowed by the IRB-approved protocol, so dosages were calculated using 20.0 ml as the full dose. In this examination, contrast boluses were diluted with saline so the contrast bolus volume was constant for all injections. This injection protocol is superior to the one used for the volunteer in Figure 6.4 as it allows for more variables to be held constant across the three injections. Imaging parameters specific to this volunteer include: 1.0 mm isotropic spatial resolution; 1,000 projections/frame (undersampling factor of 360 compared to a fully sampled VIPR dataset); 4.7 second temporal resolution. Similar to the results shown in Figure 6.4, high quality angiograms were obtained with only a quarter dose of contrast agent.

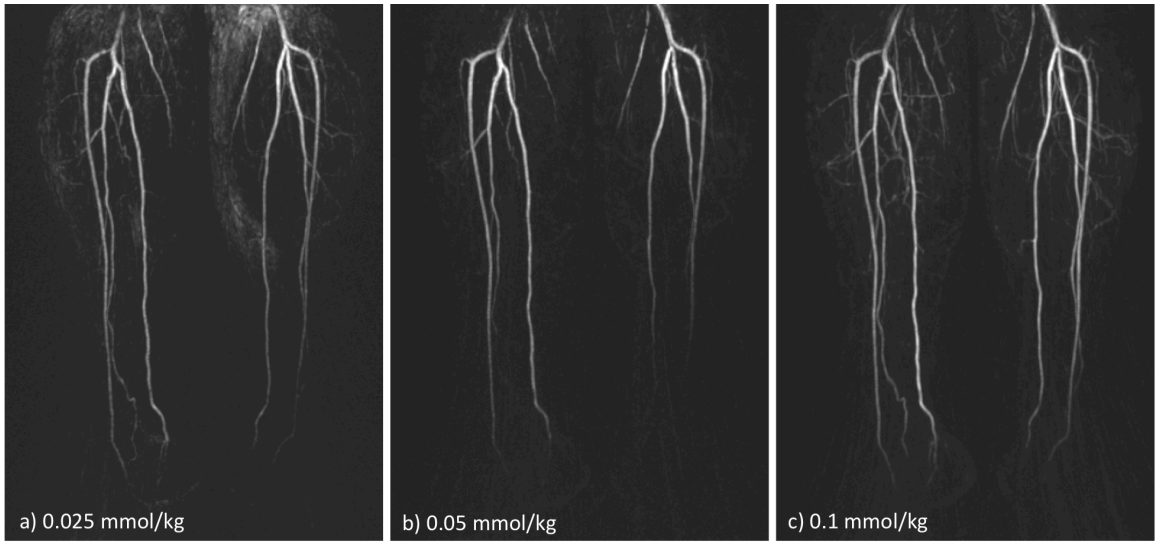

Figure 6.5: MIP images of HYPR LR arterial time frames from a healthy volunteer obtained after a quarter (a), half (b) and full (c) dose of gadobenate dimeglumine was administered. The order of injection matches the order of display. The injection protocol displayed in Figure 6.1 was utilized here.

Figure 6.6 shows arterial MIP images of HYPR LR time frames from a patient with peripheral artery disease (weight: 74 kg) after the administration of a quarter (6.6a: 3.7 ml), half (6.6b: 7.4 ml) and full (6.6c: 14.8 ml) dose of contrast agent. The injection order matches the order of images displayed in Figure 6.6. Imaging parameters specific to this patient include: 1.0 mm isotropic spatial resolution; 1,200 projections/frame (undersampling factor of 209 compared to a fully sampled VIPR dataset); 5.28 second temporal resolution. Similar to the healthy volunteer examinations, the combination of VIPR acquisition and HYPR LR reconstruction allows for the creation of high quality angiograms in this patient with the use of only 0.025 mmol/kg of contrast agent. The disease is clearly visible in all three dose images: the severe stenoses in the patient's left anterior tibial (solid yellow arrow) and peroneal (dashed yellow arrow) arteries and the occlusion of the patient's right peroneal artery (dashed red arrow).

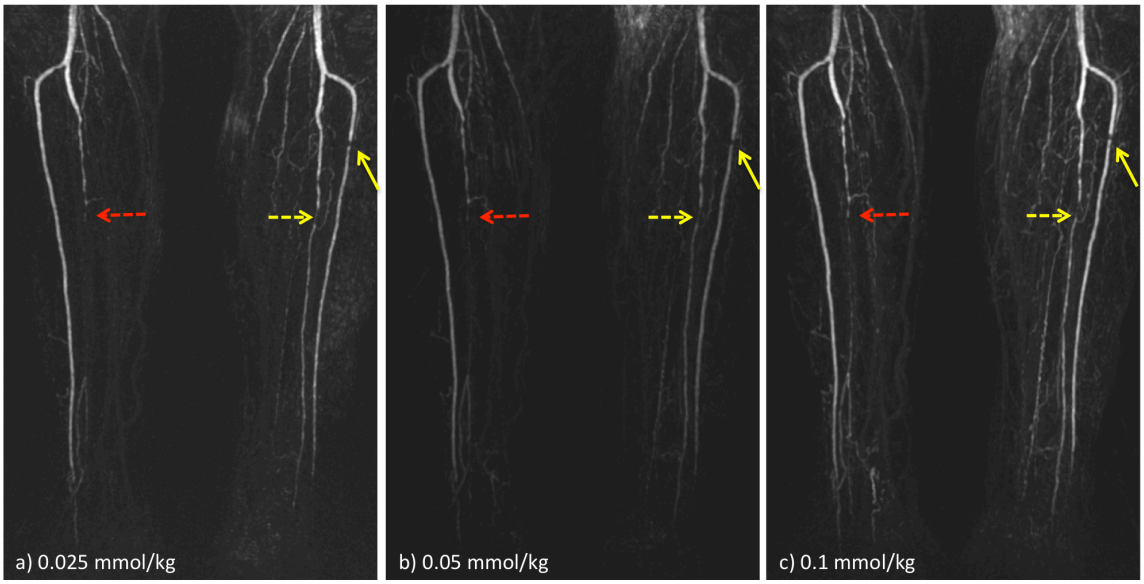

Figure 6.6: MIP images of HYPR LR arterial time frames from a patient with PAD obtained after a quarter (a), half (b) and full (c) dose of gadobenate dimeglumine was administered. The order of injection matches the order of display. The injection protocol displayed in Figure 6.1 was utilized.

6.4 Conclusions

The combination of VIPR k-space acquisition and HYPR LR reconstruction resulted in high quality, time-resolved MRA series of the peripheral vasculature in both healthy volunteers and patients. The feasibility of applying this imaging protocol to achieve similar high quality results with the administration of fractional doses of contrast agent was also investigated. In healthy volunteers, image quality endured only minimal penalties in the form of slight SNR decrease in series obtained with 0.025 mmol/kg of gadobenate dimeglumine. Diagnostic quality images were produced with isotropic spatial resolution of 1.0 mm and temporal resolutions between 4.8 and 6.75 seconds after the administration of 2.9 – 5.0 ml of contrast agent (depending on subject weight).

The presence of pathology will typically cause a reduction in image quality, due to lack of vascularization and consequent decrease in signal from contrast-enhanced blood. Promising results in healthy volunteers do not necessitate similarly positive results in patients. Therefore, this work extended to test the feasibility of low-dose exams in a cohort of patients with peripheral vascular disease. Results for the initial feasibility study in patients were encouraging. A large-scale, statistic-based study investigating the potential effects of a low-dose exam on diagnostic ability and confidence is needed to further promote the use of this protocol. Such a project and its inherent difficulties are discussed in Chapter 8.

Chapter 7: Comparison of Image Quality and Diagnostic Agreement of VIPR/HYPR and TRICKS Protocols for Peripheral MRA

7.1 Introduction

HighlY constrained backPRojection (HYPR)(40) is a post-processing technique that improves upon the signal-to-noise ratio (SNR) and occurrence of undersampling artifacts in a set of time-resolved images while maintaining high temporal and spatial resolution. HYPR processing is most successful in instances of high image sparsity and/or high spatio-temporal correlation. Magnetic resonance angiography (MRA), therefore, is a well-suited application of the technique. Many authors have exploited the characteristics of HYPR to provide an improvement in SNR, temporal resolution and/or spatial resolution compared to currently utilized MRA methods(41-43,70-72). While these improvements are impressive, it has not yet been shown whether the superior image parameters translate into improved diagnostic capability.

In this study, a cohort of patients being treated for peripheral arterial disease (PAD) by our institution's Vascular Surgery department underwent research MRA examinations of the lower extremities prior to x-ray digital subtraction angiography (DSA) procedures and possible intervention. The MRA examination consisted of two imaging protocols: 1) comparable to a clinical MRA study of the lower extremities using a Cartesian view-sharing technique and 2) the proposed research protocol for the calf station consisting of a 3D radial k-space trajectory (VIPR)(39) and HYPR LR(46) post-processing. Two experienced cardiovascular radiologists interpreted the MRA images from both protocols. Grades were assigned to eleven vessel segments per leg by each reader to describe the severity of disease in each segment.

7.2 Methods

Nine patients were recruited from the University of Wisconsin Hospital and Clinic's Vascular Surgery department. The eligibility requirements for this study included having a diagnosis of PAD and a scheduled appointment for a procedure that would include x-ray DSA. Furthermore, per the Institutional Review Board-approved protocol, patients had to have a documented eGFR > 30.0 ml/min/1.72m^2. Informed written consent was obtained from each subject.

MRA exams were performed on a 3.0T MR scanner (Discovery MR 750, GE Healthcare) with a 32-channel phased-array abdominal coil (GE Healthcare, Waukesha, Wisconsin). After the acquisition of a pre-contrast mask dataset, each MRA series was obtained with

the administration of gadobenate dimeglumine contrast agent (MultiHance, Bracco Diagnostics, USA) followed by a saline flush (20.0 ml) injected in the antecubital fossa (except for Patient 1, injection in the hand) at a rate of 2.5 – 3.0 ml/s using an MR-compatible power injector. The contrast dose for each injection was 0.05 mmol/kg, unless the subject's contrast volume for a full dose (0.2 ml/kg) exceeded 20 ml. In these cases, 10 ml of contrast agent was administered per injection. Table 7.1 summarizes the injection protocol for each patient. The acquisition order of the two MRA protocols was randomized with a delay of 20 minutes between the contrast injections.

Patient Number	Weight (kg)	Contrast Volume for Full Dose (ml)	Contrast Volume Administered per Injection (ml)	Injection Rate (ml/s)
1	114.76	22.95	10	2.5
2	104.78	20.95	10	3.0
3	85.7	17.14	8.5	2.5
4	102.7	20.48	10	2.5
5	89.1	17.82	9	2.5
6	55	11	5.5	2.5
7	96.8	19.36	9.68	2.5
8	78.2	15.64	7.8	2.5
9	77.6	15.52	8	2.5

Table 7.1: Contrast injection information for each patient.

The clinically comparable MRA protocol was performed using the time-resolved imaging of contrast kinetics (TRICKS)(26) technique, which is a Cartesian view-sharing method. At our institution, parallel imaging is not typically utilized in the clinical setting. However, in order to represent the state-of-the-art of the technique, an R=2 parallel imaging acceleration factor in the left/right direction was prescribed using a sensitivity-encoding

method(73) (ASSET, GE Healthcare). Typical image parameters for the TRICKS time series include: 1.25 x 1.25 x 2.0 mm spatial resolution over a 400 x 320 x 124 mm field of view with a temporal update rate of 6.1 seconds. The imaging prescription deviated slightly from the typical protocol in three patients due to the size of the anatomy. (Patient 1: 1.25 x 1.312 x 2.0 mm spatial resolution over 480 x 336 x 124 mm FOV; Patient 2: 1.25 x 1.22 x 2.0 mm spatial resolution over 480 x 312 x 124 mm FOV; Patient 7: 1.25 x 1.32 x 2.0 mm spatial resolution over 400 x 340 x 124 mm FOV). Other acquisition parameters included; flip angle: 25°; TE/TR: 1.2ms/3.6ms; receiver bandwidth: ±83.33 kHz.

The proposed research protocol utilized a 3D radial trajectory (VIPR), with 1,000 – 1,200 projections per time frame and 36,000 – 40,000 unique projections acquired over the course of the scan. Typical image parameters for the proposed research protocol included: 1.0 x 1.0 x 1.0 mm spatial resolution over 400 x 400 x 400 mm FOV. The imaging prescription deviated from this typical protocol in two patients. (Patient 1 and Patient 2: 1.0 x 1.0 x 1.0 mm spatial resolution over 480 x 480 x 480 mm FOV). Other imaging parameters included; flip angle: 20°; TE/TR: 1.2-1.4ms/4.2-4.5ms; receiver bandwidth: ±125.0 kHz. The typical parameters corresponded to a temporal resolution of 5.2 seconds and an undersampling factor of 210 compared to a fully sampled Cartesian matrix of the same size. Table 7.2 offers a summary of the imaging parameters for the two protocols.

	TRICKS	VIPR/HYPR
Spatial Resolution	1.25 x 1.25 x 2.0 mm	1.0 x 1.0 x 1.0 mm
Update Rate	6.1 seconds	5.2 seconds
TR/TE/FA/BW	3.6ms/1.2ms/25°/±83.33 kHz	4.2-4.5ms/1.2-1.4ms/20°/±125.0 kHz

Table 7.2: Description of the imaging parameters for the TRICKS and VIPR/HYPR protocols.

The HYPR LR reconstruction method was used in this study. The general equation for a single HYPR time frame with this technique is:

Equation 7.1

$$I_H(t) = I_C \cdot I_W(t) = I_C \cdot \frac{\Phi(k_t)}{\Phi(k_t^C)}$$

where I_C is a well sampled composite image with high spatial resolution, few undersampling artifacts and low temporal resolution and $I_W(t)$ is a unique weighting image for time frame t. The function Φ() represents a reconstruction technique for the gridded k-space data for time frame t (k_t) that improves SNR and reduces undersampling artifacts compared to a corresponding undersampled, non-HYPR-processed image. In this work, SNR improvement is achieved at the cost of weighting image spatial resolution; Φ() represents a blurring function that is described in detail in Chapter 6 and Figure 6.2.

Image evaluation was performed in two rounds; TRICKS, VIPR/HYPR images were read in distinct, independent sessions by two experienced cardiovascular radiologists. For MRA evaluations, the readers were provided with three-dimensional image volumes of

multiple time phases for each imaging method. Arterial phases were chosen and read independently by each reader; a consensus method was not used. Each reader assigned grades to eleven vessel segments per leg to describe the severity of stenosis. The scale was based on the grading system of the American College of Radiology multi-institutional trial of peripheral MR angiography(74) (0 = normal/no disease, 1 = abnormal/<50% stenosis, 2 = moderate/50-74% stenosis, 3 = severe/75-99% stenosis, 4 = occluded, 9 = diagnosis not possible). Significant disease in a vessel segment was characterized by a stenosis grade of 3 or 4. For each vessel segment, readers also rated their diagnostic confidence (0 = no confidence, 1= low confidence, 2 = confident, 3 = very confident). Vessels segments were manually assigned by the individual readers as follows: (1) Popliteal artery, (2) Tibial peroneal trunk, (3) anterior tibial - proximal, (4) anterior tibial - mid, (5) anterior tibial - distal, (6) peroneal - proximal, (7) peroneal - mid, (8) peroneal - distal, (9) posterior tibial - proximal, (10) posterior tibial - mid, (11) posterior tibial - distal, see Figure 7.1.

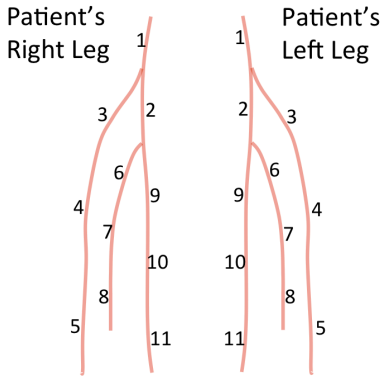

Figure 7.1: Diagram showing the vessel segments that were assigned and graded by each radiologist.

A dedicated statistician performed the statistical design and analysis for this study. Cohen's kappa (κ) was computed to assess 1) the inter-reader agreement on the presence of significant disease and stenosis grade for each method and 2) the inter-method agreement on the presence of significant disease and stenosis grade for each reader. To identify the agreement on stenosis grade, linear weights were used to calculate kappa. The magnitude of kappa was used as the basis for describing agreement as non-existent ($\kappa < 0$), slight ($0 \leq \kappa$ 0.2), fair (0.2 ≤ κ 0.4), moderate (0.4 ≤ κ 0.6), substantial (0.6 ≤ κ 0.8), and almost perfect ($\kappa \geq 0.8$), in accordance with previously published guidelines(75). Statistical computations were obtained using R 2.12.2 (76) with the irr(77), lattice(78), and plyr(79) packages.

7.3 Results and Discussion

Figures 7.2a and 7.3a show coronal maximum intensity projection (MIP) images of arterial time frames for TRICKS and VIPR/HYPR imaging series, obtained from Patient 9 and Patient 6, respectively. Figures 7.2b and 7.3b show sagitally reformatted MIP images of each patient's right leg from the TRICKS and VIPR/HYPR imaging series. The improvement in coronal plane spatial resolution – from 1.25 x 1.25 mm with TRICKS to 1.0 x 1.0 mm with VIPR/HYPR – is difficult to appreciate by visual inspection alone. However, the improvement in spatial resolution in the anterior/posterior (A/P) direction – from 2.0 mm in TRICKS to 1.0 mm in VIPR/HYPR – is easily appreciated in Figures 7.2b and 7.3b. Also, Figure 7.3b demonstrates the ringing artifact that can occur in TRICKS imaging due to the view-sharing of time-varying intravascular signal intensity(80).

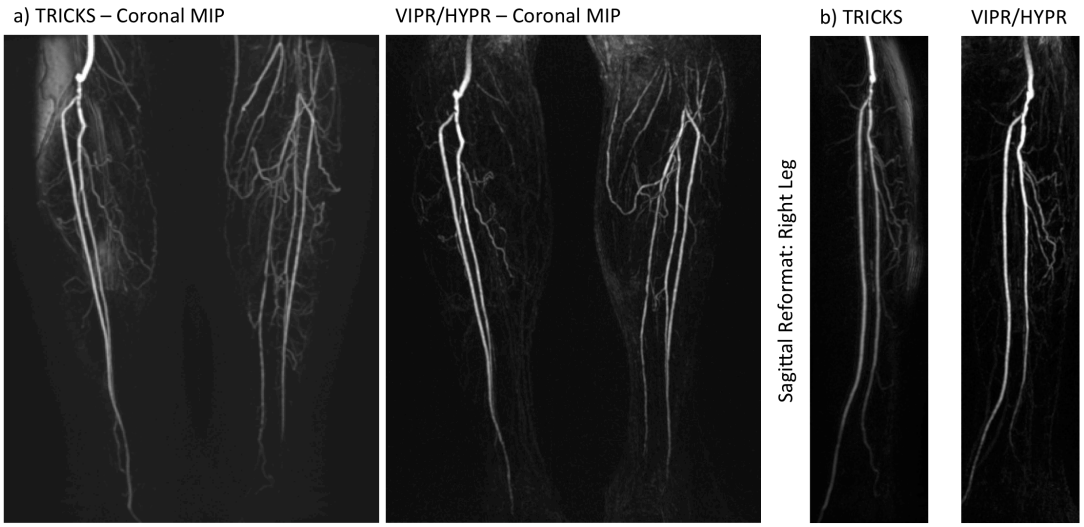

Figure 7.2: Coronal MIP images (a) and sagital reformatted MIP images (b) of arterial time frames from TRICKS and VIPR/HYPR protocols, as labeled, from Patient 9.

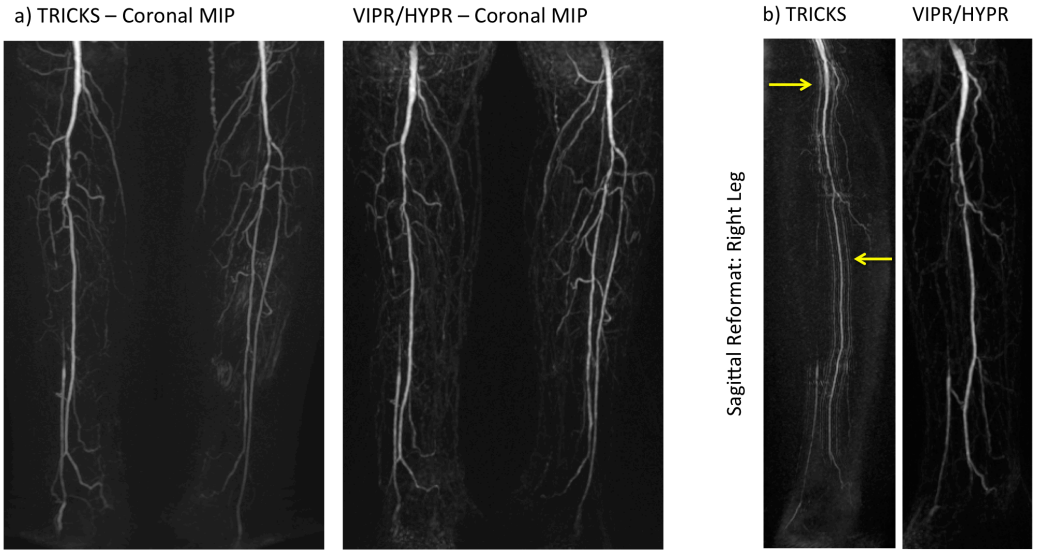

Figure 7.3: Coronal MIP images (a) and sagittal reformatted MIP images (b) of arterial time frames from TRICKS and VIPR/HYPR protocols, as labeled, from Patient 6. The yellow arrows highlight a common ringing artifact of TRICKS imaging.

Figure 7.4 demonstrates the superior temporal resolution of the VIPR/HYPR protocol. Figures 7.4a and 7.4b show four consecutive MIP images of arterial time frames from

TRICKS and VIPR/HYPR protocols, respectively. Note that not only is the frame update rate longer for the TRICKS time series (6.5 seconds versus 5.28 seconds), but the bolus edge is difficult to identify; distal arteries appear enhanced early and enhancement gradually become more intense. Figure 7.4c plots the average signal in a region of interest (ROI) placed on a distal artery in the TRICKS (dashed blue line) and VIPR/HYPR (solid red line) time series. The slope of the uptake curve is much more sharper in the VIPR/HYPR time series. This is indicative of the improved temporal resolution and temporal fidelity of the VIPR/HYPR protocol.

a) TRICKS Series

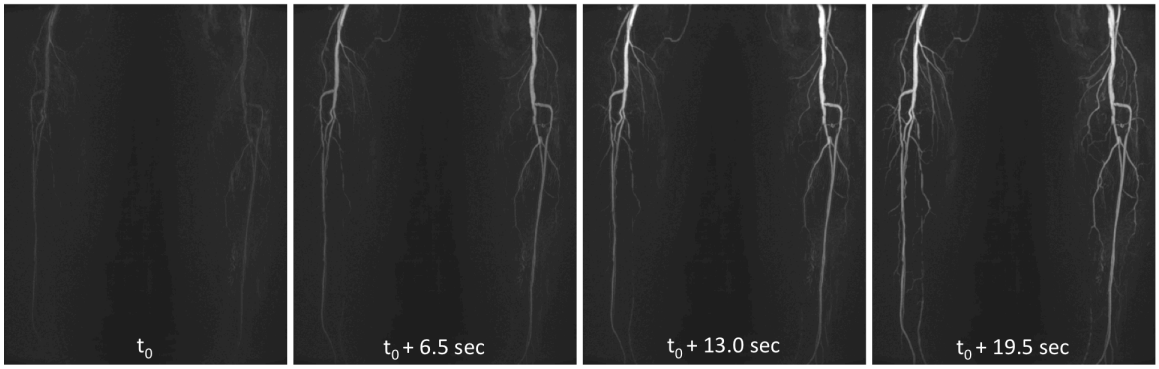

b) HYPR/VIPR Series

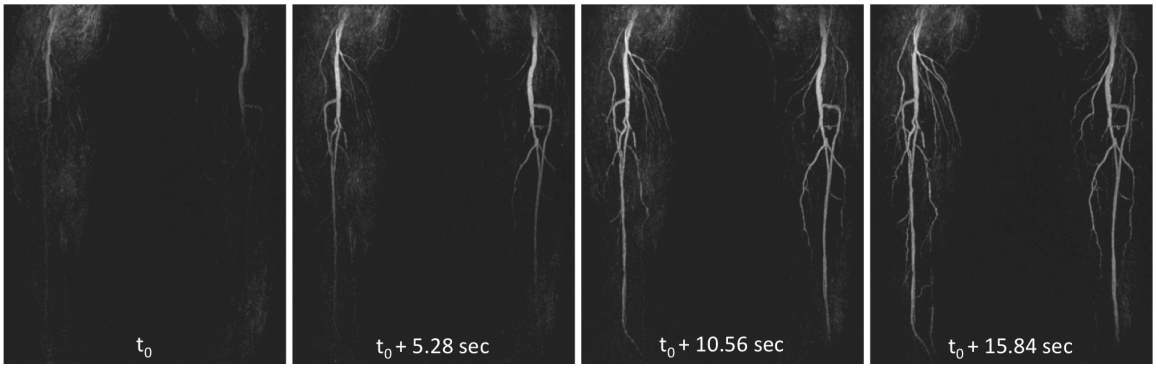

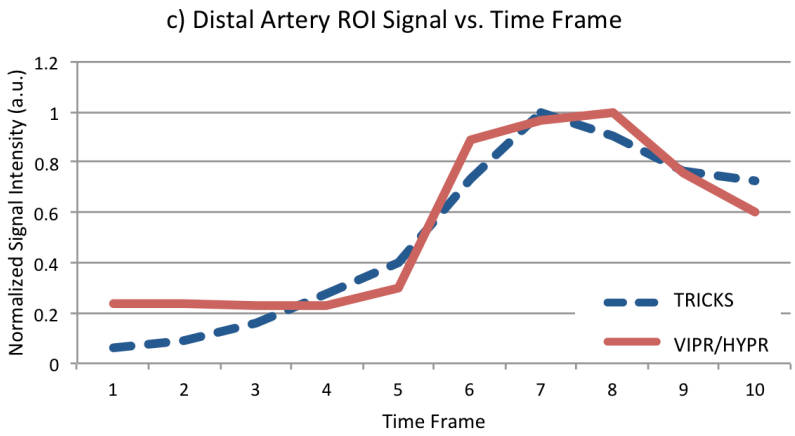

Figure 7.4: Four consecutive coronal MIP images of arterial time frames from TRICKS (a) and VIPR/HYPR (b) protocols. An ROI was placed in a distal artery and average signal in the ROI is plotted over several time frames in (c). The steep uptake curve in the VIPR/HYPR plot is indicative of superior temporal fidelity.

Table 7.3 displays the Cohen's kappa values for inter-reader and inter-method agreement on the presence of significant disease and stenosis grade. The inter-reader agreement values are similar for both methods. Both methods show substantial inter-reader agreement on the presence of significant disease. TRICKS would be categorized as having substantial agreement on the stenosis grades, while VIPR/HYPR would be categorized as having moderate agreement. The inter-method agreement within a reader on the presence of significant disease was almost perfect for Reader 1 and moderate for Reader 2. Those classifications are maintained for the level of agreement on stenosis grades.

While Cohen's kappa is meant to measure inter-reader agreement, it is only a conservative estimate for agreement between methods for a given reader; kappa is the

percent agreement penalized for chance agreement and it is not necessarily legitimate to penalize the grades of a single reader for agreeing between methods. Furthermore, though the inter-method agreement estimates may signify only moderate agreement, the current analysis does not take into account which method has the highest agreement with the true level of stenosis. An inquiry of this kind is discussed in Chapter 8.

Inter-Reader Agreement

	Significant Disease	Stenosis Grade
TRICKS	0.759 *substantial*	0.605 *substantial*
VIPR/HYPR	0.756 *substantial*	0.590 *moderate*

Inter-Method Agreement

	Significant Disease	Stenosis Grade
Reader 1	0.866 *substantial*	0.807 *substantial*
Reader 2	0.547 *moderate*	0.497 *moderate*

Table 7.3: Cohen's kappa values for inter-reader and inter-method agreement on the presence of significant disease and the stenosis grades.

7.4 Conclusion

In conclusion, a protocol based on the combination of VIPR k-space acquisition and HYPR LR image reconstruction was used to acquire time-resolved, contrast-enhanced examinations of the peripheral vessels in patients with PAD. Data were also acquired using the TRICKS method with imaging parameters that are comparable to those attained in the clinical setting. Two cardiovascular radiologists read each dataset and

eleven vessel segments in each leg were graded for the severity of stenosis. A grade of moderate stenosis or occlusion warranted the designation of significant disease. Statistical analysis was performed to calculate the inter-reader and inter-method agreement on the presence of significant disease and the stenosis grade. Both inter-method and inter-reader agreements were substantial for the presence of significant disease. Levels of agreement were not as high on the stenosis grades. However, further analysis is required to elucidate which protocol better represents the true level of stenosis.

Chapter 8: Summary and Future Work

8.1 Summary

The work presented in this dissertation is best summarized as 1) a thorough investigation of the characteristics of HYPR reconstruction, specifically with regard to magnetic resonance angiography (MRA) and 2) the development of a robust data acquisition and reconstruction strategy utilizing radial k-space sampling and HYPR reconstruction for *in vivo* MRA of the peripheral vasculature.

A numerical phantom was designed to characterize the temporal impulse response and temporal frequency response functions of the HYPR LR(46) reconstruction technique relative to two techniques commonly used for dynamic, contrast-enhanced MRA: Keyhole(47) and TRICKS(26). Since both Keyhole and TRICKS methods are based on view-sharing, the results of the numerical phantom experiment varied drastically

depending on 1) which region of k-space what was acquired during the signal impulse and 2) the frequency with which that region was updated. HYPR LR showed more consistent results in this regard. Furthermore, while the best scenarios for both Keyhole and TRICKS yielded very good temporal impulse responses, there were significant deficiencies in the spatial representation of the impulse signal in both reconstructed time series. The HYPR LR technique not only exhibited minimal temporal spreading of the impulse signal, but also superior spatial representation of the signal in the correct time frame.

A physical phantom was designed and built to further characterize the spatial and temporal fidelity of HYPR processing using real, acquired, three-dimensional data. The phantom used a computer-controlled motion stage to traverse a dilute-gadolinium filled tube through the imaging field of view in a way that mimicked a contrast bolus traveling through an artery and a nearby vein. The purpose of this work was to confirm the theoretical limits that the spatial resolution of a HYPR image is best characterized as that of the composite image, while the temporal resolution of a HYPR image is best characterized as that of the corresponding non-HYPR-processed image. Given judicious choices for the weighting image reconstruction technique, this theory was shown to be well-founded. The potential penalties and artifacts due to un-optimized reconstruction parameters were shown and discussed. The results were also reproduced in an *in vivo* model.

In later chapters, the validated reconstruction technique was used for *in vivo* imaging of both healthy volunteers and patients with peripheral artery disease (PAD). Two imaging protocols with different radial acquisition strategies were initially developed in parallel: stack-of-stars (SOS) and vastly undersampled isotropic projection reconstruction (VIPR).

To fully optimize the SOS trajectory, a data-driven parallel imaging technique was incorporated into the pulse sequence and reconstruction pipeline. This provided the ability to excite only a prescribed extent of spins in the superior/inferior direction and acquire exams with both higher temporal resolution and improved slice thickness over previously-published efforts. While the SOS + ARC technique was not pursued further in this work, it remains a tool that is widely applicable to other work at the University of Wisconsin and elsewhere.

The VIPR k-space acquisition provided more optimal characteristics and was pursued more vigorously than the SOS + ARC technique. High spatial and temporal resolutions were attainable with VIPR acquisition and HYPR LR reconstruction. Furthermore, it was shown that high quality MRA examinations of patients with PAD are feasible with the administration of fractional doses of contrast agent with the VIPR/HYPR LR imaging protocol. While further testing is necessary, this ability could prove to have significant impact in patients with mildly impaired renal function.

The VIPR/HYPR protocol was also tested for agreement with a protocol currently used in clinical practice: TRICKS. A significant improvement in both spatial and temporal

resolution was attainable using VIPR and HYPR LR. This improvement was realized while maintaining significant agreement with the TRICKS method on the presence of significant disease. Further work is needed to more completely characterize the possible benefits of the VIPR/HYPR technique.

8.2 Future Work

8.2.1 Peripheral MRA Examinations with Fractional Doses of Gadolinium-Based Contrast Agents

In Chapter 6, work was described that demonstrated the feasibility of obtaining high-quality peripheral MRA examinations with the administration of fractional doses of gadobenate dimeglumine contrast agent. In order to promote such a protocol for clinical practice, a large-scale, statistics-based study should be performed to investigate the potential effects of a low-dose exam on diagnostic ability and confidence.

Imaging series obtained after the administration of various doses of contrast agent would be graded by two radiologists for the stenosis severity and diagnostic confidence in each of 11 vessels segments per leg. The grading scale would be similar to that described in Chapter 7. Additionally, each image series would be graded for relative SNR and image quality. Cohen's kappa would be calculated for the level of agreement between stenosis grades that originate from full and low dose imaging series.

Such a study would require a large number of subjects with peripheral arterial disease to account for confounding factors such as amount of contrast agent on-board and the amount of time the subject has been at rest in the scanner prior to the administration of a given dose. Since rest pain is a typical symptom of PAD, subjects will be more likely to move during later scans. Subject motion can lead to errors in mask subtraction and poor image quality. This is further complicated by the relatively long exam time required to perform three imaging series with at least 15 minutes between each injection. If three distinct contrast agent doses were administered to each subject, the acquisition of an adequate number of subjects using each of the six possible permutations of dose order would be necessary.

8.2.2 Comparison of Image Quality and Diagnostic Accuracy of VIPR/HYPR and TRICKS for Peripheral MRA Using X-ray DSA as the Reference Standard

One criterion for patient recruitment into the study described in Chapter 7 was a scheduled appointment for a procedure that involved x-ray digital subtraction angiography (DSA) of a lower extremity. For each patient, after the research MRA examination, x-ray DSA exams were performed on a Phillips INTEGRIS V system by experienced vascular surgeons using the typical clinical protocol. Note that while MRA images were collected bi-laterally, DSA images of only a single leg were obtained.

Since both the temporal and spatial resolutions of x-ray DSA are substantially superior to any method currently available for MRA (see Figure 8.1), x-ray DSA images would be assumed to represent the true level of disease and stenosis severity in each vessel

segment. There are a few limitations of this assumption. For example, x-ray DSA provides only two-dimensional information and adjustments to the image analysis may be necessary if this limitation significantly affects or skews the outcome of the study.

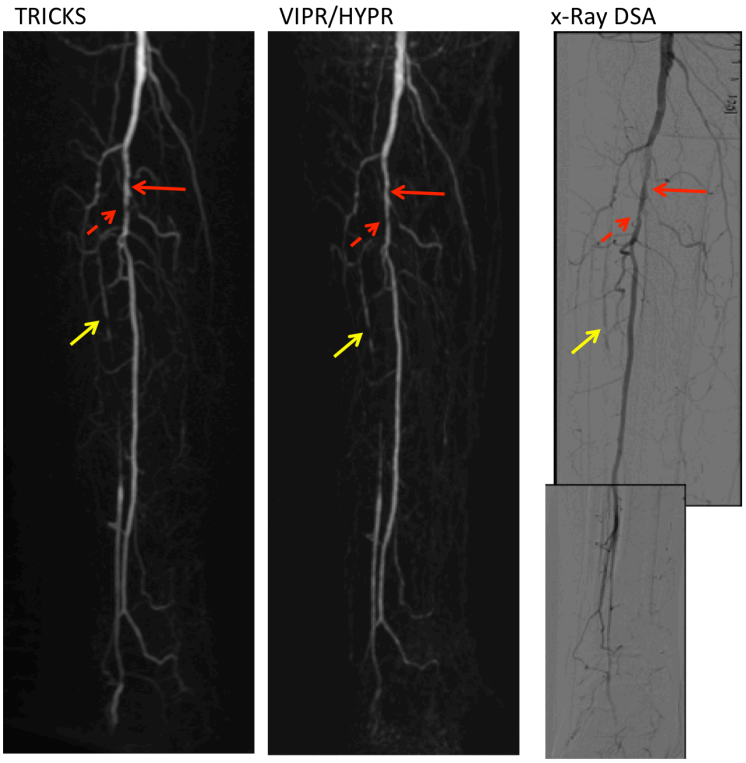

Figure 8.1: Coronal MIP TRICKS and VIPR/HYPR images cropped to show a single leg that corresponds to the x-ray DSA image shown on the right.

While, as described in Chapter 7, vessel segments in MRA images were graded for stenosis severity and confidence in diagnosis, x-ray DSA images would be read for stenosis severity only by two experienced cardiovascular radiologists. Confidence measurements would not be taken. Cohen's kappa coefficients and/or percent agreement values would be calculated for each MRA method with respect to the x-ray DSA stenosis grades.

The study described in Chapter 7 characterizes the level of agreement between stenosis severity grades based on VIPR/HYPR and TRICKS datasets. When disagreement does exist, there is currently no method to discern which imaging protocol best represents the true level of disease. By taking advantage of the x-ray DSA images available for these patients, and assuming that these images represent the truth, this future work will better characterize any improvement in diagnostic accuracy attainable with the VIPR/HYPR imaging protocol.

Bibliography

1. Marso SP, Hiatt WR. Peripheral arterial disease in patients with diabetes. Journal of the American College of Cardiology 2006;47(5):921-929.
2. Allison MA, Ho E, Denenberg JO, Langer RD, Newman AB, Fabsitz RR, Criqui MH. Ethnic-specific prevalence of peripheral arterial disease in the United States. American journal of preventive medicine 2007;32(4):328-333.
3. Hirsch AT, Hartman L, Town RJ, Virnig BA. National health care costs of peripheral arterial disease in the Medicare population. Vasc Med 2008;13(3):209-215.
4. Faxon DP, Creager MA, Smith SC, Jr., Pasternak RC, Olin JW, Bettmann MA, Criqui MH, Milani RV, Loscalzo J, Kaufman JA, Jones DW, Pearce WH. Atherosclerotic Vascular Disease Conference: Executive summary: Atherosclerotic Vascular Disease Conference proceeding for healthcare professionals from a special writing group of the American Heart Association. Circulation 2004;109(21):2595-2604.
5. Gornik HL, Beckman JA. Cardiology patient page. Peripheral arterial disease. Circulation 2005;111(13):e169-172.
6. Ouriel K. Peripheral arterial disease. Lancet 2001;358(9289):1257-1264.
7. Mohler ER, 3rd, Treat-Jacobson D, Reilly MP, Cunningham KE, Miani M, Criqui MH, Hiatt WR, Hirsch AT. Utility and barriers to performance of the ankle-brachial index in primary care practice. Vasc Med 2004;9(4):253-260.
8. Gardner AW, Montgomery PS. Comparison of three blood pressure methods used for determining ankle/brachial index in patients with intermittent claudication. Angiology 1998;49(9):723-728.
9. Resnick HE, Lindsay RS, McDermott MM, Devereux RB, Jones KL, Fabsitz RR, Howard BV. Relationship of high and low ankle brachial index to all-cause and cardiovascular disease mortality: the Strong Heart Study. Circulation 2004;109(6):733-739.
10. Oser RF, Picus D, Hicks ME, Darcy MD, Hovsepian DM. Accuracy of DSA in the evaluation of patency of infrapopliteal vessels. Journal of vascular and interventional radiology : JVIR 1995;6(4):589-594.
11. Kock MC, Adriaensen ME, Pattynama PM, van Sambeek MR, van Urk H, Stijnen T, Hunink MG. DSA versus multi-detector row CT angiography in peripheral arterial disease: randomized controlled trial. Radiology 2005;237(2):727-737.
12. Ofer A, Nitecki SS, Linn S, Epelman M, Fischer D, Karram T, Litmanovich D, Schwartz H, Hoffman A, Engel A. Multidetector CT angiography of peripheral vascular disease: a prospective comparison with intraarterial digital subtraction angiography. AJR American journal of roentgenology 2003;180(3):719-724.
13. Ota H, Takase K, Igarashi K, Chiba Y, Haga K, Saito H, Takahashi S. MDCT compared with digital subtraction angiography for assessment of lower extremity arterial occlusive disease: importance of reviewing cross-sectional images. AJR American journal of roentgenology 2004;182(1):201-209.
14. Portugaller HR, Schoellnast H, Hausegger KA, Tiesenhausen K, Amann W, Berghold A. Multislice spiral CT angiography in peripheral arterial occlusive disease: a valuable tool in detecting significant arterial lumen narrowing? European radiology 2004;14(9):1681-1687.
15. Prince MR, Zhang H, Morris M, MacGregor JL, Grossman ME, Silberzweig J, DeLapaz RL, Lee HJ, Magro CM, Valeri AM. Incidence of nephrogenic systemic fibrosis at two large medical centers. Radiology 2008;248(3):807-816.

16. Jalandhara N, Arora R, Batuman V. Nephrogenic systemic fibrosis and gadolinium-containing radiological contrast agents: an update. Clinical pharmacology and therapeutics 2011;89(6):920-923.
17. Haemel AK, Sadowski EA, Shafer MM, Djamali A. Update on nephrogenic systemic fibrosis: are we making progress? International journal of dermatology 2011;50(6):659-666.
18. Elmholdt TR, Pedersen M, Jorgensen B, Sondergaard K, Jensen JD, Ramsing M, Olesen AB. Nephrogenic systemic fibrosis is found only among gadolinium-exposed patients with renal insufficiency: a case-control study from Denmark. The British journal of dermatology 2011;165(4):828-836.
19. Hoch JR, Kennell TW, Hollister MS, Sproat IA, Swan JS, Acher CW, Burks J, Heisey DM. Comparison of treatment plans for lower extremity arterial occlusive disease made with electrocardiography-triggered two-dimensional time-of-flight magnetic resonance angiography and digital subtraction angiography. American journal of surgery 1999;178(2):166-172.
20. Miyazaki M, Takai H, Sugiura S, Wada H, Kuwahara R, Urata J. Peripheral MR angiography: separation of arteries from veins with flow-spoiled gradient pulses in electrocardiography-triggered three-dimensional half-Fourier fast spin-echo imaging. Radiology 2003;227(3):890-896.
21. Fan Z, Sheehan J, Bi X, Liu X, Carr J, Li D. 3D noncontrast MR angiography of the distal lower extremities using flow-sensitive dephasing (FSD)-prepared balanced SSFP. Magn Reson Med 2009;62(6):1523-1532.
22. Edelman RR, Sheehan JJ, Dunkle E, Schindler N, Carr J, Koktzoglou I. Quiescent-interval single-shot unenhanced magnetic resonance angiography of peripheral vascular disease: Technical considerations and clinical feasibility. Magn Reson Med 2010;63(4):951-958.
23. Hodnett PA, Koktzoglou I, Davarpanah AH, Scanlon TG, Collins JD, Sheehan JJ, Dunkle EE, Gupta N, Carr JC, Edelman RR. Evaluation of peripheral arterial disease with nonenhanced quiescent-interval single-shot MR angiography. Radiology 2011;260(1):282-293.
24. Nakamura K, Miyazaki M, Kuroki K, Yamamoto A, Hiramine A, Admiraal-Behloul F. Noncontrast-enhanced peripheral MRA: technical optimization of flow-spoiled fresh blood imaging for screening peripheral arterial diseases. Magn Reson Med 2011;65(2):595-602.
25. Sheehan JJ, Fan Z, Davarpanah AH, Hodnett PA, Varga J, Carr JC, Li D. Nonenhanced MR angiography of the hand with flow-sensitive dephasing-prepared balanced SSFP sequence: initial experience with systemic sclerosis. Radiology 2011;259(1):248-256.
26. Korosec FR, Frayne R, Grist TM, Mistretta CA. Time-resolved contrast-enhanced 3D MR angiography. Magn Reson Med 1996;36(3):345-351.
27. Willinek WA, Hadizadeh DR, von Falkenhausen M, Urbach H, Hoogeveen R, Schild HH, Gieseke J. 4D time-resolved MR angiography with keyhole (4D-TRAK): more than 60 times accelerated MRA using a combination of CENTRA, keyhole, and SENSE at 3.0T. J Magn Reson Imaging 2008;27(6):1455-1460.
28. Kinner S, Quick HH, Maderwald S, Hunold P, Barkhausen J, Vogt FM. Triple-TWIST MRA: high spatial and temporal resolution MR angiography of the entire peripheral vascular system using a time-resolved 4D MRA technique. European radiology 2012.
29. Haider CR, Hu HH, Campeau NG, Huston J, 3rd, Riederer SJ. 3D high temporal and spatial resolution contrast-enhanced MR angiography of the whole brain. Magn Reson Med 2008;60(3):749-760.

30. Lauterbur PC. Progress in n.m.r. zeugmatography imaging. Philosophical transactions of the Royal Society of London Series B, Biological sciences 1980;289(1037):483-487.
31. Glover GH, Pauly JM. Projection reconstruction techniques for reduction of motion effects in MRI. Magn Reson Med 1992;28(2):275-289.
32. Peters DC, Korosec FR, Grist TM, Block WF, Holden JE, Vigen KK, Mistretta CA. Undersampled projection reconstruction applied to MR angiography. Magn Reson Med 2000;43(1):91-101.
33. Peters DC, Derbyshire JA, McVeigh ER. Centering the projection reconstruction trajectory: reducing gradient delay errors. Magn Reson Med 2003;50(1):1-6.
34. Duyn JH, Yang Y, Frank JA, van der Veen JW. Simple correction method for k-space trajectory deviations in MRI. J Magn Reson 1998;132(1):150-153.
35. Beatty PJ, Nishimura DG, Pauly JM. Rapid gridding reconstruction with a minimal oversampling ratio. IEEE transactions on medical imaging 2005;24(6):799-808.
36. Schomberg H, Timmer J. The gridding method for image reconstruction by Fourier transformation. IEEE transactions on medical imaging 1995;14(3):596-607.
37. Yeh EN, Stuber M, McKenzie CA, Botnar RM, Leiner T, Ohliger MA, Grant AK, Willig-Onwuachi JD, Sodickson DK. Inherently self-calibrating non-Cartesian parallel imaging. Magn Reson Med 2005;54(1):1-8.
38. Heidemann RM, Griswold MA, Seiberlich N, Kruger G, Kannengiesser SA, Kiefer B, Wiggins G, Wald LL, Jakob PM. Direct parallel image reconstructions for spiral trajectories using GRAPPA. Magn Reson Med 2006;56(2):317-326.
39. Barger AV, Block WF, Toropov Y, Grist TM, Mistretta CA. Time-resolved contrast-enhanced imaging with isotropic resolution and broad coverage using an undersampled 3D projection trajectory. Magn Reson Med 2002;48(2):297-305.
40. Mistretta CA, Wieben O, Velikina J, Block W, Perry J, Wu Y, Johnson K, Wu Y. Highly constrained backprojection for time-resolved MRI. Magn Reson Med 2006;55(1):30-40.
41. Huang Y, Wright GA. Time-resolved MR angiography with limited projections. Magn Reson Med 2007;58(2):316-325.
42. Jeong HJ, Cashen TA, Hurley MC, Eddleman C, Getch C, Batjer HH, Carroll TJ. Radial sliding-window magnetic resonance angiography (MRA) with highly-constrained projection reconstruction (HYPR). Magn Reson Med 2009;61(5):1103-1113.
43. Wu Y, Korosec FR, Mistretta CA, Wieben O. CE-MRA of the lower extremities using HYPR stack-of-stars. J Magn Reson Imaging 2009;29(4):917-923.
44. Wang K, Busse RF, Holmes JH, Beatty PJ, Brittain JH, Francois CJ, Reeder SB, Du J, Korosec FR. Interleaved variable density sampling with a constrained parallel imaging reconstruction for dynamic contrast-enhanced MR angiography. Magnetic resonance in medicine : official journal of the Society of Magnetic Resonance in Medicine / Society of Magnetic Resonance in Medicine 2011;66(2):428-436.
45. Song HK, Dougherty L. k-space weighted image contrast (KWIC) for contrast manipulation in projection reconstruction MRI. Magn Reson Med 2000;44(6):825-832.
46. Johnson KM, Velikina J, Wu Y, Kecskemeti S, Wieben O, Mistretta CA. Improved waveform fidelity using local HYPR reconstruction (HYPR LR). Magn Reson Med 2008;59(3):456-462.
47. van Vaals JJ, Brummer ME, Dixon WT, Tuithof HH, Engels H, Nelson RC, Gerety BM, Chezmar JL, den Boer JA. "Keyhole" method for accelerating imaging of contrast agent uptake. J Magn Reson Imaging 1993;3(4):671-675.
48. Tsao J, Boesiger P, Pruessmann KP. k-t BLAST and k-t SENSE: dynamic MRI with high frame rate exploiting spatiotemporal correlations. Magn Reson Med 2003;50(5):1031-1042.

49. Lustig M, Donoho D, Pauly JM. Sparse MRI: The application of compressed sensing for rapid MR imaging. Magn Reson Med 2007;58(6):1182-1195.
50. Mostardi PM, Haider CR, Rossman PJ, Borisch EA, Riederer SJ. Controlled experimental study depicting moving objects in view-shared time-resolved 3D MRA. Magn Reson Med 2009;62(1):85-95.
51. O'Halloran RL, Wen Z, Holmes JH, Fain SB. Iterative projection reconstruction of time-resolved images using highly-constrained back-projection (HYPR). Magn Reson Med 2008;59(1):132-139.
52. Wu Y, Wieben O, Mistretta CA, Korosec FR. Evaluation of temporal and spatial characteristics of 2D HYPR processing using simulations. Magn Reson Med 2008;59(5):1090-1098.
53. Keith L, Kecskemeti S, Velikina J, Mistretta C. Simulation of relative temporal resolution of time-resolved MRA sequences. Magn Reson Med 2008;60(2):398-404.
54. Wieben O, Velikina J, Block W, Perry J, Wu Y, Johnson K, Wu Y, Korosec FR, Mistretta C. Highly Constrained Back Projection (HYPR):Theory and Potential MRI Applications. ISMRM. 2006; Seattle, Washington USA. p 688.
55. Holmes JH, O'Halloran RL, Brodsky EK, Bley TA, Francois CJ, Velikina JV, Sorkness RL, Busse WW, Fain SB. Three-dimensional imaging of ventilation dynamics in asthmatics using multiecho projection acquisition with constrained reconstruction. Magn Reson Med 2009;62(6):1543-1556.
56. Keith L, Kecsckemeti SR, Wu Y, Holmes JH, Wang K, Busse RF, Korosec F. Vastly Undersampled Isotripic Projection Reconsturction and HYPR for Time Resolved CE-MRA of the Peripheral Vessels. ISMRM. 2010; Stockholm, Sweden. p 1418.
57. Keith L, Korosec F, Mistretta C. MR Angiography Using Fractional Contrast Doses with VIPR and HYPR. ISMRM. 2011; Montreal, Canada. p 3328.
58. Keith L, Schiebler M, Francois C, Reeder S, Korosec F. Comparison of Diagnostic Quality of HYPR and TRICKS for Peripheral MRA Exams in Patients. ISMRM. 2012; Melbourne, Australia. p 3868.
59. Keith L, Francois C, Schiebler M, Reeder S, Korosec F. Time-Resolved Contrast-Enhaced Peripheral MRA in Patients with Low Contrast Doses Using VIPR-HYPR. ISMRM. 2012; Melbourne, Australia. p 4159.
60. Wu H, Block W, Samsonov A. HYPR-Constrained Compressed Sensing Reconstruction for Accelerated Time Resolved Imaging. ISMRM. 2008; Toronto, Canada. p 339.
61. Griswold M, Barkauskas K, Blaimer M, Moriguchi H, Sunshine J, Duerk J. More Optimal HYPR Reconstructione Using a Combination of HYPR and Conjugate-Gradient Minimization. Club M. 2006; Basel, Switzerland. p 29.
62. Du J, Carroll TJ, Wagner HJ, Vigen K, Fain SB, Block WF, Korosec FR, Grist TM, Mistretta CA. Time-resolved, undersampled projection reconstruction imaging for high-resolution CE-MRA of the distal runoff vessels. Magn Reson Med 2002;48(3):516-522.
63. Du J, Korosec FR, Thornton FJ, Grist TM, Mistretta CA. High-resolution multistation peripheral MR angiography using undersampled projection reconstruction imaging. Magn Reson Med 2004;52(1):204-208.
64. Du J, Thornton FJ, Fain SB, Korosec FR, Browning F, Grist TM, Mistretta CA. Artifact reduction in undersampled projection reconstruction MRI of the peripheral vessels using selective excitation. Magn Reson Med 2004;51(5):1071-1076.
65. Winkelmann S, Schaeffter T, Koehler T, Eggers H, Doessel O. An optimal radial profile order based on the Golden Ratio for time-resolved MRI. IEEE transactions on medical imaging 2007;26(1):68-76.

66. Griswold MA, Jakob PM, Heidemann RM, Nittka M, Jellus V, Wang J, Kiefer B, Haase A. Generalized autocalibrating partially parallel acquisitions (GRAPPA). Magn Reson Med 2002;47(6):1202-1210.
67. Brau AC, Beatty PJ, Skare S, Bammer R. Comparison of reconstruction accuracy and efficiency among autocalibrating data-driven parallel imaging methods. Magn Reson Med 2008;59(2):382-395.
68. Pruessmann KP, Weiger M, Scheidegger MB, Boesiger P. SENSE: sensitivity encoding for fast MRI. Magn Reson Med 1999;42(5):952-962.
69. Du J, Carroll TJ, Brodsky E, Lu A, Grist TM, Mistretta CA, Block WF. Contrast-enhanced peripheral magnetic resonance angiography using time-resolved vastly undersampled isotropic projection reconstruction. J Magn Reson Imaging 2004;20(5):894-900.
70. Mistretta CA. Undersampled radial MR acquisition and highly constrained back projection (HYPR) reconstruction: potential medical imaging applications in the post-Nyquist era. J Magn Reson Imaging 2009;29(3):501-516.
71. Velikina JV, Johnson KM, Wu Y, Samsonov AA, Turski P, Mistretta CA. PC HYPR flow: a technique for rapid imaging of contrast dynamics. J Magn Reson Imaging 2010;31(2):447-456.
72. Wu Y, Johnson K, Kecskemeti SR, Wang K, Wieben O, Aagaard-Kienitz BL, Rowley H, Korosec FR, Mistretta C, Turski P. Time resolved contrast enhanced intracranial MRA using a single dose delivered as sequential injections and highly constrained projection reconstruction (HYPR CE). Magn Reson Med 2011;65(4):956-963.
73. Pruessmann KP, Weiger M, Scheidegger MB, Boesiger P. SENSE: sensitivity encoding for fast MRI. Magn Reson Med 1999;42(5):952-962.
74. Baum RA, Rutter CM, Sunshine JH, Blebea JS, Blebea J, Carpenter JP, Dickey KW, Quinn SF, Gomes AS, Grist TM, et al. Multicenter trial to evaluate vascular magnetic resonance angiography of the lower extremity. American College of Radiology Rapid Technology Assessment Group. JAMA : the journal of the American Medical Association 1995;274(11):875-880.
75. Landis JR, Koch GG. The measurement of observer agreement for categorical data. Biometrics 1977;33(1):159-174.
76. Team RDC. R: A language and environment for statistical computing. Vienna, Austria: R Foundation for Statistical Computing; 2009.
77. Gamer M, Lemon J, Fellows I, P S. irr: Various Coefficients of Interrater Reliability and Agreement. R Package Version: 0.83; 2010.
78. Sarkar, Deepayan. Lattice: Multivariate Data Visualization with R. New York: Springer; 2008.
79. Wickham, Hadley. The Split-Apply-Combine Strategy for Data Analysis. Journal of Statistical Software 2011;40(1):1-29.
80. Maki JH, Prince MR, Londy FJ, Chenevert TL. The effects of time varying intravascular signal intensity and k-space acquisition order on three-dimensional MR angiography image quality. J Magn Reson Imaging 1996;6(4):642-651.